DESIGN AND EVALUATION OF SLOT MULTIPLE ELEMENT ANTENNAS

by

Jane Xing Yun
M. Sc., University of Calgary, 2004
B. Eng., Beijing University of Aeronautics and Astronautics, 1997

THESIS SUBMITTED IN PARTIAL FULFILLMENT OF
THE REQUIREMENTS FOR THE DEGREE OF

DOCTOR OF PHILOSOPHY

In the
School of Engineering Science
Faculty of Applied Sciences

SIMON FRASER UNIVERSITY

Summer 2011

APPROVAL

Name: **Jane Xing Yun**

Degree: **Doctor of Philosophy**

Title of Thesis: **Design and Evaluation of Slot Multiple Element Antennas**

Examining Committee: _____

Chair: **Dr. James K. Cavers, P. Eng**
Professor Emeritus, School of Engineering Science

_____

Dr. Rodney G. Vaughan
Senior Supervisor
Professor, School of Engineering Science

_____

Dr. Shawn Stapleton, P. Eng
Supervisor
Professor, School of Engineering Science

_____

Dr. Behrouz Pourseyed, P. Eng
Supervisor
Director, RF Engineering
Sierra Wireless, Inc.

_____

Mr. James P. Warden
Supervisor
Director, Advanced Antenna and Electromagnetic Research
Research in Motion Limited

_____

Dr. Sami Muhaidat
Internal Examiner
Associate Professor, School of Engineering Science

_____

Dr. Michael A. Jensen
External Examiner
Professor and Department Chair, Department of Electrical and Computer Engineering, Brigham Young University

Date Defended/Approved: _____ June 2, 2011

Partial Copyright Licence

ABSTRACT

MIMO uses multiple element antennas (MEAs) at the transmitter and receiver to exploit spatial channels for improving communications performance such as spectral efficiency and outage. The performance returns for MIMO become significant when the number of antennas at each end of the link becomes large. The challenges in the realization of MIMO lie with both the extra antennas and the extra communications signal processing.

In mobile communications, a basic problem is integrating a large number of uncorrelated antenna elements within the mobile terminal. As yet, there are no standard figures of merit or measurement procedures to evaluate the performance of the MIMO antennas. Consequently, MEA designs are often developed in a rather ad hoc way, without a formal measure of how well the antenna system is performing. Parameters such as correlation, diversity gain and capacity are popularly used as metrics for MIMO antenna performance. However, the correlation describes an aspect of the statistical characteristics, the diversity gain assumes a signal combination technique, and the capacity further includes the communications performance. These terms can be attributed to MEA designs, but they do not address important design aspects of the antennas themselves. For example, the compactness and efficiency (which must include the mutual coupling losses) of MEAs for MIMO are undeveloped.

This dissertation addresses new MEA evaluation techniques and new types of antennas. New figures of merit for MIMO antennas are proposed, including MEA space efficiency. The evaluation is demonstrated using idealized antennas and slot MEA examples designed in this dissertation. The antennas use the slot elements because of their advantages over other elements types. Contributions include new design information for slot elements as well as new MEA designs using the slot elements.

DEDICATION

To my husband and family for believing in me.

ACKNOWLEDGEMENTS

My deepest gratitude goes to my supervisor Prof. Rodney G. Vaughan, who allowed me to pursue my dream of completing a PhD program under his guidance. Through all these years, he patiently supported, encouraged and helped me to develop my research skills, along with other skills. His impact on my professionalism and personality will last a lifetime.

My gratitude also goes to my supervisory committee members Prof. Shawn Stapleton from Simon Fraser University, Dr. Behrouz Pourseyed from Sierra Wireless Inc. and Mr. James P. Warden from Research In Motion Limited for their helpful advices on this dissertation from both the academia and industrial points of view. I am grateful for Prof. Sami Muhaidat's participation as the internal examiner and his suggestions from the signal processing point of view.

It is an honour for me to have one of the world's best researchers in wireless communication, Prof. Michael A. Jensen from Brigham Young University, as my external examiner. As a professor, department chair, and chief editor of the IEEE Transactions on Antenna and Propagation, also with many other obligations, his time is extremely valuable. His attendance of the defence is an honour to me. His suggestions for adding comments on approaches using microwave network theory, modes of the propagation channel, and volumetric modes of an antenna are gratefully acknowledged.

A special thank to Mr. John Demas from Nearfield System Inc. and Mr. Steve Whitmore from Simon Fraser University who looked closely at the draft version of this dissertation for English style and grammar, correcting both and offering suggestions for improvement.

I am indebted to all my colleagues in the lab who supported me with their friendship, especially when my progress seemed slow: Seyed Alireza Banani, Maryam Dehghani Estarki, Andrew Lea, Piraj Fozoonmayeh, and many others.

TABLE OF CONTENTS

LIST OF FIGURES

LIST OF TABLES

ABBREVIATIONS

a	Groundplane width
b	Groundplane length
$BW_{\text{-10dB}}$	-10dB impedance bandwidth
C	Capacity bandwidth efficiency, called “capacity” in short here
CDF	Cumulative density function
CSI	Channel state information
D	Slot depth
DG	Distributed gain
EGC	Equal Gain Combining
FBR	Front-to-back ratio
g_θ	Normalized θ–polar vector field pattern
g_ϕ	Normalized ϕ–polar vector field pattern
G	Antenna gain or gain pattern
G_{div}	Diversity gain
h	Far field pattern
H	Channel matrix
ka	Electrical radius of the MEA spherical volume
ka_e	Electrical radius per equivalent element of the MEA

ka_{chu}	Electrical radius on the Chu limit for the given Q_{rad}
L	Slot length
LTE	Long Term Evolution
L / λ	Slot electrical length
M_e	Equivalent number of idealized elements of an MEA
MEA	Multiple Element Antenna
MEG	Mean effective gain
MIMO	Multiple-Input, Multiple-Output
MSA	Minimum Scattering Antenna
MRC	Maximum Ratio Combining
n_T	Number of transmit antennas
n_R	Number of receive antennas
p_θ	θ components of the power density function of incoming wave
p_ϕ	ϕ components of the power density function of incoming wave
Q	Unloaded quality factor
Q_{rad}	Radiation quality factor
R	Resistance matrix
S	Scattering parameter matrix
SC	Selection Combining
SCM	Spatial Channel Model
S_{ii}	Reflection coefficient of the *ith* port
S_{ij}	Transmission coefficient from the *jth* port to the *i*th port

S_θ	θ– polar angular power distribution of the incoming wave
S_ϕ	ϕ–polar angular power distribution of the incoming wave
SVD	Singular value decomposition
SNR	Signal-to-noise-ratio
SwC	Switched Combining
V_e	Effective element volume
V_{MEA}	MEA spherical volume
w	Slot width
X	Reactance matrix
XPR	Cross polarization ratio
Z	Impedance matrix
$\mathbf{Z_A}$	MEA impedance matrix
$\mathbf{Z_L}$	Loading circuit impedance matrix
α	Wedge angle
ϕ	Azimuth angle
γ_c	Instantaneous *SNR* of combined received signal
γ_{ref}	Instantaneous *SNR* of received signal by reference antenna
Γ	Mean *SNR* on one branch
Γ_{ref}	Mean *SNR* on reference branch
η_{pol}	Polarization efficiency
η_{rad}	Radiation efficiency
η_{total}	Total efficiency

η_{space}	Space efficiency
$\boldsymbol{\eta}_{\mathbf{total}}$	MEA total efficiency matrix
λ	Wavelength
λ_k	Singular value of the *k*th element
$\lambda_{scale,k}$	Scaled singular value of the *k*th element
$\boldsymbol{\Lambda}$	Singular value column matrix
$\boldsymbol{\Lambda}_{\mathbf{scale}}$	Scaled singular value column matrix
θ	Zenith angle
$\boldsymbol{\rho}_{\mathbf{L}}$	Loaded circuit voltage correlation coefficient matrix
$\boldsymbol{\rho}_{\mathbf{L,H}}$	Estimated loaded circuit voltage correlation coefficient matrix with pattern approach
$\boldsymbol{\rho}_{\mathbf{L,S}}$	Estimated loaded circuit voltage correlation coefficient matrix with scattering parameter approach
$\boldsymbol{\rho}_{\mathbf{L,Z}}$	Estimated loaded circuit voltage correlation coefficient matrix with impedance approach
$\boldsymbol{\rho}_{\mathbf{O}}$	Open circuit voltage correlation coefficient matrix
$\boldsymbol{\rho}_{\mathbf{O,H}}$	Estimated open circuit voltage correlation coefficient matrix with pattern approach
$\boldsymbol{\rho}_{\mathbf{O,S}}$	Estimated open circuit voltage correlation coefficient matrix with scattering parameter approach
$\boldsymbol{\rho}_{\mathbf{O,Z}}$	Estimated open circuit voltage correlation coefficient matrix with impedance approach
$\boldsymbol{\rho}_{\mathbf{scale}}$	Scaled correlation coefficient matrix

CHAPTER 1: INTRODUCTION

Multiple element antennas (MEAs) are to improve communications performance by deploying antenna diversity and multiple-input, multiple-output (MIMO) techniques in multipath environments, or by suppressing interference through spatial filtering.

A special case of an MEA is the classical array antenna, which has identical, regularly-spaced elements, as defined in [1]. In particular, arrays are distinguished by having a scalar array factor that multiplies the element pattern in order to facilitate pattern analysis and synthesis, *cf*., [2]-[4], often for directional pattern related applications.

MEAs are more general than arrays. An MEA can comprise identical or different types of the elements, e.g., [5], so the classical array factor may not be applicable. The MEA elements can be irregularly spaced and differently orientated to minimize mutual coupling for maximizing diversity performance, while also seeking a minimal size. In most cases, the elements need to be arranged to suit the shape and volume requirements of the platform. The differences between arrays and MEAs are discussed in Appendix A in more detail.

MEAs are required for MIMO systems, so the MEA communications performances are of the primary interest, as introduced below.

1.1 MEAs for MIMO and diversity systems

MIMO technology is drawing tremendous attention as a powerful solution for increasing data throughput and for improving reception reliability in wireless communications, without additional transmit power and bandwidth. MIMO uses MEAs at both the transmitter and receiver to exploit spatial channels for increasing data rates. Data are transmitted over each antenna element, and the transmit power is divided among the transmit channels, either evenly or weighted, based on the knowledge of the channels. The data throughput of a MIMO system increases with the number of antennas, as shown below.

The *capacity bandwidth efficiency* (called *capacity* for simplicity in this dissertation), C, denotes the MIMO channel capacity over the utilized bandwidth. The capacity of parallel channels was treated by Gallagher in the 1960s and is now in current information theory texts, e.g., [6]. The capacity limit for MIMO channels is given by the sum of the Shannon capacities of the water-filled eigen-channels. A pragmatic approach is to divide the transmit power equally between the transmit antennas, and this provides a capacity close to the Shannon limit. However, compared to an optimized transmission, such as eigen-MIMO, it is likely to cause more interference in a multi-user system which is sharing spectrum. For random channels, there is a simple formula for this “equal transmit power” capacity [7][8]. For a system with n_T transmit and n_R receive antennas, C is

$$C = \log_2 \det\ [I + \frac{SNR}{n_T} HH^{\mathrm{H}}] \qquad \text{(bit/s/Hz)} \qquad (1\text{-}1)$$

where I is the $n_R \times n_R$ identity matrix, H is a $n_R \times n_T$ channel matrix, the operation $()^{\mathrm{H}}$ is the Hermitian conjugate transpose, and SNR is the average signal-to-noise-ratio at the output of each receiving antenna element, or strictly speaking after the low noise amplifier where the receiving SNR is established. In Eq. (1-1), SNR is assumed to be the same for each receiving element.

For an $N \times N$ system, when the channels are uncorrelated Eq. (1-1) simplifies, as developed by Winters as early as in 1987 [7], but more famously presented in [8]

$$C = N \log_2(1 + \frac{SNR}{N}) \qquad \text{(bit/s/Hz)} \qquad (1\text{-}2)$$

When N is large (say $N>10$), the capacity is increased essentially linearly with the number of antennas for a given SNR. Therefore, large N systems are more of interest for achieving a much higher capacity than a Single-Input, Single-Output (SISO) system can provide. In other words, large-N, uncorrelated MEAs are needed at both the transmitter and the receiver for high capacity performance.

MEAs can also achieve more reliable reception in a multipath environment through antenna diversity [9]-[11]. Antenna diversity uses multiple antennas to transmit and/or receive the same signal. The transmitted copies of the signal experience different propagation paths, and may arrive at the receivers at different times. The received copies of the signal are then selected or combined

so that deep fades can be avoided and the signal can be recovered at times when it is not possible using single antennas. Popular diversity schemes (*cf*. [9][10][12]) include Maximum Ratio Combining (MRC), Equal Gain Combining (EGC), Selection Combining (SC), Switched Combining (SwC), Optimum Combining (OC), etc.

To achieve higher reception reliability and significantly increased data throughput, large-*N*, uncorrelated MEAs are of interest for MIMO systems. However, this imposes a grand challenge to MIMO implementation, especially in small mobile terminals due to the difficulty in integrating a large number of antenna elements in small devices, which have sufficiently low correlation for diversity action.

In the context of modal theory, a larger volume for an antenna will support more spherical radiating modes [13][14]. Similarly, a multipath propagation environment can be couched as supporting multiple modes [15][16]. By adding extra antenna elements to the MEA, the volume of the MEA is increasing and the aperture of the antenna is increasing, helping to support higher numbers of radiation modes and linking to propagation channel modes. Modes are not otherwise discussed in this dissertation.

1.2 Current state of MIMO implementation in industry

Owing to its potential for improving spectral efficiency and reception reliability, MIMO technology is being deployed in current wireless communication systems. The recent 3GPP Long Term Evolution (LTE) [17] has set high data

throughput performance requirements, such as a downlink peak data rate of at least 100Mbps and an uplink rate of at least 50Mbps. Furthermore, the LTE Advanced, submitted for 4G systems in the fall of 2009 and expected to be finalized in 2011, has set the peak data rate up to 1Gbps for low mobility cases and 100Mbps for high mobility cases. To attain the high data rate requirements, MIMO combining with other techniques, such as orthogonal frequency-division multiple access (OFDMA) MIMO, is required in the LTE standards [18].

However, LTE requires only a small number of antennas on small handheld devices (also called UE – user equipment in mobile communication industry). For example, 3GPP LTE requires only 2 receive and 1 transmit antennas on an UE, and LTE Advanced requires maximum 4 × 4 MIMO. This modest dimension is due to the complexity and difficulties of MIMO implementation in small devices.

1.3 Difficulties in MIMO implementation

Currently MIMO implementation is facing several problems, including the following: 1) for techniques that use channel state information (CSI), there is much channel usage required which bites into the capacity; 2) integrating a number of antenna elements in the limited size of mobile devices; and 3) lack of figures of merit and standard measurement procedures to evaluate the performance of MIMO antennas.

In the first problem, CSI provides the complex gain of the channel. Complete MIMO channel CSI is required for eigen-MIMO [12][19], so as to

achieve the maximum data throughput. However, in the real world, full CSI is never known perfectly *a priori*. It needs to be estimated at the receiver based on pilot symbols sent from the transmitter and fed back to the transmitter. For this reason, bandwidth is necessarily used for obtaining CSI (there are no blind channel sounding systems available yet). In a fast fading environment, the channel condition varies rapidly, so CSI needs to be updated quickly as well. For a high order MIMO system in a high mobility environment, the CSI acquisition can dominate the bandwidth consumption, and the point of deploying this type of MIMO becomes lost. Eigen-MIMO is not suitable for fast-fading (relative to the symbol rate) channels. In the last decade, there have been many papers addressing MIMO CSI acquisition, and the solutions generally fall into two categories: blind and non-blind estimation, e.g., [20]-[26].

The second problem is currently the major difficulty in implementing MIMO communication systems. Since an MEA must contain a number of antenna elements, it may be bulky. The physical sizes of MEAs are probably less of a problem for base stations, which normally have the flexibility for expanded volume to accommodate more complex antenna configurations. But handheld devices have very limited space for antennas and also are subject to losses incurred by the presence of the user.

Furthermore, the antenna elements tend to become correlated when implemented in a small volume. When the MEA elements are correlated on either side of the communication link, the MIMO capacity is reduced. Low correlation and compactness are conflicting requirements.

A lack of standards for evaluation and measurement procedures is the third problem. In the current state, MEA design for MIMO is still mainly based on the knowledge of single element antennas and conventional antenna arrays. Terms and definitions for single element antennas and antenna arrays are well understood [1], and measurement procedures are provided in [27]. MEAs are of course more complicated than single elements, and no standard is defined by IEEE or elsewhere for their evaluation. In practice, current MEA designs are often developed in a rather *ad hoc* way, without a formal measure of how well the antennas are performing (e.g., how compact an MEA is, and what is the MEA efficiency in terms of power lost through mutual coupling). A few other terms, such as correlation, diversity gain [12] and capacity, are popularly used as the metrics of MIMO antenna performance. However, these terms describe the statistical characteristics of the signals as well as the communication performance of the systems. These terms can be attributed to the given MEAs, but they do not address important design aspects of the antennas themselves.

1.4 Focus of the dissertation

The first problem addressed above is a signal processing research problem, and it is not the focus of this dissertation. The last two problems are antenna design and evaluation issues, and they are the focus here.

This dissertation has two themes: 1) MEA elements and structures for compact large-*N* MIMO antenna designs; 2) MIMO antenna evaluation. The first theme is finding different antennas which are feasible as MIMO antenna elements and have an advantage over currently designs such as dipoles and

patches. The elements must have an effective geometrical configuration which allows them to be used for compact MEAs while retaining their performance. The slot antenna is the solution explored in this dissertation. It is also of interest to find suitable geometrical arrangements, other than linear or planar ones, for compact and large-*N* MEAs. The second theme involves the investigation of MIMO antenna evaluation metrics, especially on the efficiency and compactness of MEAs. New figures of merit are proposed for MIMO antenna evaluation.

1.5 Organization of the dissertation

The rest of the dissertation comprises three main parts, as follows.

1) The first part comprises Chapter 2, which provides comprehensive and detailed reviews on the state of the art in MIMO antenna design and evaluation. As the preferred MEA element in this dissertation, the slot antenna and its literature are also reviewed.

2) The second part is in Chapters 3 and 4. New MEA evaluation techniques are presented. Chapter 3 discusses MEA efficiency and its impact on diversity gain and capacity, while Chapter 4 introduces a new figure of merit - an MEA space efficiency to evaluate the compactness of MEAs

3) The third part is in Chapters 5 to 7, covering slot-based MEA designs and evaluations. Chapter 5 focuses on a stand-alone slot antenna in a small groundplane. Its performance as a candidate element for a MIMO antenna is studied. The impact of the rectangular slot shape and the groundplane details on the antenna performance is investigated with parametric study. Chapters 6 and 7

give two examples of large-*N* MEAs utilizing slot elements. With the MEA evaluation metrics provided in Chapters 3 and 4, the two proposed large-*N* MEAs are evaluated and their performances are discussed.

The dissertation is summarized in Chapter 8. The appendices address: the difference between MEAs and conventional array antennas; future directions for slot MEA design and applications; and a list of publications that have stemmed from the research for this dissertation.

CHAPTER 2: LITERATURE REVIEW

In the last decade, research on MIMO antenna designs is attracting massive attention despite the difficulty of MIMO implementation. This chapter starts with the review of MIMO antenna designs and it also identifies some interesting topics on MEA antenna design that are treated in this dissertation.

In the second part of this chapter, currently available MIMO antenna evaluation techniques in the literature are outlined. The commonly used parameters to measure MEA performance are summarized to prepare for the discussion on new figures of merit for MEA evaluation in the following two chapters. This does not extend to over-the-air (OTA) testing procedures currently evolving within the industry.

In the last part of this chapter, the slot antenna is reviewed. The slot is not as widely understood, or used, as other types of elements, such as the dipole or patch. Inspired by its benefits, for example, being low profile on a metal surface and inherently compatible with the shapes of many types of terminals, the slot is adopted as the element for MEAs in this dissertation. The review of the stand-alone slot antenna paves the way for its applications in the last three chapters.

2.1 Review on MIMO antenna design in literature

Current MIMO antenna design research focuses on antenna element design, geometric arrangement of the elements for compact antenna size, and techniques to reduce mutual coupling. The goal is to obtain de-correlated signals from different antenna elements with high distributed gains for maximizing *SNR*s.

The basic antenna element types (i.e. dipole, loop, slot and patch) have been exploited in designs reported in the literature. Dipoles (or their monopole counterparts) – both wire and printed, and the patch, have been the most popular elements owing to their simplicity of manufacture and because their performance characteristics are well documented. Odd shapes of elements have also appeared, which are mainly to get multiple frequency bands matched. Often, in compact mobile terminals, the compact “antenna” is really acting as an impedance match to the electrically larger chassis (typically a conducting plate) of the device, i.e. the chassis is a critical part of the radiating structure. There are numerous papers on various MEA designs with dipoles and patches, for example, [28]-[39]. On the contrary, loops and slots are seldom used in MIMO antenna design. Relatively few papers are available here, such as [40]-[42] for the loop and [43]-[46] for the slot.

MIMO antenna design research has been focusing on the techniques to reduce antenna size and fit multiple antennas into a space-limited device. Recently, the mm-wave Industrial, Scientific and Medical (ISM) bands (e.g., 24, 60, and >100 GHz) is drawing increasing attention to MIMO research because of

the small physical sizes of the antennas. The drawbacks of these antennas, including low efficiency are being addressed by current research.

The concept of “multi-feed diversity antennas” is also drawing attention. Here, one antenna structure has multiple feeds at different locations. The feeds excite orthogonal modes, and in turn, their patterns are orthogonal. Pattern diversity is achieved with a single antenna structure. This technique was discussed in [47], and the concept has also been developed for handsets, for example, [48].

The goal of MIMO is to increase link quality, for example to increase the capacity, reliability, etc. In MIMO, antenna diversity can be implemented at the receiver or the transmitter, or both. Diversity patterns are derived by exploiting: spacing the antenna elements apart (spatial diversity); orthogonal polarizations (polarization diversity); patterns with different directional coverage (angle diversity). Using any of these, or a combination of them can be referred to as pattern diversity. Examples of spatial diversity include [28][29][31][32][46], polarization diversity, [5][41], and for angle diversity, [5][41][43][44][47][49].

Another approach to the problem of reducing correlation is by directly considering the radiating structure rather than the resulting embedded element patterns, and the concept of “feed point isolation” is presented in, for example, [31]. It is typically realized by disconnecting or extending the path of electric current flow between the feeds of each two MEA elements. For example, for an MEA with its elements sharing a groundplane, inserting slots between the feeds in the groundplane will extend the currents paths, and thereby reduce the coupling.

Yet another approach to reducing correlation is by “post signal processing”, which refers to combining correlated received signals to produce a smaller number of branches that have lower correlations. An example of such an orthogonalization is [50].

The current state of MIMO antenna research is summarized as follows.

1) The majority of the published MIMO antenna designs have narrow bandwidth, mostly below 10% for the -10dB fractional impedance bandwidth. However, since wide bandwidth provides higher capacity, antennas with wider bandwidth are of increasing interest for the future wireless communication systems such as MIMO-OFDM. It is noted here that the capacity efficiency (in bits per sec per Hertz) is increased by having more antennas, and the extra bandwidth increases capacity, but not capacity efficiency. The significance of MIMO is in its narrowband performance.

2) The number of antenna elements is mostly below 4 in published antenna designs. Antennas with more elements (such as greater than 8) are rarely found in the literature. This is again due to the difficulty in arranging a large number of elements in a limited size without losing much of the performance. Also, the current standards for communications (such as the IEEE 802 series) do not yet discuss more than 4 antenna systems.

3) The majority of presented MEAs are for handheld devices. Designs for base stations, access points, repeaters, notebooks, tags, USB keys, etc., are not as well covered in the literature as for handheld terminals.

4) Linear and planar geometric arrangements are popularly exploited because most of the described MIMO antennas are on circuit boards within handheld devices. Antenna elements have to be spread out for low mutual coupling, or additional isolation techniques have to be applied to closely spaced elements for compact MIMO antennas.

5) Dipole and patch elements are popularly applied in the literature and in practice. The benefit of slot antennas is having a low profile and being able to conform to (conducting) surfaces of terminals. These have not yet been widely applied in MIMO antenna design.

In this thesis, the slot antenna is investigated for large-*N* MEAs with wider bandwidth than for just narrow band operation. To achieve compact slot MEAs, a three-dimensional geometric arrangement (i.e., other than linear or planar arrangements) suitable for slot MEAs is proposed. Applications of interest include handheld devices, access points, base stations, laptops, tablets, USB dongles, etc.

2.2 Review on MIMO antenna evaluation techniques

In the presence of mutual coupling, the impedance and radiation behaviour at each element of an MEA will be impacted by the other elements and their terminations. The performance of each MEA element can still be described with the parameters defined for single element antennas and arrays in [1], including input impedance, polarization, radiation pattern, etc. However, the element must be considered with the presence of other elements, i.e., we must

consider the *embedded element*. The parameters for single port antennas are in, for example, [1][4][51][52], and their extensions to MEAs are reviewed below. MEA parameters such as the correlation matrix and diversity gain are now used to measure the performance of MIMO antennas in multipath scenarios [12], and are also reviewed below.

2.2.1 Scattering parameter matrix and impedance matrix

Mutual coupling is the interaction between two antennas [53]. The amount of coupled energy depends on the physical proximity and polarization of the antennas. The coupling can be viewed as a current flowing on one element which is induced by the fields from the excitation of another element. If observed from the antenna port, this extra current causes impedance alternation, viz., the mutual impedance combined with the self impedance defines the input impedance. Therefore, mutual coupling relates to the antenna compactness and affects the communications performance, e.g., [54]-[57]. It is important in MIMO design to have a good understanding of mutual coupling and its effects.

The **scattering parameter matrix (S)** contains reflection coefficients (S_{ii}) and transmission coefficients (S_{ij}) measured at the ports of an MEA [58]. S_{ii} is the ratio of reflected voltage to incident voltage at the port of the ith element when all the other ports are terminated and matched so there are no reflections, and in this sense, it gauges how well this element is matched to its port impedance. S_{ij} is the ratio of the voltage transferred from the jth element port to the ith element port to the incident voltage at the jth element port. S_{ij} is a measure of mutual

coupling between the antenna elements. Using a Vector Network Analyzer (VNA) is the most convenient method to measure scattering parameters.

The **impedance matrix (Z)** includes the self and mutual impedances of an MEA. Their definitions and measurements can be found in, for example, [12]. However, we do not need to measure these impedances directly from their definition. Instead, **Z** of an MEA can be calculated from its scattering parameter matrix **S** and the port reference impedance Z_o (normally 50Ω) using network theory [58] as

$$\mathbf{Z} = \mathbf{R} + j\ \mathbf{X} = Z_0(\mathbf{I} + \mathbf{S})(\mathbf{I} - \mathbf{S})^{-1} = Z_0(\mathbf{I} - \mathbf{S})^{-1}(\mathbf{I} + \mathbf{S}) \quad (2\text{-}1)$$

where **R** and **X** are the resistance and reactance matrices respectively of the MEA, and **I** is the identity matrix with dimension equal to the number of the MEA elements.

2.2.2 Element radiation pattern, efficiency, directivity and gain

Mutual couplings between MEA elements change not only their impedances but also their radiation characteristics [53], i.e., the embedded element characteristics are different to their stand-alone characteristics. Therefore, the radiation behaviour of each MEA element must include the presence of the other elements and their terminations.

The **element radiation pattern (*h*)** refers to the far-field response in different directions of the radiating element. The **embedded element pattern** is the pattern when other elements are present. The terminations of the other

elements, e.g., whether they are loaded, open circuited or short circuited, impact the embedded element pattern.

The “pattern” of an antenna can refer to many quantities. For example, it can refer to a complex (amplitude and phase) vector field (both polarizations) pattern, a scalar amplitude or power pattern, a directivity pattern (i.e., scaled power pattern), or a gain pattern which is the directivity pattern scaled by the efficiency. Finally, these patterns are sometimes divided by their maxima to get normalized patterns.

The **element efficiency (η)** is well defined for a stand-alone element, but for an MEA, the embedded element has a different efficiency. In an MEA, power is transferred among elements through mutual coupling, so the efficiency seen at each element port is not only decided by the element loss, but also by mutual coupling and the losses of other elements of the MEA. However, the embedded element efficiency has no formal definition in the literature. This thesis includes a treatment of the efficiency of MEA elements.

The **maximum directivity (D_{max})** of an MEA element is defined in the usual way from the embedded pattern, and in this way the presence of other elements is accounted for.

The **maximum Gain (G_{max})** of an element is the product of its maximum directivity and efficiency. In practice, the “total efficiency” and “realized gain” are also of interest since they are related to the net power delivered into the port of the element. The total efficiency of an embedded element is also defined in this dissertation.

2.2.3 Distributed Gain and Mean effective gain

In line-of-sight communications, antennas preferably have a high gain to help maximize the signal-to-noise ratio. When the gain of a single antenna is insufficient, an array can be used to enhance the gain. On the other hand, in non-line-of-sight situations, there is often rich multipath, and the signals of interest are distributed over many directions and both polarizations. Antennas used in these scenarios should be capable of receiving signals from all directions, so fixed, high gain antennas are typically not suitable.

For this reason, the directive gain of an antenna in Section 2.2.2 is an important parameter in line-of-sight communications, but for non-line-of-sight it is not so useful for characterizing the antenna performance. The distributed gain [10][11][59], also called mean effective gain [60][63] when the directions are all of real space, is for this scenario.

The **distributed gain (*DG*)** can be used to measure the antenna transmitting and receiving capability in a given stochastic propagation environment, so it is a link gain (or the match between pattern and propagation environment) rather than a pattern parameter as in the directivity. It is defined as the ratio of the mean power received by the antenna to the mean power of the incoming waves, in both polarizations. The formulation for the distributed gain over the full sphere (called mean effective gain) is in [62], and is summarized as follows

$$DG = \frac{\text{antenna received power}}{\text{incident wave power}} \tag{2-2}$$

$$= \frac{\int_0^{4\pi} S_\theta(\Omega) G_\theta(\Omega) \mathrm{d}\Omega + \int_0^{4\pi} S_\phi(\Omega) G_\phi(\Omega) \mathrm{d}\Omega}{\int_0^{4\pi} S_\theta(\Omega) \mathrm{d}\Omega + \int_0^{4\pi} S_\phi(\Omega) \mathrm{d}\Omega}$$

$$= \frac{\int_0^{4\pi} \kappa_\theta p_\theta(\Omega) G_\theta(\Omega) \mathrm{d}\Omega + \int_0^{4\pi} \kappa_\phi p_\phi(\Omega) G_\phi(\Omega) \mathrm{d}\Omega}{\int_0^{4\pi} \kappa_\theta p_\theta(\Omega) \mathrm{d}\Omega + \int_0^{4\pi} \kappa_\phi p_\phi(\Omega) \mathrm{d}\Omega}$$

$$= \frac{XPR}{1+XPR} \int_0^{4\pi} p_\theta(\Omega) G_\theta(\Omega) \mathrm{d}\Omega + \frac{1}{1+XPR} \int_0^{4\pi} p_\phi(\Omega) G_\phi(\Omega) \mathrm{d}\Omega$$

where $G_\theta(\Omega) = \eta_{ant} \left| g_\theta(\Omega) \right|^2$, and $G_\phi(\Omega) = \eta_{ant} \left| g_\phi(\Omega) \right|^2$

$$S_\theta(\Omega) = \kappa_\theta p_\theta(\Omega),\ S_\phi(\Omega) = \kappa_\phi p_\phi(\Omega)$$

and $$XPR = \frac{\text{incident power in } \theta \text{ polar}}{\text{incident power in } \phi \text{ polar}} = \frac{\int_0^{4\pi} S_\theta(\Omega) \mathrm{d}\Omega}{\int_0^{4\pi} S_\phi(\Omega) \mathrm{d}\Omega} = \frac{\kappa_\theta}{\kappa_\phi}$$

where: Ω is the solid angle; $\mathrm{d}\Omega = \sin\theta \, \mathrm{d}\theta \, \mathrm{d}\phi$ is the elemental solid angle, and θ and ϕ are the zenith and azimuth angles, respectively; $p_\theta(\Omega)$ and $p_\phi(\Omega)$ are the θ and ϕ co-polar probability density functions of the incoming wave power, respectively, and so they are normalized as $\int_0^{4\pi} p_\theta(\Omega) \mathrm{d}\Omega = \int_0^{4\pi} p_\phi(\Omega) \mathrm{d}\Omega = 1$; $S_\theta(\Omega)$ and $S_\phi(\Omega)$ are the θ– and ϕ–polar angular power distribution of the incoming wave, respectively; κ_θ and κ_ϕ are the scale factors that satisfy $S_\theta(\Omega) = \kappa_\theta p_\theta(\Omega)$

and $S_\phi(\Omega)=\kappa_\phi\, p_\phi(\Omega)$; $g_\theta(\Omega)$ and $g_\phi(\Omega)$ are respectively the θ– and ϕ–polar vector field patterns normalized with $\int_0^{4\pi}(|g_\theta(\Omega)|^2+|g_\phi(\Omega)|^2)\mathrm{d}\Omega=4\pi$; $G_\theta(\Omega)$ and $G_\phi(\Omega)$ are respectively the θ– and ϕ–polar gain patterns, which are the corresponding power patterns ($|g_\theta(\Omega)|^2$ and $|g_\phi(\Omega)|^2$) weighted with the (same) antenna efficiency, η_{ant}. For MEAs, $G_\theta(\Omega)$ and $G_\phi(\Omega)$ represent the embedded element gain patterns; *XPR* is called the cross polar ratio. Here it is the ratio of the total θ–polar incident power to the total ϕ–polar incident power, and it is not angularly dependent. When the antenna efficiency is unity, the distributed gain is the same as the **distributed directivity**.

If *XPR* is unity (same incident power in each polarization), and the direction of interest reduces to a singularity or a ray (the incoming wave probability function for the singular direction is, here for the θ polarization, $p_\theta(\theta,\phi)=\delta(\theta-\theta_0)\,\delta(\varphi-\varphi_0)/\sin(\theta_0)$), then the distributed gain reduces to half of the classical gain. This can be written as $DG(\Omega_0)=\eta_{pol}G(\Omega_0)$ where η_{pol}=0.5, is the polarization efficiency.

For another case when *XPR*=1 and the incoming waves are uniformly distributed over the sphere in each polarization ($p_\theta(\theta,\phi)=p_\phi(\theta,\phi)=1/(4\pi)$), the mean effective gain of any antenna is half of the antenna efficiency where the factor of half is the polarization efficiency.

2.2.4 Correlation coefficient matrix

The correlation coefficient of two antenna elements refers to the normalized covariance of the signals received at the element ports, when a carrier is transmitted. It gives the degree of similarity of the fading signals at the ports caused by the multipath propagation and by the antennas including their mutual coupling. Based on the theory of reciprocity, the correlation coefficient matrix of a transmit MEA can be obtained from the receive MEA.

The **correlation coefficient matrix (ρ)** of an MEA includes the correlation coefficients of the antenna elements corresponding to the indices in the matrix. For example, ρ_{11} is the normalized auto-covariance (also auto-correlation) of the signal received at the 1st element, and it is unity. ρ_{23} is the normalized cross-covariance (also cross-correlation) between the signals received at the 2nd and the 3rd elements of the MEA, and its magnitude is between zero and unity. To achieve good diversity and capacity performance, the correlation coefficient between any two MEA elements is desired to be low. For signals with envelopes following a Rayleigh distribution, the envelope correlation coefficient, ρ_e, can be approximated from the correlation coefficient of the signals [64] as

$$\rho_e \approx |\rho|^2 \tag{2-3}$$

It has been reported that ρ_e<0.7 for base station and ρ_e<0.5 for mobile station are acceptable figures for good antenna diversity performance [12].

Different terminations of the MEA ports change the received voltages, and these voltages define different correlations. Correlations from open circuited and loaded terminations are given as follows.

A) Open circuit voltage correlation coefficient matrix of an MEA (ρ_O)

When an antenna element is open-circuited, the voltage excited by the incident wave is the function of the impinging wave and the antenna effective height (which is the complex far field pattern of the element). The open circuit voltage at the port of the *i*th antenna element can be found (*cf.* [59]) as

$$V_{O,i}(t) = \int_0^{4\pi} h_{O,i}(\Omega) \cdot E(\Omega,t)\ \mathrm{d}\Omega \tag{2-4}$$

where $h_{O,i}$ (Ω) is the embedded far field receive pattern of the *i*th element measured when other elements of the MEA are present and open circuited; and $E(\Omega,t)$ is the incident field, which may vary with time index *t*.

The open circuit voltage correlation coefficient ($\rho_{O,ij}$) between the *i*th and *j*th element is defined as the normalized covariance of the open circuit voltages:

$$\rho_{O,ij} = \frac{E\{(V_{O,i} - \overline{V_{O,i}})(V_{O,j} - \overline{V_{O,j}})^*\}}{\sqrt{E\{|V_{O,i} - \overline{V_{O,i}}|^2\}\ E\{|V_{O,j} - \overline{V_{O,j}}|^2\}}} \tag{2-5}$$

which is also the normalized correlation since the means are zeros. E{ } is the expectation operation over time or space.

When the MEA elements are open-circuited, they can each be considered as a voltage source in a network model, and $\boldsymbol{\rho_O}$ becomes the correlation matrix of the sources' signals.

B) Loaded circuit voltage correlation coefficient matrix ($\boldsymbol{\rho_L}$)

Likewise, the loaded circuit voltage for terminated MEA elements ($V_{L,i}$) is calculated as in Eq. (2-4), but using the embedded complex far field pattern, $h_{L,i}$ (Ω), measured when other elements of the MEA are present and also terminated. $\boldsymbol{\rho_L}$ is defined in the same way as in Eq. (2-5) that

$$\rho_{L,ij} = \frac{E\{(V_{L,i} - \overline{V_{L,i}})(V_{L,j} - \overline{V_{L,j}})^*\}}{\sqrt{E\{|V_{L,i} - \overline{V_{L,i}}|^2\}\, E\{|V_{L,j} - \overline{V_{L,j}}|^2\}}} \tag{2-6}$$

Since $\boldsymbol{\rho_O}$ can be interpreted as the correlation matrix of source signals, $\boldsymbol{\rho_L}$ can be found from $\boldsymbol{\rho_O}$ if the impedances are known. Denoting $\mathbf{Z_A}$ as the MEA impedance matrix and $\mathbf{Z_L}$ as the loading circuit impedance matrix, then as derived in [12]

$$\boldsymbol{\rho_L} = \mathbf{F}\boldsymbol{\rho_O}\mathbf{F}^{H}, \qquad \text{where } \mathbf{F} = \mathbf{Z_L}(\mathbf{Z_A} + \mathbf{Z_L})^{-1} \tag{2-7}$$

With these stochastic definitions, the correlation matrix of an MEA can be calculated from time-series measurements of the voltage signals, as in Eqs. (2-6) and (2-7). In practice, time-series measurement for MEA correlation estimation is difficult, expensive and time consuming. Also, the results depend on many other factors, such as the measurement details (sampling rate, sample size, etc.)

which are not related to the antenna itself. Another problem is that even with a consistent measurement set-up, repeating the measurement is seldom possible. Therefore, time-series evaluation, although it processes the real-world quantity that we are pursuing in order to characterize the antenna, is not very convenient. The convenience is important for design because the MIMO antenna design process is often iterative.

Instead, under sufficient assumptions, several approaches to estimate MEA correlation with antenna field patterns and circuit parameters have been proposed, as follows.

2.2.4.1 Embedded field pattern approach

The approach of estimating antenna correlation using field patterns in various propagation environments is discussed in, for example, [11][12][65]-[69]. The principal assumption of this method is that the electrical size of the MEA is small enough to consider that all the elements are in the same propagation environment, i.e., the incident wave distribution is identical at each element. In mobile communications scenario, the devices are typically small relative to the distance to the scatters, so this assumption is likely to be satisfied. Another assumption is that the incoming waves are angularly uncorrelated, and uncorrelated between polarizations.

With this method, correlation coefficient between the *i*th and *j*th element of an MEA is approximated with their embedded far field patterns weighted by the distribution of incident power in a given propagation environment as

$$\rho_{i\,j} = \frac{\int_0^{4\pi} H_{i,\,j}(\theta,\phi)\, d\Omega}{\sqrt{\int_0^{4\pi} H_{i,\,i}(\theta,\phi)\, d\Omega}\sqrt{\int_0^{4\pi} H_{j,\,j}(\theta,\phi)\, d\Omega}} \tag{2-8}$$

where,

$$H_{i,\,j}(\theta,\phi) = XPR\; h_{\theta,\,i}(\theta,\phi)\, h^{*}_{\theta,\,j}(\theta,\phi)\, p_{\theta}(\theta,\phi) \;+\; h_{\phi,\,i}(\theta,\phi)\, h^{*}_{\phi,\,j}(\theta,\phi)\, p_{\phi}(\theta,\phi)$$

XPR is the cross polarization ratio as defined in Eq. (2-2), $h_{\theta,\,i}$ and $h_{\phi,\,i}$ are the *i*th antenna open-circuited or loaded embedded far field patterns for open or loaded circuit voltage correlation respectively. As defined in Eq. (2-2) $p_{\theta}(\Omega)$ and $p_{\phi}(\Omega)$ are the θ– and ϕ–polar of the probability density functions of the power of the incoming waves, respectively. Statistical modelling of $p_{\theta}(\Omega)$ and $p_{\phi}(\Omega)$ is an ongoing research subject, *cf.* [70][72] and some simplified models, for example, are summarized in [66]. Here, Eq. (2-8) shows that both the embedded pattern and the distribution of incoming waves govern the antenna correlation.

This pattern method is repeatable, and different propagation environments can be included by using modelled incident power distributions. But the drawback is that the pattern measurement requires an antenna chamber which is expensive. Patterns from modelling software are generally reasonably reliable, but there is always the danger of a modelling error. With further assumptions, another two alternative methods to estimate MEA correlation with circuit parameters have been proposed, which are less expensive, but they can only be applied to the case of the incoming wave distribution being uniform (or at least

uniform of the directions of significant pattern gain), and uncorrelated in angle and polarization.

2.2.4.2 Impedance approach

For Minimum Scattering Antennas (MSAs) [73] in the uniform scenario, [11] proposed that the open circuit voltage correlation coefficient of an MEA can be approximated from the normalized mutual resistance as

$$\rho_{O,i,j} \approx \rho_{O,Z,i,j} = \frac{R_{i,j}}{\sqrt{R_{i,i}R_{j,j}}} \tag{2-9}$$

where $\rho_{o,i,j}$ is the open circuit voltage correlation coefficient between the *i*th and *j*th elements; $\rho_{o,z,i,j}$ is the estimation of $\rho_{o,i,j}$ with the impedance method, which is the mutual resistance, $R_{i,j}$, normalized by the self resistances $R_{i,i}$ and $R_{j,j}$. The mutual and self resistances are from the MEA impedance matrix, $\mathbf{Z}=\mathbf{R}+j\mathbf{X}$. **Z** can be calculated from the scattering parameter matrix, **S** with Eq. (2-1).

With Eqs. (2-7) and (2-9), the loaded circuit voltage correlation coefficient can also be estimated with this method.

2.2.4.3 Scattering parameter approach

Stein [74] included the scattering parameter matrix **S** with the field pattern correlation for lossless antennas in uniform distribution scenario. This method was summarized in [75][76], and then later it is utilized in many publications to estimate loaded circuit voltage correlation as

$$\boldsymbol{\rho}_L \approx \boldsymbol{\rho}_{L,S} = \mathbf{I} - \mathbf{S}^H\mathbf{S} \tag{2-10}$$

where $\boldsymbol{\rho}_{L,S}$ denotes the estimation of $\boldsymbol{\rho}_L$ with scattering parameter method, and $()^H$ is the Hermitian operation.

The impedance and scattering parameter methods share the assumptions of lossless antenna and a uniform distribution propagation scenario. The impedance method has an even further assumption that the MEA elements are MSAs. Therefore, as long as the assumptions apply, both methods should yield similar results to the antenna field pattern correlation. However, these three methods have not been compared and the equivalence has not been checked in the literature. This is undertaken through measurement and simulation in this dissertation.

To summarize, antenna correlation usually refers to the time series correlation of the received signals, or rather the modulation imposed on the transmitted signal by the multipath channel. This is hard to measure accurately, requiring extensive time series analysis, and the results from such a measurement can only be repeated in a loose statistical sense. The accuracy is further complicated by the presence of noise. If the signal cannot be separated from the noise (usually impossible), then the time series measurement data is affected by ohmic loss in the antenna, because the *SNR* can be affected by it. This is clear from the limiting case of zero antenna efficiency, where a measured signal correlation will reflect only the (un)correlation of the noise which is in the signal path. Only if the signal can be separated from the noise, then the

measured correlation of the signals will be independent of the losses, or antenna efficiency.

Under certain conditions, the correlation can be estimated by the "correlation" (inner product) of the embedded antenna patterns. This measure is deterministic. The field pattern correlation is not strongly affected by the ohmic loss in the antenna, but may well be affected by the changes to the environment, including the presence of a user. In this dissertation we refer to the correlation as the signal correlation, and consider that the pattern correlation is a good approximation to this. In practice, the inner product of the patterns weighted by the local distribution of incoming waves gives the local correlation. But the issue is that the incoming wave distribution is changing with time and position. Therefore, an averaged (over time and position) incoming wave distribution, *i.e*. a modelled pdf, is used, and this relates directly to a statistical correlation. Knowing the patterns is therefore very important. If the patterns are known for given terminations (sum of element patterns weighted by the resulting excitations), then the patterns can be calculated for any termination via the modified excitations.

2.2.5 Bandwidth and compactness

The **bandwidth** of a single element antenna is the frequency range in which the antenna's performance (including patterns, input impedance, beamwidth, polarization, etc.) reaches a satisfactory level. If not specified, it normally refers to **impedance bandwidth** - the frequency range within which the reflection coefficient at the antenna feed point is below, say, -10dB or -3dB.

However, there is no commonly agreed definition of impedance bandwidth for MEA in literature. A reasonable definition proposed in [77] is to take the frequency range over which all the scattering parameters $S_{i,i}$ and $S_{i,j}$ are under a certain value (e.g., -10dB) to be the bandwidth of the MEA. In other words, it is the overlap of the element bandwidths. It is not hard to imagine that there may be no such overlap in an initial MEA design, and then the bandwidth of the MEA is zero.

There is a special class of array structures which are element-symmetric in the sense that each element sees an identical structure of elements around it. For this kind of symmetric MEA, it is likely that the element bandwidths are the same or very similar, and in this case, the element impedance bandwidth can be a reasonable approximation of the system impedance bandwidth as well.

Similar to impedance bandwidth, **correlation bandwidth** is the frequency range in which all the correlation coefficients between any two antenna elements are under certain value, e.g., envelope correlation coefficient ρ_e<0.7 [11]. Within this frequency range, the diversity performance of the MEA can be considered acceptable.

To evaluate the **compactness** of a single element antenna, the trade-off between the **quality factor** and the **electrical size** of the antenna can be used. The quality factor is approximately proportional to the inverse of -3dB impedance bandwidth at the antenna resonance, *cf*., [78][79]. The electrical size of the antenna is usually described with the electrical size of the spherical volume inscribing the antenna. Recently, arbitrary volumes have been treated [13][80].

Chu and MacLean limits [14][81] are the bounds of quality factor for lossless antennas with given enclosing spherical electrical sizes. These limits also give upper bounds of impedance bandwidth.

MEAs are of course more complicated than single elements. To significantly improve MIMO communications performance, a larger number of elements are required which in turn requires a larger volume. There is no standard for the evaluation of **MEA compactness**. A step in this direction is to develop a space efficiency measure for an MEA and its trade-off with the MEA communications performance, presented in this dissertation.

2.2.6 Diversity combining methods and diversity gain

Antenna diversity uses MEAs to transmit and/or receive replicas of the same signal. The transmitted copies of the signal go through different propagation paths, and arrive at the receivers at different times. The received copies of the signal are then selected or combined in the ways that deep fades can be avoided and the signal can be recovered. Popular combining methods (*cf.* [12]) include Optimal Combining (OC), Maximum Ratio Combining (MRC), Equal Gain Combining (EGC), Selection Combining (SC), Switched Combining (SwC), etc.

Pattern diversity includes: spatial diversity (spacing the antenna elements apart); polarization diversity (using orthogonal polarizations); angular diversity (using patterns with different directional coverage). Examples of spatial diversity

include [28][29][31][32][46], polarization diversity, [41][5], and for angle diversity, [41][43][44][47][49][5].

Diversity performance of an MEA is measured by its diversity gain [12], G_{div}. There are several definitions for diversity gain. From the communications literature, a popular form is to model the channel gain as $(G_{coding}\,SNR)^{-G_{div}}$ at high *SNR* so that the slope of the function gives the diversity gain (and G_{coding} is a coding gain, seen as a translation of the curve along a dB *SNR* axis). But such a simple slope metric alone is insufficient to capture the complete gain garnered from diversity action. A more complete definition is conveniently read from cumulative density function (*CDF*) plots of *SNR* [12]. Here, the diversity gain at a given probability is defined as the improvement in *SNR* expressed in dB,

$$G_{div}(\text{dB}) = [\frac{\gamma_c}{\Gamma}(\text{dB}) - \frac{\gamma_{ref}}{\Gamma_{ref}}(\text{dB})\,]_{\text{given probability}} \tag{2-11}$$

where, γ_c is the instantaneous *SNR* of the combined received signal. Γ is the mean *SNR* on one MEA receiving branch. Similarly, γ_{ref} and Γ_{ref} are respectively the instantaneous and mean *SNR* received by a single element reference antenna. When the MEA has equal mean *SNR*s on each branch, and when these branch mean *SNR*s are the same as the mean *SNR* of the reference antenna ($\Gamma = \Gamma_{ref}$), Eq. (2-11) reduces to $G_{div}(\text{dB}) = [\gamma_c(\text{dB}) - \gamma_{ref}(\text{dB})\,]_{\text{given probability}}$. This shows that the diversity gain is the improvement in receive *SNR* of the diversity MEA over the *SNR* of a reference single branch.

Note that this definition of diversity gain depends on the choice of the probability and the choice of the reference antenna element. There are several options for the reference element. For example, it can be one of the MEA's elements mounted in the device, but with the other elements removed [82]. In this case, the diversity gain gives the *SNR* improvement from a single element system to a multiple element diversity system in the same device. Another option is to take the element with the highest mean *SNR* as the reference antenna, while the other elements remain present. Or the reference element can be a separate antenna, such as a dipole, or an idealized lossless element with isotropic pattern for analysis or simulation. The choices of probability and reference antenna need to be specified in a study of diversity performance.

Factors affecting γ_c include the propagation channel characteristics, the diversity combining method, the MEA total efficiency, and the correlation coefficient between each element. The total efficiency of each element acts to reduce the *SNR* value. Changing propagation channel characteristics may change the antenna correlations, but do not change the MEA efficiencies. Using the embedded element far field patterns and knowledge of the propagation scenario, the antenna correlations can be found from the approaches in Section 2.2.4 for diversity performance analysis.

G_{div} can be estimated from time series measurements in real-world propagation environments, e.g., indoor, urban, etc. This is the best estimation technique in the sense that the real-world behaviour is being sampled. But it is a complex and expensive measurement, and care must be taken with the

averaging, i.e., the experiment must cover all the propagation environments for a proper estimate. Moreover, the mobile antenna must be moved, e.g., translated, rotated, etc., in a realistic way, and be deployed appropriately - a major exercise for handheld terminals which are held in various orientations and distances from reflecting and absorbing objects including body tissue [83]. In such measurements, an observation from one environment may not match well with another observation from a different environment, or with an ensemble average.

Another physical measurement method is to create an artificial incoming wave distribution, typically striving for uniform and uncorrelated scattering [84]. It is useful for measuring the distributed gain (or mean effective gain) of an antenna when it is not possible to measure the patterns. A reverberation chamber is often used, but these, as for a pattern measurement chamber, can be expensive. It is noted that comparative performance does not necessarily reveal how to improve the terminal performance.

Based on signal statistics, a simple and general signal processing approach is used to calculate the diversity gain for different diversity combining methods, as summarized below.

For a lossless and uncorrelated diversity MEA in a Rayleigh fading scenario, if all the antenna branches have equal mean *SNR*s (Γ), the MRC *CDF* is given in [10] as

$$CDF(\gamma \le \gamma_c) = 1 - e^{-\gamma_c / \Gamma} \sum_{k=1}^{N} \frac{(\gamma_c / \Gamma)^{(k-1)}}{(k-1)!} \tag{2-12}$$

where *N* is the number of the antenna branches.

For a lossless and correlated MEA with MRC in the same propagation scenario, the correlation matrix ($\boldsymbol{\rho}$, estimated with either of the methods mentioned in Section 2.2.4) has singular values which correspond to the mean power in the equivalent uncorrelated antenna branches. The singular values can be found, for example using singular value decomposition (SVD), as [12][85]

$$\boldsymbol{\Lambda} = [\lambda_1 \ \lambda_2 \cdots \lambda_M]^T = \mathrm{SVD}(\boldsymbol{\rho}) \tag{2-13}$$

where *M* is the number of non-zero effective branches, and it can be equal to or less than the number of antenna branches (*N* in Eq. (2-12)). $\boldsymbol{\Lambda}$ is a *M*×1 column matrix comprising the singular values, $\lambda_{m\ (m=1,\ \ldots,M)}$. With this decomposition, the correlated antenna branches are orthogonalized into equivalent uncorrelated branches with different mean branch *SNR*s as $\Gamma\lambda_{m\ (m=1,\ \ldots,M)}$. Here, Γ, as defined in Eq. (2-11) and (2-12), is the mean *SNR* of uncorrelated and equal power branches with lossless antennas. $\lambda_{m\ (m=1,\ \ldots,M)}$ are caused by the correlation of the branches and act to weight Γ for different equivalent branches. The equivalence refers to the total power received by the branches.

The *SNR* probability density function of the combined signal in Rayleigh channels combined with MRC is given in [10] as

$$p(\gamma) = \frac{1}{2\pi j}\int_{c-j\infty}^{c+j\infty} \frac{e^{s\gamma}}{\prod_{m=1}^{M} 1+s\Gamma\lambda_m} ds = \sum_{k=1}^{K} res_k(\gamma), \qquad c \geq 0 \tag{2-14}$$

where *K* is the number of poles in the Laplace space, and the *k*th residue is

$$res_k(\gamma) = \frac{1}{(n-1)!} \lim_{s->\frac{-1}{\Gamma\lambda_k}} \frac{d^{n-1}}{ds^{n-1}} \left(\frac{e^{s\gamma}}{\prod_{m=1}^{M} 1+s\Gamma\lambda_m} \left(s + \frac{1}{\Gamma\lambda_k} \right)^n \right) \tag{2-15}$$

and *n* is the order of the pole, meaning that there are *n* uncorrelated branches with the same *k*th mean *SNR*, $\Gamma\lambda_k$.

The MRC *CDF* follows from

$$CDF(\gamma \leq \gamma_c) = \int_0^{\gamma_c} p(\gamma)\, d\gamma \tag{2-16}$$

For the case when the equivalent uncorrelated branches have different mean power (the orders of all the poles are one, and thus *K*=*M*) the MRC *CDF* simplifies to [12]

$$CDF(\gamma \leq \gamma_c) = \sum_{k=1}^{M} \frac{1}{\prod_{\substack{m=1 \\ m\neq k}}^{M} (1-\frac{\lambda_m}{\lambda_k})} (1-e^{-(\gamma_c/\Gamma)/\lambda_k}) \quad \text{for } K=M, \lambda_m \neq \lambda_k \tag{2-17}$$

The *CDF*s of some other combination techniques are available in [10][12]. For example, the *CDF* of Selection Combining (SC) for lossless and correlated MEA in a Rayleigh environment is

$$CDF(\gamma \le \gamma_c) = \prod_{k=1}^{M} (1 - e^{-(\gamma_c / \Gamma)/\lambda_k}) \tag{2-18}$$

Fig. 2.1 demonstrates the impact of MEA correlation on MRC G_{div} with a 3-element, lossless and correlated example MEA, whose correlation matrix is

$$\rho = \begin{bmatrix} 1 & 0.7 & 0.4 \\ 0.7 & 1 & 0.6 \\ 0.4 & 0.6 & 1 \end{bmatrix}$$

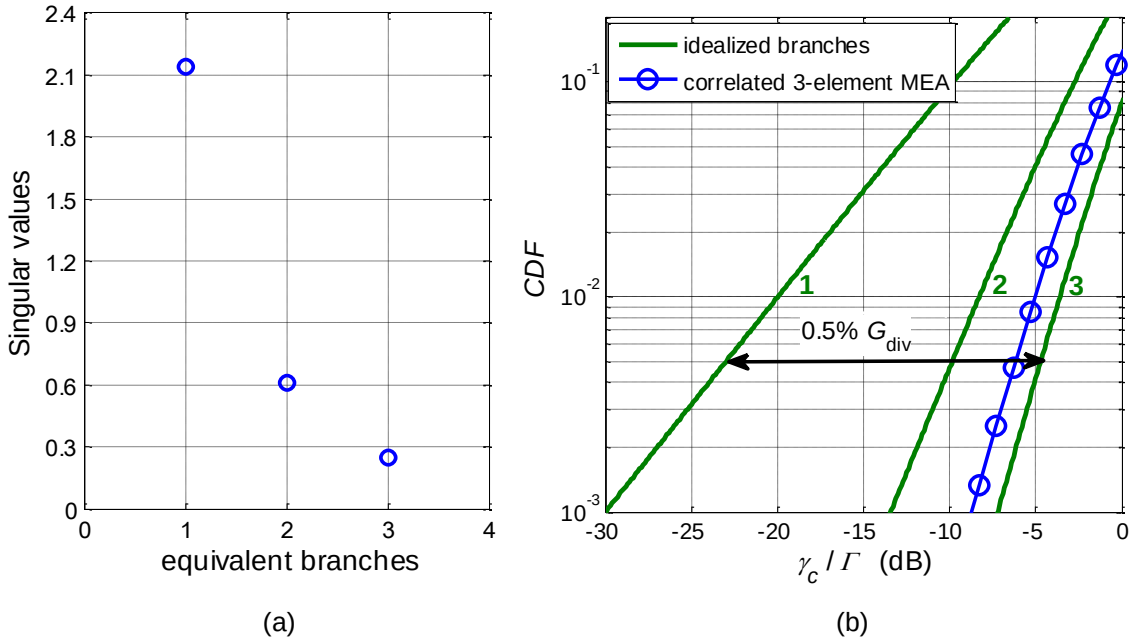

Figure 2.1 Impact of MEA correlation on MRC G_{div}

(a) Singular values of a lossless, correlated 3-element MEA; (b) G_{div} of idealized MEAs and the lossless, correlated 3-element MEA

In Fig. 2.1(a), the singular values of correlation coefficient matrix of the example MEA are obtained with Eq. (2-13). The sum of the singular values is 3

(the same as the number of the elements) owing to the power constraint (the SVD transform is energy conserving) of this lossless MEA. Fig. 2.1(b) compares the MRC *CDF* curve of the correlated example MEA with the ones of some idealized (lossless, uncorrelated, equal branch power) MEAs. Taking the curve for the single element idealized antenna as the reference, G_{div} is indicated for the probability of 0.5%. It shows that, at the 99.5% reliability level, the idealized 3-element MEA has an 18dB *SNR* increase compared to the reference antenna. In comparison, the correlated 3-element MEA has a 16dB increase. Therefore, there is 2dB *SNR* lost in the diversity gain owing to the correlation between the MEA elements.

There are several factors affect G_{div}, including diversity combining methods, propagation channel characteristics, MEA correlation coefficient and total efficiency. For some of the diversity combining methods, e.g. MRC and SC, closed form formulations to calculate G_{div} are summarized in [12]. The effect of propagation channel characteristics on G_{div} is not considered as an antenna effect, but with the Kronecker model [86] it can be included in the correlation coefficient matrix. The impact of correlation on G_{div} is demonstrated in Fig. 2.1.

MEA total efficiency acts to reduce *SNR*. As a consequence, G_{div} is reduced. The signal processing approach with Eqs. (2-12) – (2-18) does not include the effect of antenna loss. In this dissertation, antenna loss is taken into account, and the signal processing evaluation of G_{div} is revised.

2.2.7 MIMO capacity

There is some confusion over the term of *capacity*, and an explanation is useful for how it is used in this thesis. In many information-theoretic contexts, the units of capacity are bits per channel use. In practice, the units of capacity are expressed as bits per second per Hertz. In some information theoretic articles, this bandwidth (in Hertz) often refers only to the idealized baseband signal, whereas in practice, the need for guard bands, etc., make the required RF bandwidth much larger. In the traditional communications literature, the channel capacity bandwidth efficiency is often denoted "*C*/*B*", called the *channel efficiency*, and here the "*C"* is in bits per second and the "*B*" in Hertz. For simplicity, following much of the recent literature, in this dissertation, the MIMO capacity bandwidth efficiency is simply called *capacity*, denoted as *C*, with the unit of bits per second per Hertz.

Eq. (1-1) describes spectral efficiency of an n_T transmit and n_R receive system in a given channel. The channel transfer matrix, *H*, contains the information of the channel, which includes the propagation channel, as well as the transmit and receive antennas. Depending whether *H* is known to the transmitter, the implementation of the MIMO system can be different.

A) *H* unknown

When the channel is unknown at the transmitter, the total transmitted power P_T is equally divided between each transmit branch as P_T/n_T. The channel capacity is summarized in [87]

$$C = \log_2 \det[I + \frac{P_T}{n_T \sigma_N^2} HH^H] \quad (2\text{-}19)$$

where σ_N^2 is the noise power. Here H includes the path gains of the channels, and often it is scaled to have unit variance for convenience in the signal processing.

B) *H* known

If the transmitter has knowledge of the channels, then eigen-MIMO is possible. The channels are decomposed into equivalent orthogonal channels (eigenchannels) with singular value decomposition. Each singular value of HH^H, λ_k, is the power gain of the corresponding equivalent eigenchannel. Then the MIMO channel capacity becomes the sum of the capacity of each eigenchannel in the form of the parallel channels formula of Gallagher, as [12][88] as

$$C = \sum_{k=1}^{K} \log_2(1 + \lambda_k \frac{P_k}{\sigma_N^2}) \quad (2\text{-}20)$$

where P_k is the power assigned to the kth eigenchannel determined by water filling (Gallagher, 1968), and P_k / σ_N^2 is the *SNR* referred to the transmitter of the k-th eigenchannel. K is the total number of the eigenchannels.

In a communications system, the channel information is estimated on the fly, often using pilot symbols for channel sounding. For evaluating a system, the channel information can be either estimated from field measurements of the channels, or simulated with physical propagation channel models [89] such as

ray-tracing and proposed standard Spatial Channel Models (SCMs) [90], or approximated with analytical models such as Kronecker model [86].

1) *Field measurement*: Field measurement of the channel matrix has been of interest [91]-[97]. As with other time series measurements, it is an expensive process. It uses test beds, which include antennas, IF/RF frequency converters, DSP processors, etc., at both ends of the channels. Antenna effects, such as patterns and mutual coupling, are therefore included in the measured channel matrix. The measured channel matrix can be normalized by post processing such as removing the average path loss, and be demeaned by removing a local average (removes the long term variation) to keep the short-term, Rayleigh-like fading.

2) *Physical channel models*: As summarized in [89], physical channel models reproduce channel matrices based on multipath wave propagation mechanisms. Ray tracing models and SCM are two different approaches for different propagation environments. Ray tracing models is used in the environment where the wavelengths are much shorter than the sizes of the obstacles, so geometrical optics can be used. Ray tracing models are usually used in urban environments and more recently indoor environments for 60GHz systems. SCM is a stochastic model for outdoor environments. It can reflect the physical reality better in the way that scatterers are randomly placed and important parameters such as phases, time delays, Doppler frequency, angle of departure (AOD), angle of arrival (AOA), and angular spread, etc. can be defined. The channel matrix can therefore be reproduced with a stochastic

process. It is important to mention that in many of these systems, antenna effects are excluded from the channel matrices for these two physical channel models.

3) *Analytical models:* Kronecker model [86][98]-[101] assumes that the transmit and receive antenna correlation matrices (R_{Tx} and R_{Rx} respectively) can be separable, under the reported assumptions that all antenna elements at both ends of the MIMO link have the same polarization and the same radiation pattern. In a complex Gaussian i.i.d. propagation channel ($H_{i.i.d}$), the correlation matrix of the total channel R_H (including the transmit and receive antennas and the i.i.d. channel) is the Kronecker product

$$R_H = R_{Tx} \otimes R_{Rx} \quad , \quad \otimes \text{denotes Kronecker product} \tag{2-21}$$

The total channel matrix can then be found as

$$H = R_{Rx}^{1/2} H_{i.i.d.} R_{Tx}^{1/2} \tag{2-22}$$

For channels other than complex Gaussian i.i.d., R_{Tx} and R_{Rx} are found from, say, Eq. (2-8), for a given antenna and propagation scenario, then the complex Gaussian i.i.d. channel model can still be applied using Eq. (2.22). Hence the Kronecker model provides a convenient way to evaluate the impact of Tx and Rx correlation on channel capacity in different propagation environments.

However, the accuracy of the method of Kronecker model has been questioned [102], and the model needs to be revised for polarization diversity, according to [103]. But the Kronecker model appeals because it allows

independent optimization at Tx and Rx, and is a simple, repeatable way to evaluate the MIMO capacity performance in known channels.

Over the air (OTA) measurements are currently of interest, and here the communications terminal is tested for its communications capability (includes antennas, detection algorithms, etc.), not just its electromagnetic performance.

In the above capacity analyses provided in the literature, the impact of antenna efficiency on the MIMO capacity has not been thoroughly addressed. Although in [104] the impact of averaged efficiency over all the elements was discussed in a Rayleigh fading scenario, an important part of the MEA efficiency for compact designs – mutual coupling loss – is omitted. Also, averaged efficiency is used in [104], and the case when the elements have different efficiencies is not discussed. In this dissertation, the efficiency of each element is considered, and their impact on MIMO capacity is investigated and formulated.

From the review on currently available MIMO antenna evaluation techniques in the literature, the missing but important aspects of MIMO antenna evaluation techniques are summarized here, including: 1) comparison of the three different antenna correlation coefficient estimation approaches; 2) space efficiency for MEA compactness measure and its trade-off with the MEA performance; 3) defining the efficiencies of MEA elements with consideration of all aspects which impact the power loss of MEA elements; 4) the impact of MEA efficiency on diversity gain and capacity, etc.

2.3 Review on slot antenna and its usage in literature

In much of the literature, a slot antenna is considered in an infinitely large groundplane, and then treated as a magnetic dipole with the same total power pattern but with the orthogonal polarization compared to its complementary strip dipole.

Based on Babinet's principle, Booker's relation provides a link between the impedance of a slot antenna and the impedance of its complementary electrical dipole [105]. However, Booker's relation for the slot antenna requires three frequently overlooked conditions: the planar groundplane must be infinitely large, infinitesimally thin, and perfectly conducting. In a practical implementation, all three conditions are violated. It has been found in [52] that for an open slot (which has no cavity so radiates to both sides of the groundplane) the impedance can be predicted reasonably well from Booker's relation when the edge of the groundplane is more than a wavelength away from the slot. In other words, the size of the groundplane needs to be large – typically more than two wavelengths for maintaining the Booker's relation. Long [106] gives physical measurement results for a $\lambda/2$ slot near its first resonance in a 4.8-wavelength groundplane, and shows that the Booker relation holds well for this configuration.

Slot antennas have been widely used in arrays fed by waveguides, e.g. in [107]-[109], or with microstrip feeds, e.g. in [110]-[112]. However, slots have not been widely used as practical, stand-alone antennas. This is because slot elements have been generally considered at their first resonance where their impedance is very high, and a large groundplane is required. Some designs of

stand-alone slot antennas have been presented, e.g. in [113]-[117], but little analysis or radiation mechanism has been discussed, and no study has been reported on the impact of groundplane size.

To apply the slot as an element in practical MEAs, it is appropriate to have a complete study of stand-alone slot in a finite groundplane, including the effects of the rectangular slot shape, rectangular groundplane shape and size, and the impact of mutual coupling between the slot elements in the same groundplane. Such a study is undertaken in this dissertation.

CHAPTER 3: MEA EFFICIENCY AND IMPACT ON DIVERSITY AND CAPACITY

A desirable characteristic of an MEA is to be compact. But as an MEA becomes more compact it tends to have higher ohmic and mutual coupling losses. A metric for the efficiency of the MEA would help clarify the tradeoff between compactness and performance.

In this chapter, MEA efficiencies are discussed and formulated in the context of mutual coupling and diversity combining. In a MIMO/diversity antenna, the total efficiency seen at each port contributes directly to the *SNR* in the diversity branch. The *SNR* after diversity combining governs the performance of the antenna system.

The impact of MEA efficiency on the diversity gain and the information theoretical capacity is also formulated and demonstrated using the measurements of example MEAs. With these formulations, an equivalent number of idealized (lossless, uncorrelated, uncoupled, equal power) branches can be found for an MEA, and this defines the diversity order and the capacity order of the MEA. With this metric, the performance of different MEAs can be compared.

3.1 Introduction

Efficiencies of single element antennas are well understood and defined in IEEE Standards [1][27]. But for an MEA used for MIMO communications,

definitions of efficiencies are not yet clarified. Since power is transferred between elements through mutual coupling, the antenna efficiencies of MEA elements are not only decided by the element loss, but also by the mutual coupling and the diversity combining method which includes the terminations. A formulation of the MEA efficiency needs to include these effects, and it should apply to both the transmit case and the receive case.

The efficiency of each element directly impacts the MEA transmitting and receiving capability. In an MIMO system, the *SNR* of an element is proportional to the efficiency of the element. The combination of the element *SNR*s governs the antenna diversity gain and its capacity performance.

How the MEA efficiency impacts the MEA performance in a Rayleigh fading scenario is discussed in [104], but an important part of the MEA efficiency for compact designs - mutual coupling loss - is omitted in order to study the impact of efficiency caused by the element ohmic loss and impedance mismatch loss only. Also, the averaged efficiency and the highest efficiency among the elements have been recently used (*cf*. [104] and [118], respectively). But these treatments do not consider the impact of each element when their efficiencies are different. Often, MIMO antennas must be mounted on complex platforms. The available space can be critical and the designer may be forced to use different types of elements. In fact, different types of elements are often deployed in order to reduce correlation and mutual coupling. Different element types normally have different radiation efficiencies. In some implementations, this difference can be up to 6dB.

The problem has been approached from rigourous network theory. This approach does not explicitly formulate a definition of the efficiency, but the efficiency is included in the formulation [15][119][119].

This dissertation develops efficiency formulations for MEAs. The formulation ensures that the ***embedded element transmit efficiency*** and the ***embedded element receive efficiency*** are the same, as should be expected from the principle of reciprocity. Also, we use the reciprocal terms ***total transmit/receive efficiency of the embedded element*** for the total efficiency of the embedded element. The loss due to mutual coupling, which can be a dominant part of the antenna loss, changes with the type of diversity combining and the terminations of the elements. Therefore, the formulation of the efficiencies considers the embedded element losses with different diversity schemes.

An ***MEA total efficiency****,* in the form of a matrix containing the total efficiency of each embedded element, accounts for the impact of individual element efficiencies on the diversity gain and capacity. The impact agrees with a published example. By comparing these performance metrics before and after the MEA total efficiency is included, the impact of antenna efficiency is separated from the impact of antenna correlation. The formulation is not limited to Rayleigh channels but Rayleigh channels are used in the examples.

The rest of chapter is laid out as follows. Section 3.2 develops the efficiency formulations for an MEA. Section 3.3 takes the derived efficiency and

incorporates it into the MEA diversity gain, and Section 3.4 does the same for the information theoretic capacity. Section 3.5 concludes the chapter.

3.2 Embedded element efficiencies of MEA

For single element antennas, the radiation efficiency is expressed in terms of the transmit case. It is well-established and features in Standards [1][27]. The receive efficiency is identical to the transmit radiation efficiency for reciprocal antennas. From a simplified circuit model, the radiation efficiency is normally written as $\eta_{rad} = R_{rad} / (R_{rad} + R_{\Omega})$, where R_{rad} is the radiation resistance and R_{Ω} is the ohmic resistance of the element.

To include the impedance mismatch, the antenna efficiency is sometimes expressed in the form $\eta_{total}=P_{rad} / (P_{rad}+P_{\Omega}+P_{match})$ where P_{rad} is the radiated power, P_{Ω} is the ohmic power loss in the element, and P_{match} is the power dissipated in the source resistor due to an impedance mismatch which is difficult to measure. It is more practical to define a mismatch efficiency as $\eta_{match}=1-|\Gamma|^2$, where Γ is the reflection coefficient at the antenna port. The efficiencies are multiplicative, in the usual way, i.e., $\eta_{total}= \eta_{rad} \times \eta_{match}$.

However, for an MEA, efficiencies of the elements are impacted by mutual coupling, the diversity combining, and the terminations of the elements. Mutual coupling causes power transfer from one element to other elements. This transferred power is then dissipated in different ways: in the terminating resistances; as ohmic losses in the elements; and as radiation from the elements. In practice, there is also ohmic loss and radiation from the MEA

support structure. In a simplified circuit model these powers can be included into the element's radiation and ohmic losses, respectively.

In terms of a matched load for the MEA, the conjugate match approach (the load impedance matrix of a receiving MEA is set to be the conjugate of the MEA impedance matrix), the mutual coupling is reduced because the mutual reactances are tuned out. However, the real parts cannot be tuned out of course, and so there would still be a mutual coupling loss caused by any mutual resistance.

In terms of the termination of the elements, diversity schemes can be categorized as simultaneous and non-simultaneous combining, and the MEA efficiency is formulated based on the analysis of the losses for both combining schemes in the transmitting and receiving case, respectively, as discussed in the following.

3.2.1 Simultaneous and non-simultaneous diversity combining schemes

Diversity combining can be implemented at either the transmitter or receiver, and it may act to change the terminations of the elements. One class of combining implementation has all the elements connected to fixed loads (*viz.*, the transmitters or receivers), and it is here called ***simultaneous combining*** because all the branch signals are used simultaneously. It includes Optimal Combining (OC), Maximum Ratio Combining (MRC), Equal Gain Combining (EGC), and Selection Combining (SC) implementations where all the elements have fixed terminations.

With simultaneous combining, power coupled from one MEA element to other elements can be “collected” at the receive loads in the receive case, or radiated by other elements in the transmit case. Such power must be considered “useful” - except in the receive case of SC with fixed terminations because we do not have access to the received power in the unselected terminations. For the case of the re-radiation, the power radiated via mutual coupling is part of the embedded element radiation pattern, and is therefore “useful”. Meanwhile, there is “wasted” power in the form of ohmic loss in all the elements.

Another class of combining implementation can be called ***non-simultaneous combining***, in which the signals are not combined simultaneously. It includes Switched Combining (SwC), and the implementation is to have only one element selected (i.e., terminated) at a time and the unused elements open circuited, and we will adhere to this form. With this non-simultaneous combining, we can simplistically model the situation as there being no mutual coupling since there is no current flowing through the open circuits. In some implementations, there may be physical non-zero currents because the physical terminations may be reactive, but the circuit model (with open circuits) is still valid because the elements are considered embedded.

3.2.2 Transmitting MEAs

Fig. 3.1 gives the circuit model of the *ith* embedded element of an *N*-element MEA, when only the *ith* element is transmit excited and all the other elements are present, not transmit excited, and terminated with their transmit source resistances. The dashed line represents the transmit port of the *ith*

embedded element. To the left hand side of the dashed line is the *ith* transmit source, and the right hand side is the embedded element, which includes the *ith* transmitting element in Fig. 3.1(a) and the other *N*-1 elements terminated and excited by mutual coupling. One of these terminated elements is depicted in Fig. 3.1(b).

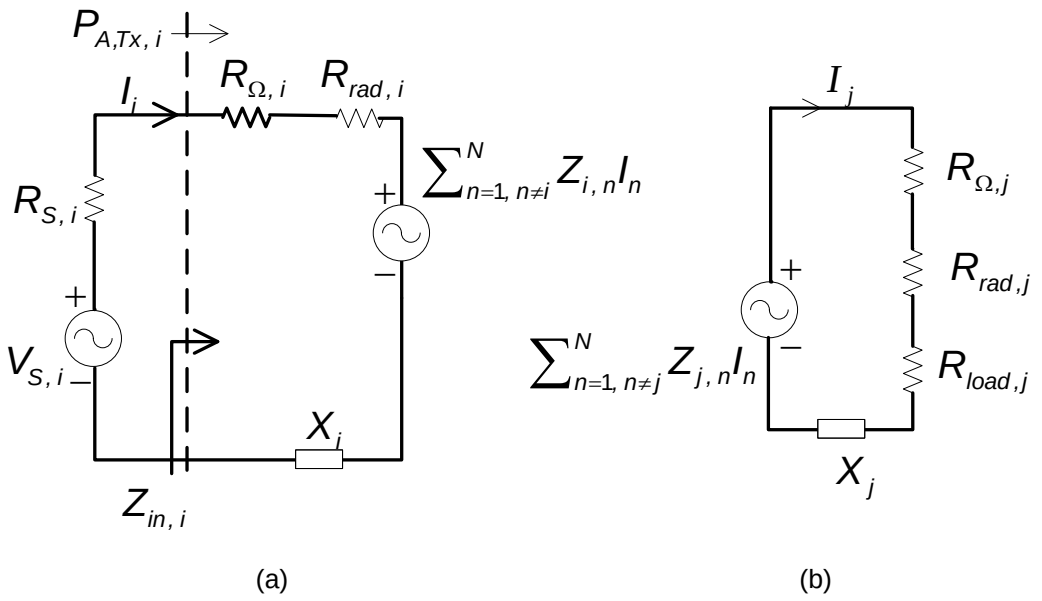

Figure 3.1 Circuit model of the *ith* embedded element of an *N*-element MEA

The *ith* element is transmitting and the other elements are present and terminated. The transmit source impedance is $R_{S,i}$, and the other elements are loaded with their transmitting source resistances, denoted R_{Load}. (a) is the *ith* transmitting element and (b) is one of the other terminated elements (taking the *jth* element as an example here). For simultaneous combining, there are *N*-1 similar circuits as (b). $P_{A,Tx,i}$ is the power accepted by the network to the right of the dashed line, from the *ith* transmitting element.

In Fig. 3.1(a), the *ith* element is excited with the transmit source $V_{S,i}$, which is the only external power source of the *ith* embedded MEA element considered. (Superposition can be used for considering all the elements transmitting together.) The source has impedance $R_{S,\,i}$, so any source reactance is omitted. The radiation resistance, $R_{rad,\,i}$, is associated with the radiation of the *ith* element in the presence of other elements. $R_{\Omega,\,i}$ and X_i are the associated ohmic loss and (self) reactance of this element, respectively. The current I_i causes power loss in the other elements if there is non-zero mutual coupling. The total power lost from the *ith* element to all the other elements through mutual coupling is from the sum of the voltage sources ($\sum_{n=1,\,n\neq i}^{N} Z_{i,\,n}\,I_n$) in the circuit model in Fig. 3.1(a).

In Fig. 3.1(b), each of the non-transmit-excited elements is excited by the mutual coupling. Taking the *jth* element as an example, the total mutual coupling excitation voltage on this element is $\sum_{n=1,\,n\neq j}^{N} Z_{j,\,n}\,I_n$. Some of this power is then radiated by this element in $R_{rad,\,j}$, and the rest dissipates as ohmic loss in $R_{\Omega,\,j}$ and $R_{load,\,j}$ (the transmit source resistance of the *jth* element).

It is emphasized that the currents I_i and I_j in Fig. 3.1 are the currents caused by the transmit excitation of the *ith* element only. For simultaneous combining, all the elements are excited by their own transmitters, so there are *N* similar circuits as Fig. 3.1 for the MEA, and the total current in each element is the sum of these circuit currents, by superposition. For non-simultaneous combining with open circuit terminations on the unselected elements, the currents in the unselected elements are zero, i.e., $I_{n=1,\ldots N,\,n\neq i}=0$, and so from the

simplistic circuit model viewpoint, all the radiation and losses induced by mutual coupling are zero. For non-simultaneous combining, the currents in the unselected elements are zero, i.e., $I_{n=1,\ldots N,\ n\neq i}=0$. So from the circuit model viewpoint, the unselected elements are open circuited. In a physical situation this may not happen, but the circuit model still includes the finite mutual coupling. This is because the selected element is treated as embedded, so that the mutual coupling with the unselected elements is included through the embedded element $R_{rad,i}$ and $R_{\Omega,i}$.

3.2.2.1 For simultaneous combining with all elements connected to fixed loads, e.g., transmitters:

For the *ith* embedded element, although only the *ith* element is transmit excited, the radiation is not only from this element but also from the other elements through mutual coupling.

The transmit efficiency of the *ith* embedded element for simultaneous combining (denoted $\eta_{Tx,i}$) is the ratio of the total power radiated from all the elements (this is denoted below as the sum of $P_{rad,n=1,\ \ldots,\ N}$) to the total power radiated and consumed by the MEA. This latter power is the power accepted by the network (to the right of the dashed line in Fig. 3.1) from the transmit source (to the left of the dashed line), denoted as $P_{A,Tx\,i} = \mathrm{Re}(V_{in,i}\, I^{*}_{i})$. So the ***embedded element transmit efficiency*** of the *ith* element is written as

$$\eta_{Tx,\,i} = \frac{\sum_{n=1}^{N} P_{rad,\,n}}{P_{A,TX,\,i}} \tag{3-1}$$

where

$$P_{A,Tx,i} = \sum_{n=1}^{N} P_{\Omega,n} + \sum_{n=1,\, n\neq i,}^{N} P_{load,n} + \sum_{n=1}^{N} P_{rad,n} \tag{3-2}$$

and

$\sum_{n=1}^{N} P_{rad,n} = \sum_{n=1}^{N} R_{rad,n} \left| I_n \right|^2$ is the total power radiated by all the elements from the excitation of i^{th} element (Fig.3.1);

$\sum_{n=1}^{N} P_{\Omega,n}$ is the ohmic loss in all the elements;

$\sum_{n=1,\, n\neq i,}^{N} P_{load,n} = \sum_{n=1,\, n\neq i,}^{N} R_{load,n} \left| I_n \right|^2$ is the loss in all the loads of non transmit excited elements.

When the situation reduces to a single element, the above transmit efficiency is the same as the classical single antenna radiation efficiency $\eta_{rad} = R_{rad} / (R_{rad}+R_{\Omega})$.

The ***total transmit efficiency of the embedded element*** at the *ith* transmit port includes the matching efficiency at the transmit port, $\eta_{match,i}$, as well as its embedded transmit efficiency, as

$$\eta_{Tx,total,i} = \eta_{match,i} \times \eta_{Tx,i} \tag{3-3}$$

where

$$\eta_{match,i} = 1 - \left| \Gamma_i \right|^2, \quad \Gamma_1 = (Z_{in,i} - R_{S,i}) / (Z_{in,1} + R_{S,i}) \tag{3-4}$$

and Γ_i is the reflection coefficient of the *ith* antenna element. The discussion of MEA reflection coefficient is in [120]. $Z_{in,i}$ to the excitation source resistance $R_{S,i}$.

3.2.2.2 For non-simultaneous combining with all unselected elements open circuited:

In this case, currents in the unselected elements are zero, so the radiations and losses induced on these elements by mutual coupling are zero. The *ith* embedded element transmit efficiency is then in the same form as the classical single antenna radiation efficiency:

$$\eta_{Tx,\,i} = \frac{P_{rad,\,i}}{P_{A,Tx,\,i}} \tag{3-5}$$

where

$$P_{A,Tx,\,i} = P_{\Omega,\,i} + P_{rad,\,i} \tag{3-6}$$

3.2.3 Receiving MEAs

In Fig. 3.2, the dashed line represents the receive port of the *ith* embedded element. The left hand side of the dashed line is the *ith* receiving embedded element, including the receiving element and the other elements, all terminated with loads. Again, there are *N*-1 similar circuits as Fig. 3.2(a) for the non-receiving elements, but only the *jth* element is shown here.

To the right hand side of the dashed line in Fig. 3.2(b), the voltage source, $V_{Rec,i}$, provides the received power on the receive port, and it is the only external

source to this embedded element circuit model. $P_{A,Rx,i}$ is the absorbed power (discussed in [121] and [122]) by the *ith* embedded element. This is the power accepted by the network to the left of the dashed line. The absorbed power includes the power dissipated in all the receiving loads (which is the wanted power); the power dissipated as the ohmic losses of all the elements (which is a "wasted" power); and the power radiated by all the non-receiving elements (which is excited by mutual coupling and considered as "wasted" power).

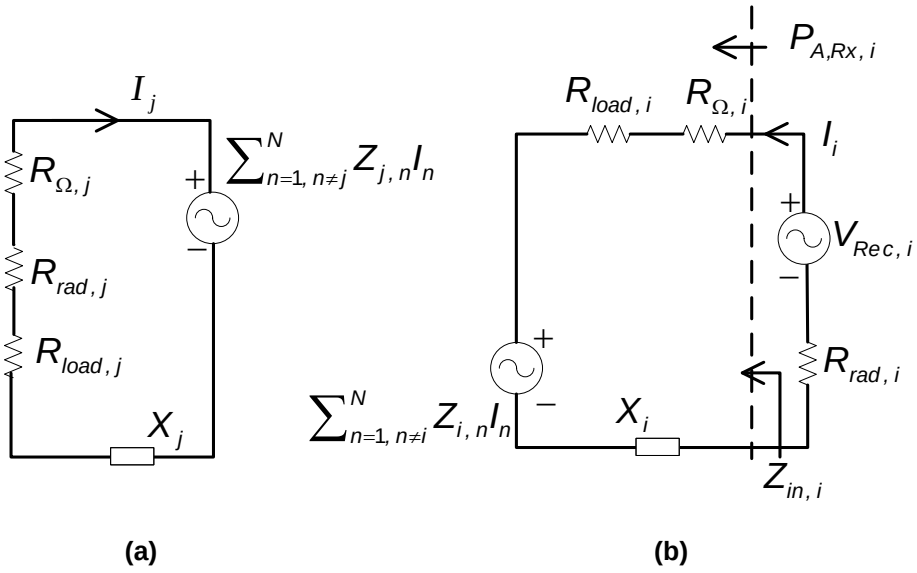

Figure 3.2 Circuit model of *ith* embedded element of the *N*-element MEA

The *ith* element is receiving and the other elements are present and terminated. (a) is one of the terminated elements (taking the *jth* element as an example here). For simultaneous combining, there are *N*-1 similar circuits as (a). (b) is the *ith* receiving element. $P_{A,Rx,i}$ is the power absorbed by the network (to the left of the dashed line) from the receiving port (the dashed line).

$R_{rad,i}$ is the (re-)radiation resistance of the *ith* element. This re-radiation is caused by the reflection at the receive port of the *ith* embedded element (the dashed line in Fig. 3.2), and so does not occur unless $R_{rad,i}$ mismatches with $Z_{in,i}$.

This re-radiation is different to the *structural* (or *residual*) scattering of the antenna [121][122], and it is zero when the antenna is lossless and matched. Since this mismatch causes an additional power loss, the mismatch changes the total receive efficiency. It is further discussed below.

3.2.3.1 For simultaneous combining with all elements connected to fixed loads, e.g., receivers:

The *ith* ***embedded element receive efficiency*** ($\eta_{Rx,\,i}$) is defined here as the ratio of the power delivered to the loads of all the elements (the wanted power) to the absorbed power of the MEA owing to the reception of the *ith* element, as

$$\eta_{Rx,\,i} = \frac{\sum_{n=1}^{N} P_{load,\,n}}{P_{A,\,Rx,\,i}} \tag{3-7}$$

where

$$P_{A,\,Rx,\,i} = \sum_{n=1}^{N} P_{\Omega,\,n} + \sum_{n=1,\,n\neq i}^{N} P_{rad,\,n} + \sum_{n=1}^{N} P_{load,\,n} \tag{3-8}$$

and $P_{A,Rx,i}$ is the absorbed power at the embedded element and the radiated power from all the non-receiving elements excited by the mutual coupling, $\sum_{n=1,\,n\neq i}^{N} P_{rad,\,n}$. The re-radiation of the *ith* element, $P_{rad,i} = R_{rad,i}\,|I_i\,|^2$, is the total

received power minus the absorbed power $P_{A,Rx,i}$, as indicated in Fig. 3.2(b), so it is not part of $P_{A,Rx,i}$. It changes the total receive efficiency of the embedded element and is further discussed below.

Note that Eqs. (3-7) and (3-8) are similar to Eqs. (3-1) and (3-2), except that $P_{rad,n}$ and $P_{load,n}$ are interchanged, so the receiving case and the transmitting case are well-related. As seen by one transmit element, the radiation from the other elements (excited by mutual coupling) is the reciprocal analogy of the power received by the loads of the other elements (excited by mutual coupling) in the receive case. With the interchange of $P_{rad,n}$ and $P_{load,n}$, reciprocity can be applied, and the embedded element receive efficiency can be found from the embedded element transmit efficiency for the same MEA element with the same combining implementation, i.e., $\eta_{Rx,rad,i} = \eta_{Tx,rad,i}$.

However, for a single receiving element (rather than a receive MEA), Eq. (3.7) reduces to $\eta_{Rx} = R_{load} / (R_{load}+R_{\Omega})$. This is not the classical radiation efficiency. In fact it is not an antenna parameter, because in the receive case the metric is how much power is delivered to the load rather than to radiation.

The *total receive efficiency of the embedded element* at the *ith* receive port ($\eta_{Rx,total,i}$) can be analogously found from Eqs. (3-3) and (3-4), where $R_{rad,i}$ is used to replace $R_{S,i}$ as

$$\eta_{Rx,\,total,\,i} = \eta_{match,\,i} \times \eta_{Rx,\,i} \tag{3-9}$$

where, as above,

$$\eta_{match,\,i} = 1 - \left|\Gamma_i\right|^2, \quad \Gamma_i = (Z_{in,\,i} - R_{rad,\,i})/(Z_{in,\,1} + R_{rad,\,i}) \tag{3-10}$$

in which the source reactance is taken as zero. With reciprocity, again $\eta_{Rx,total,i} = \eta_{Tx,total,i}$.

3.2.3.2 For non-simultaneous combining with all unselected elements open circuited:

Similar to the non-simultaneous transmit case, since the unselected elements are open circuited, the power lost on these elements are zero (in a simplistic circuit model). The embedded element receive efficiency is therefore in the same form as that for single element antenna and the reciprocity can be again applied:

$$\eta_{Rx,\,i} = \frac{P_{load,\,i}}{P_{A,Rx,\,i}} \tag{3-11}$$

where

$$P_{A,Rx,\,i} = P_{\Omega,\,i} + P_{load,\,i} \tag{3-12}$$

In the above formulas, $\eta_{TX,i}$ and $\eta_{RX,i}$ measure how much wanted power is radiated/received per unit accepted/absorbed power by the embedded element. On the other hand, these also indicate how much power is wasted through mutual coupling in the forms of ohmic loss and re-radiation. It is impractical to measure $\eta_{TX,i}$ and $\eta_{RX,i}$ with their definitions in Eq. (3-1)(3-2) and (3-7)(3-8). Instead, with Eq. (3-3), (3-4), (3-9) and (3-10), they can be found from the embedded element total efficiency and matching efficiency, both of which can be

measured with single port systems. In the next section, an example MEA is measured to demonstrate this process. The results verify the impact of the diversity scheme on the power radiated and lost in the embedded elements.

3.2.4 MEA total efficiency matrix

As noted above, the total efficiency for each embedded element can be different. A diagonal matrix is used to include all the total efficiencies of embedded element of an MEA as

$$\boldsymbol{\eta}_{total} = \begin{bmatrix} \eta_{total,1} & 0 & \cdots & 0 \\ 0 & \eta_{total,2} & \cdots & 0 \\ \vdots & \vdots & \vdots & \vdots \\ 0 & 0 & \cdots & \eta_{total,M} \end{bmatrix} \tag{3-13}$$

and this is here referred to as the *MEA total efficiency*. Here, M is the number of the antenna elements.

In this section, the MEA efficiencies are formulated and applied to the analysis of how the radiated/received power and losses are impacted by return loss, mutual coupling, diversity combining scheme and the associated terminations of the MEA. In the following sections, the impact of the MEA total efficiency on the diversity and capacity performances is presented.

3.3 Impact of MEA total efficiency on diversity gain

The diversity performance of an MEA is measured by its diversity gain, G_{div}, which has several definitions as introduced in Section 2.2.6. The approach of Eq. (2-13) to Eq. (2-18) includes the impact of the antenna correlation

coefficient, but it corresponds to a lossless MEA with MRC. When the antenna is lossy, this approach needs to be revised.

3.3.1 Formulations of the impact of η_{total} on the diversity gain

Taking receive diversity as an example, loss in the embedded MEA elements reduces the receive *SNR* of each receive branch. The impact of this reduced *SNR* on G_{div} can be included by scaling down the correlation coefficients to have effective values, as

$$\boldsymbol{\rho}_{scale} = \sqrt{\boldsymbol{\eta}_{total}} \cdot \boldsymbol{\rho} \cdot \sqrt{\boldsymbol{\eta}_{total}}$$
$$= \begin{bmatrix} \eta_{total,1} & \rho_{1,2}\sqrt{\eta_{total,1}\eta_{total,2}} & \cdots & \rho_{1,M}\sqrt{\eta_{total,1}\eta_{total,M}} \\ \rho_{2,1}\sqrt{\eta_{total,2}\eta_{total,1}} & \eta_{total,2} & \cdots & \rho_{2,M}\sqrt{\eta_{total,2}\eta_{total,M}} \\ \vdots & \vdots & \vdots & \vdots \\ \rho_{M,1}\sqrt{\eta_{total,M}\eta_{total,1}} & \rho_{M,2}\sqrt{\eta_{total,M}\eta_{total,2}} & \cdots & \eta_{total,M} \end{bmatrix} \quad (3\text{-}14)$$

and now

$$\boldsymbol{\Lambda}_{scale} = [\lambda_{scale,1}\ \lambda_{scale,2} \cdots\ \lambda_{scale,M}]^T = SVD(\boldsymbol{\rho}_{scale}) \quad (3\text{-}15)$$

Eq. (3-14) defines a scaled correlation coefficient matrix, $\boldsymbol{\rho}_{scale}$, which is $\boldsymbol{\rho}$ weighted by the (positive) square root of $\boldsymbol{\eta}_{total}$ from both sides. It is important to note that $\boldsymbol{\rho}_{scale}$ represents the reduced *SNR* on each receive branch, rather than a reduced correlation. Note also that the diagonal of $\boldsymbol{\rho}_{scale}$ is not unity because of the scaling. Likewise, the scaled singular value column matrix, $\boldsymbol{\Lambda}_{scale}$, contains the impact of the embedded element total efficiencies on the equivalent lossless and uncorrelated branches of the MEA. With Eqs. (3-13)-(3-15) and (2-17), the *CDF* of the MRC *SNR* with the impact of MEA total efficiency can be found as

$$CDF(\gamma \le \gamma_c) = \sum_{k=1}^{M} \frac{1}{\prod_{\substack{m=1 \\ m \ne k}}^{M} (1 - \frac{\lambda_{scale,m}}{\lambda_{scale,k}})} (1 - e^{-(\gamma_c / \Gamma)/\lambda_{scale,k}}) \tag{3-16}$$

for $k=m$, $\lambda_{scale,m} \neq \lambda_{scale,k}$

Other combination techniques can follow the same method, should this be required. For example, the *CDF* of Selection Combining (SC) in a Rayleigh environment is

$$CDF(\gamma \le \gamma_c) = \prod_{k=1}^{M} (1 - e^{-(\gamma_c / \Gamma)\lambda_{scale,k}}) \tag{3-17}$$

3.3.2 CDF of a dipole MEA with SC

To demonstrate and verify the above formulas including the impact of MEA efficiency on G_{div}, the *CDF* of a 2-element orthogonal half wavelength lossy dipole MEA with SC was computed with Eqs. (3-13)-(3-15),(3-17) and compared with a published measurement result in [104]. The total efficiencies of the embedded elements are 0.51 and 0.59, respectively. The elements are uncorrelated, as suggested in [104], so the correlation matrix is a 2x2 identity matrix.

In Fig. 3.3(a) the solid curves are the SC *CDF*s of idealized MEAs (uncorrelated and lossless) having 1 to 2 antenna branches from the left to the right. The dashed curve is the computed SC *CDF* of the 2-element orthogonal

half wavelength lossy dipole MEA, which agrees very well with the measured result in Fig. 3.3(b) from [104]. The possible sources of the difference are the measurement uncertainties of the efficiency and the finite correlation of an implemented antenna.

(a)

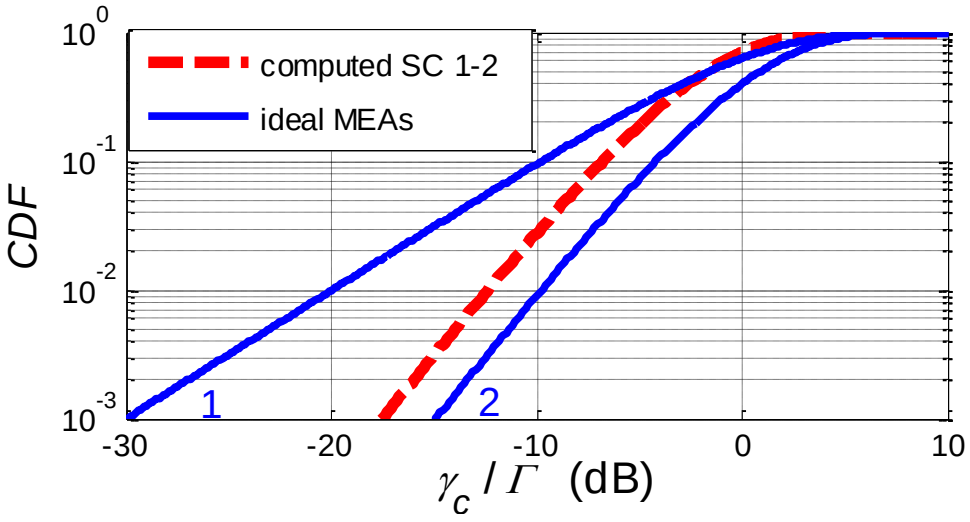

(b)

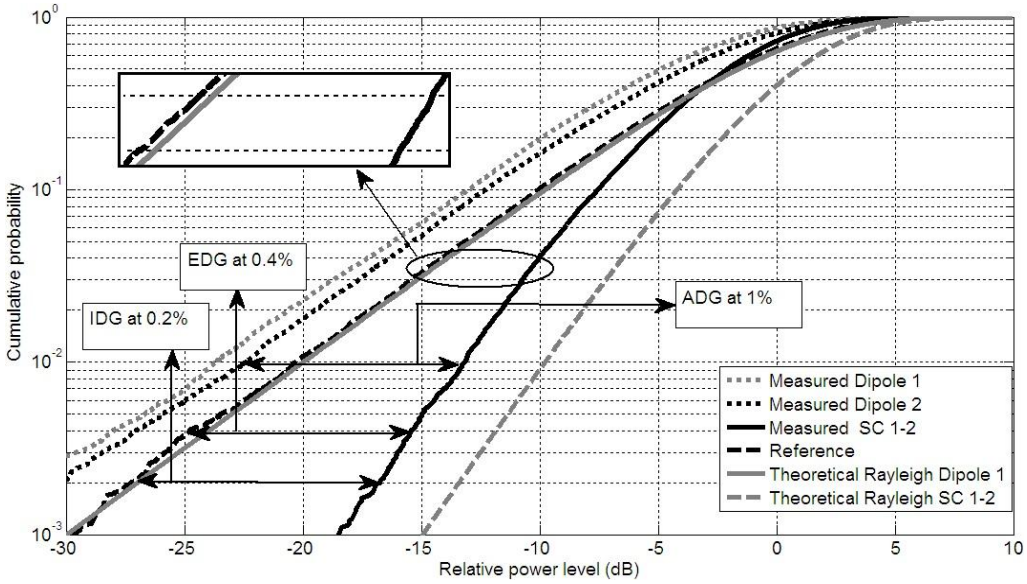

Figure 3.3 *CDF* against *SNR* of a 2-element dipole MEA

(a) computed and (b) measured *CDF* of a 2-element orthogonal half wavelength lossy dipole MEA with Selection Combining. Plot (b) is from [104].

3.3.3 CDF of element-symmetric and -asymmetric MEA

There is a special class of MEA structures which are symmetric in the sense that each element sees an identical structure of elements around it. The analysis of these structures becomes simplified because if all the terminating impedances are the same, then all the elements will see the same impedance on transmit, and will invoke the same total radiation and losses, and the same efficiencies. So an averaged efficiency can be used, and ρ_{scale} and Λ_{scale} can be simplified as:

$$\eta_{total,1} = \eta_{total,2} = \ldots = \eta_{total,M} = \eta_{total} \tag{3-18}$$

$$\rho_{scale} = \eta_{total}\ \rho$$

$$\Lambda_{scale} = \eta_{total}\Lambda$$

Conversely, for a general MEA, there is asymmetry in the sense that the elements will have different losses and efficiencies. It is of interest to compare the difference in diversity performance of the element symmetric and asymmetric MEA.

Fig. 3-4 gives the computed SC *CDF* curves of 3-element symmetric MEAs in Fig. 3-4(a) and the curves of the same MEAs but with asymmetric element efficiencies in Fig. 3-4(b). Each MEA comprises three uncorrelated half wavelength dipole elements with the element efficiency as suggested in the figures. To verify the impact of correlation on element asymmetric MEAs, the *CDF*s of correlated MEAs are also computed in Fig. 3-4(c) and (d).

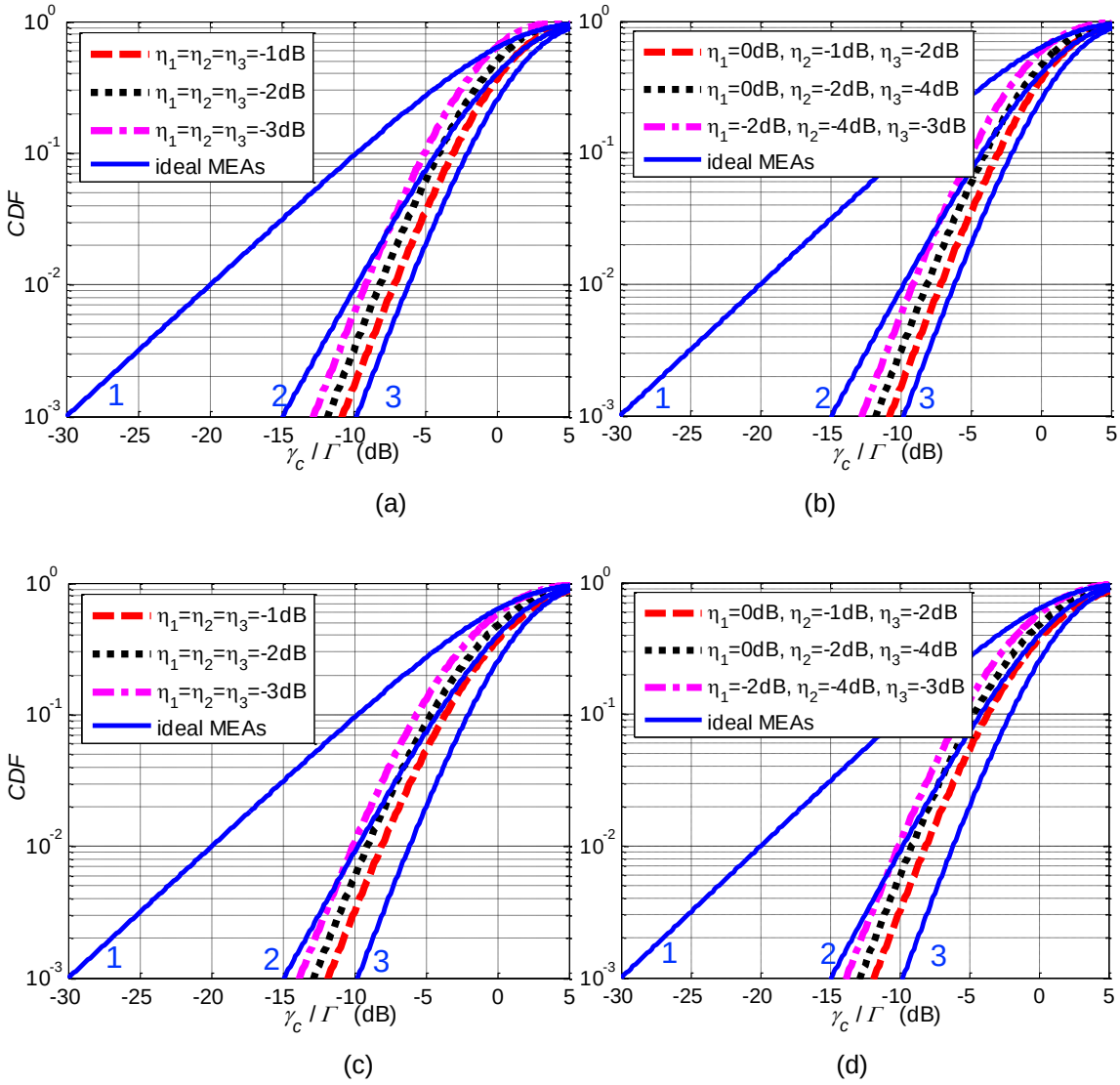

Figure 3.4 Selection combining *CDF*s of 3-element MEAs

(a) uncorrelated, symmetric (b) uncorrelated, asymmetric (c) correlated, symmetric and (d) correlated, asymmetric 3-element half wavelength dipole MEAs

In Fig. 3.4(a), with the decrease of the element efficiency, the *CDF* curve translates to the left of the figure towards the lower *SNR* direction, so G_{div} decreases. The spacing between any two adjacent dashed curves is 1dB, which corresponds to the difference of the element efficiencies. The computed *CDF*

curve for the MEA with element efficiency of -2dB agrees well with the published measured result of the same MEA in [104], and the agreement helps to verify the proposed formulations from measurements.

In Fig. 3.4(b), the averaged (in decibel) efficiency of each asymmetric MEA is -1dB, -2dB, and -3dB, respectively, and equals to the element efficiency of the symmetric MEAs in Fig. 3.4(a). It is obvious that the *CDF* curves of the corresponding symmetric and asymmetric MEAs are the same. This observation in turn shows that it is reasonable to use averaged in decibel [104] (rather than the highest [118]) element efficiency for the MEA G_{div} in a simple way.

Fig. 3.4(c) and (d) are for the same symmetric and asymmetric MEAs but the elements are correlated. A correlation matrix

$$\rho = \begin{bmatrix} 1 & 0.7 & 0.1 \\ 0.7 & 1 & 0.3 \\ 0.1 & 0.3 & 1 \end{bmatrix}$$

is used as an example. The computed results shows that, although the correlation changes the slope of the *CDF* curves, the spacing between the adjacent curves is again 1dB, and the averaged (in decibel) efficiency can still be used to find the asymmetric MEA diversity performance in a simple way. The last observation suggests that the requirement of having uncorrelated elements for using (dB-) averaged element efficiency in [104] does not seem to be necessary.

3.3.4 G_{div} reduction of MEA due to the impact of η_{total}

To demonstrate how the MEA total efficiency impact G_{div}, the *CDF* curves of lossless and lossy element-symetric MEAs with MRC are plotted in Fig. 3.5 for

comparison. The solid thin-line curves are for idealized MEAs (element-symmetric, uncorrelated and lossless) having 1 to 12 antenna elements from the left to the right. The thick-line curves are for an element-symmetric and uncorrelated 12-element MEA with η_{total}=0.1, 0.3, 0.5, 0.7 and 0.9 from the left to the right. Here, the symmetry refers to element symmetry: each element sees an identical MEA structure, so the total efficiency of each embedded element of the MEA is identical. The elements of the MEAs are uncorrelated, so the impact of antenna correlation coefficient on the diversity gain is excluded.

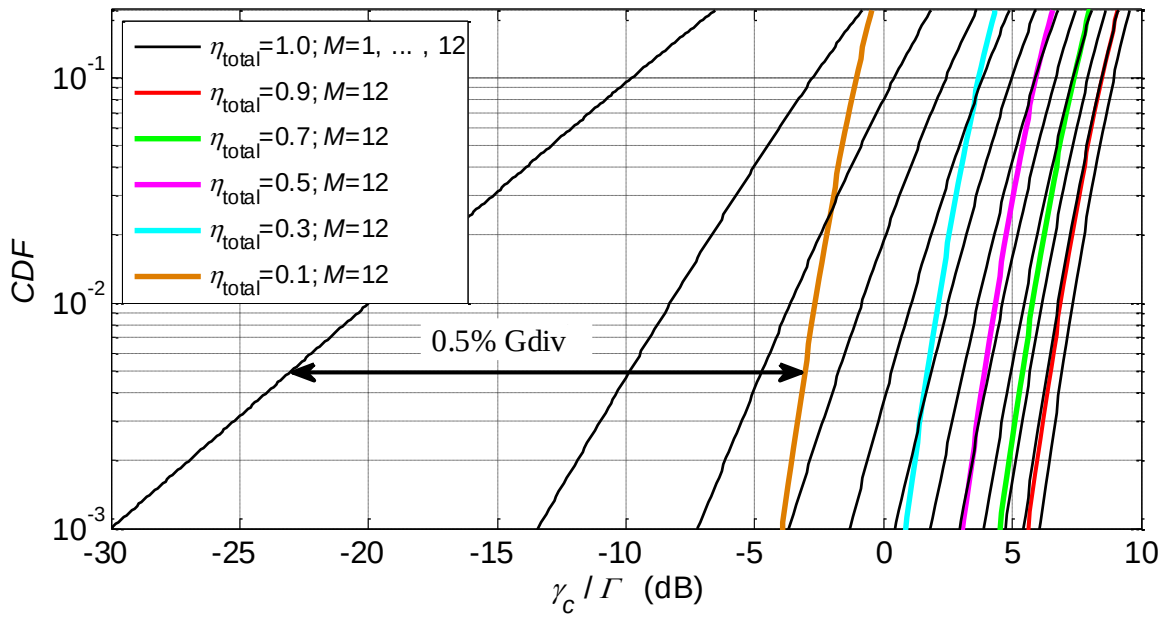

Figure 3.5 *CDF* of idealized MEAs and lossy 12-element MEAs

Taking the leftmost thin-line curve for 1 element idealized antenna as the reference, G_{div} is the *SNR* difference between the MEA and the reference at a

given probability. For example, at the probability of 0.5%, the MRC diversity gain of the 12-element MEA with η_{total}=0.1 is G_{div}=20dB, as illustrated in Fig. 3.5.

For the 12-element lossy MEA, its diversity gain is reduced and equals to that of an idealized MEA with lower number of elements, then we can define the diversity order of the lossy MEA with its equivalent idealized MEA. For example, for the probability of 0.5%, the 12-element MEA with η_{total}=0.7 has the same G_{div} as the idealized MEA with the number of elements of 10.6, so its diversity order is defined as 10.6. Likewise, the MEA with η_{total}=0.5 has a diversity order of 7.8, and with η_{total}=0.1 the MEA only has a diversity order of 3.5. For the case when η_{total}=0, Eqs. (3-14)-(3-16) are unsuitable for both the *CDF* and the diversity gain. The thick-line curves are all parallel to the rightmost thin-line curve. As mentioned above, this rightmost thin-line curve is for an idealized 12-element MEA. With the decrease of η_{total}, the *CDF* curve of the 12-element MEA moves to the left, so G_{div} decreases, while the slope of the *CDF* curve is retained for the given number of elements.

Also in Fig. 3.5, the spacing between each adjacent thick-line curves is different. Such spacing corresponds to an efficiency decrease step of 0.2. When the efficiency is low, the spacing is larger. So G_{div} drops at different rates with η_{total}. The lower the MEA efficiency, the faster the reduction in diversity gain. This observation is supported with the plot of G_{div} against efficiency in Fig. 3.6.

In Fig. 3.6, the MRC G_{div} at the probability of 0.5% over the MEA total efficiency is given for the number of elements M=2 to M=12. As in the examples

used above, these MEAs are element-symmetric and uncorrelated. With the decrease of MEA efficiency, the slopes of the G_{div} curves increase, so G_{div} drops faster when the efficiency is lower, as noted above.

For a given efficiency in Fig. 3.6, all the curves have the same slope, so it indicates that, for MEAs with different number of elements, G_{div} decreases with efficiency in the same rate. This is also true for diversity gains at other probabilities. For example, when the MEA total efficiency reduces by 3dB, the diversity gain also reduces by 3dB for MEAs with any number of elements at any probability. Thus it is an interesting conclusion that the diversity gain decreases with efficiency independently of the probability and the number of uncorrelated elements.

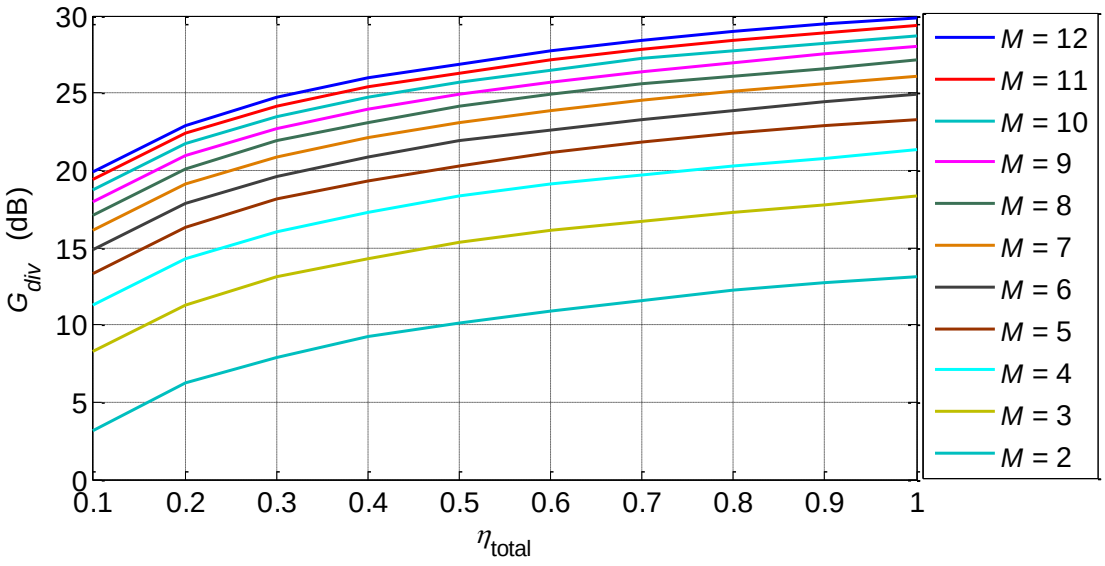

Figure 3.6 Diversity gain in dB over MEA total efficiency

3.4 Impact of MEA total efficiency on capacity

The instantaneous MIMO channel capacity for a static unknown channel is given in Eq. (1-1) and repeated here:

$$C_{ins} = \log_2 \det[\, \mathrm{I} + \frac{SNR}{n_T} \mathbf{H}_{\mathbf{ins}} \mathbf{H}_{\mathbf{ins}}^{\mathrm{H}} \,] \tag{3-19}$$

where **I** is an identity matrix; n_T is the number of the transmit elements; and $\mathbf{H}_{\mathbf{ins}}$ is a normalized instantaneous channel transfer matrix. The mean capacity is averaged over the channel variations, written $C_{avg}=\mathrm{E}_{\mathrm{H}}\{C_{ins}\}$. Note that this is different to the capacity of the mean channel. The mean capacity is known to be close to the upper limit given by the parallel (eigen) channel formulation for known channels [12].

The Kronecker model [86] introduced in Chapter 2 is a simplistic method to combine the transmit and receive antenna correlation coefficient into the channel transfer matrix. As noted above, the accuracy of this approach has been questioned in [102], and [103] reports a revised version for polarization diversity. But in the same spirit as using the capacity, the Kronecker model is a convenient step for comparatively evaluating MEAs.

With this model, the channel can be taken as zero mean, unit variance, complex Gaussian i.i.d., and the instantaneous white channel matrix is denoted $\mathbf{H}_{\mathbf{w,ins}}$. It is modified with the correlation coefficient matrices of the transmit and receive antennas, as

$$\mathbf{H}_{\mathbf{ins}} = \rho_{Rx}^{1/2}\ \mathbf{H}_{\mathbf{w,ins}}\ \rho_{Tx}^{1/2} \tag{3-20}$$

where ρ_{Rx} and ρ_{Tx} are the correlation coefficient matrix of the transit and receive MEA, respectively, in a given propagation channel model. For samples of the instantaneous channel over different propagation environments, new correlation matrices would arise. But for samples of the instantaneous channels in a specific propagation environment, the correlation matrices remain the same. The transmit correlation coefficient matrix is taken to be the same as its well-defined receive operation.

To include the impact of receive and transmit MEA total efficiencies on the MIMO capacity, the scaled correlation coefficient matrices defined in Eq. (3-14) are used in the same way,

$$\mathbf{H}_{\mathrm{scale},\mathbf{ins}} = \rho_{\mathrm{scale},Rx}^{1/2}\ \mathbf{H}_{\mathbf{w,ins}}\ \rho_{\mathrm{scale},Tx}^{1/2} \tag{3-21}$$

If the transmit and receive antennas have element symmetric structures and have the same total element efficiency for all their elements, respectively, then Eq. (3-21) is simplified to

$$\mathbf{H}_{\mathrm{scale},\mathbf{ins}} = \sqrt{\eta_{Rx,\,total}}\,\rho_{Rx}^{1/2}\ \mathbf{H}_{\mathbf{w,ins}}\ \rho_{Tx}^{1/2}\sqrt{\eta_{Tx,\,total}} \tag{3-22}$$

If an idealized transmit MEA (unity total efficiency for each element and zero correlation) is used, the impact of the imperfect receive antenna can be singled out. Here, the receive MEA efficiency scales the channel matrix to $\mathbf{H}_{\mathbf{scale,ins}}$ as

$$\mathbf{H}_{\text{scale,ins}} = \rho_{\text{scale,Rx}}^{1/2}\ \mathbf{H}_{\text{w,ins}} \tag{3-23}$$

Or alternatively stated, *SNR* is scaled, and the resulting capacity, $C_{scale,ins}$, is

$$C_{scale,ins} = \log_2 \det[\ \mathrm{I} + \frac{SNR}{n_T} \rho_{\text{scale,Rx}}^{1/2} \mathbf{H}_{\text{w,ins}} \mathbf{H}_{\text{w,ins}}^{\mathrm{H}} \rho_{\text{scale,Rx}}^{1/2}] \tag{3-24}$$

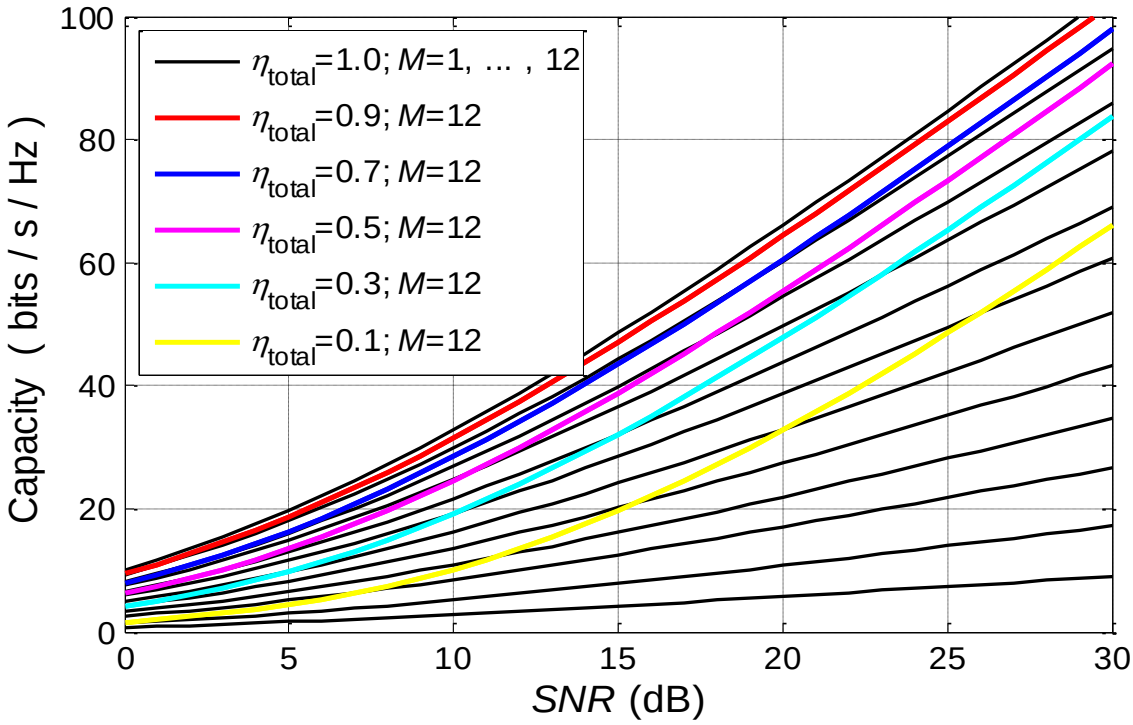

Figure 3.7 Capacities of idealized and lossy MEAs in Rayleigh channels

The thin-line curves are for the MIMO links with idealized MEAs at both ends of links. The thick-line curves are for when an idealized 12-element MEA is at one end, and an uncorrelated MEA with various efficiencies is at the other end.

Fig. 3.7 illustrates the impact of MEA total efficiency on the averaged capacity. The thin-line curves are the averaged capacities achieved in Rayleigh channels with the same idealized (lossless and uncorrelated) MEAs at both end

of the MIMO link. The numbers of elements are from 1 to 12 from the bottom to the top in the figure. The thick-line curves are for when an idealized 12-element MEA is at one end of the MMO link, and an uncorrelated 12-element MEA with various efficiencies at the other link, all in a Rayleigh channel. Statistical channel information is contained in the correlation coefficient matrix in Eq. (3-23) so the capacity for other propagation scenario models can also be found.

With Fig. 3.7, the capacity order of a lossy MEA at a given *SNR* can be found from the equivalent idealized MEA. For example, for *SNR*=20dB, the 12-element MEA with η_{total}=0.7 has the same capacity as an idealized MEA with 11 elements, so its capacity order is 11 at *SNR*=20dB. Likewise, the MEA with η_{total}=0.1 has capacity order of 6 at the same *SNR*. It is important to mention that the capacity order of an MEA is not necessary the same as its diversity order, since they are defined differently.

Similar to the change of diversity gain, the capacity decreases faster when the MEA efficiency is lower. This phenomenon is also seen in Fig. 3.8, in which the signed reduction of capacity in Rayleigh channels is plotted against the total efficiency of the receive MEA with different numbers of elements, *M*, for *SNR*=20dB. Here, the transmit MEA is idealized and has the same *M* as the receive MEA. The zero efficiency imposes a zero capacity.

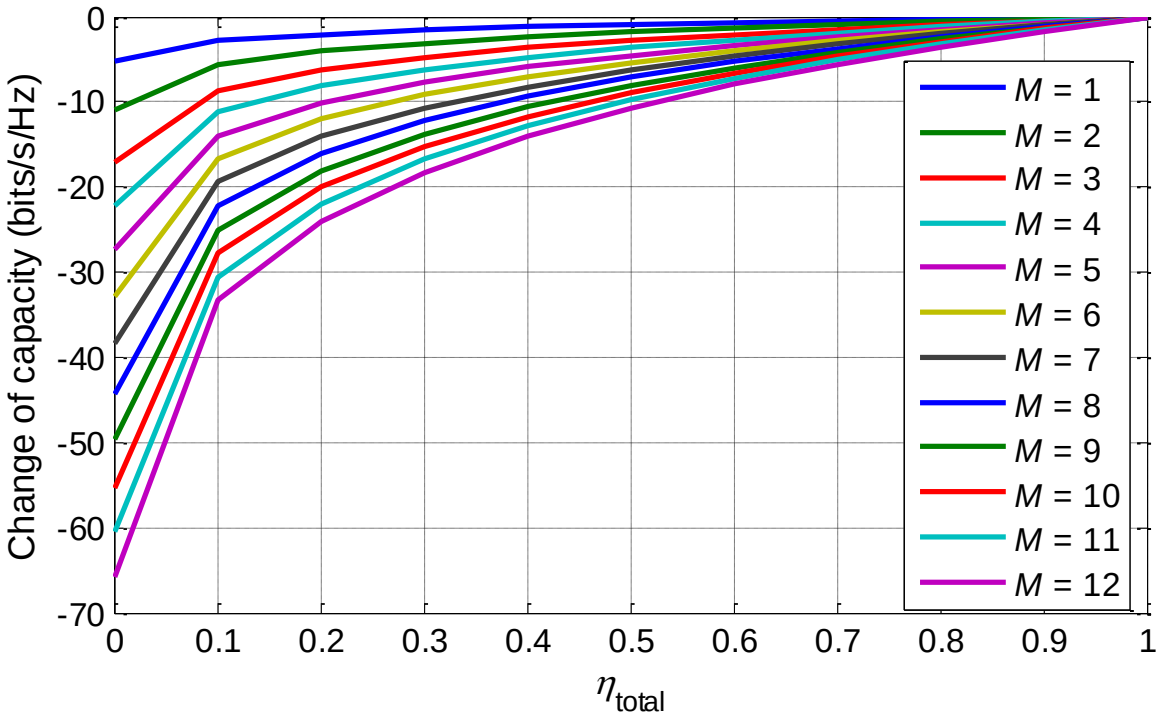

Figure 3.8 Change of capacity against MEA η_{total} with the number of elements.

At a given efficiency, the curve of capacity reduction has different slope for each *M* in Fig. 3.8, so the capacity decrease rate depends on *M*. When *M* is lower, the slope of capacity reduction is smaller, so the capacity is less sensitive to the change of MEA efficiency. In other words, the capacity of a large MEA is more affected by its efficiency than a small MEA. This observation is different to the equal rate of diversity decrease against the efficiency of MEA with various *M* in Fig. 3.6. The relative capacity change with respect to efficiency is not dependent on the number of antennas, *M*, as depicted in Fig. 3.9.

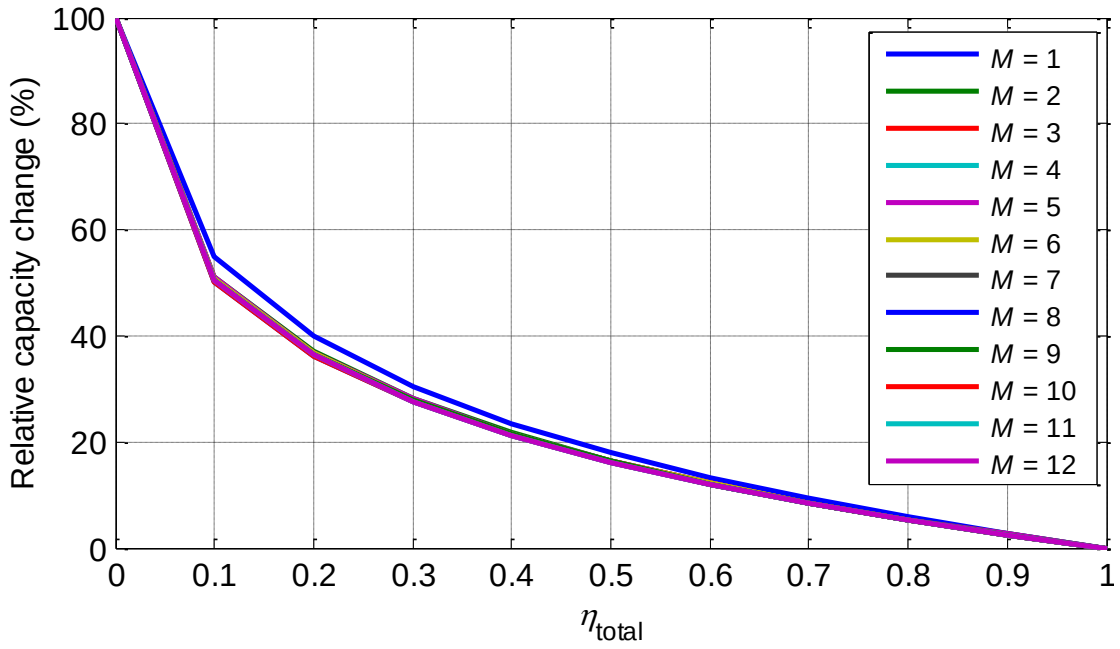

Figure 3.9 Relative capacity change against η_{total} with the number of elements.

3.5 Conclusion

In this chapter, formulations for the efficiencies of an MEA with diversity combining are developed in the context of MIMO communications performance. The MEA *embedded element efficiency* is derived for both the transmit and the receive cases, so that the principle of reciprocity can be simply interpreted for MEAs. The *total efficiency of the embedded element* is also presented. The *MEA total efficiency* is expressed as a diagonal matrix of the total efficiencies of the embedded element.

This matrix form of MEA total efficiency is then used to calculate the impact of MEA total efficiency on the communications performance in terms of the diversity gain and capacity in modelled propagation scenarios. When the MEA has an element-symmetric structure (all elements see the same antenna structure) then all the embedded element efficiencies are the same, and the formulations simplify and align with a known result. The reductions in the diversity gain and capacity, resulting from the total loss (ohmic and through mutual coupling) are demonstrated with uncorrelated MEAs.

The diversity order and MIMO capacity order of an MEA are expressed as an equivalent number of idealized elements, i.e., lossless, equal gain, uncorrelated and uncoupled, at a given probability, e.g., 0.5%. This metric allows a performance comparison of different MEA designs.

CHAPTER 4: SPACE EFFICIENCY OF MEAS

MEAs support MIMO communications and other antenna diversity techniques, resulting in better communications performance than available from single antenna systems. The space occupied by MEAs becomes important when the antennas are integrated into small or portable devices, and a metric is required for comparing different MEA designs and configurations. Single element antennas have standard procedures to support their performance evaluation, and classical compactness measures such as the size of the inscribing sphere associated with the Chu and McLean limits. In this chapter, a figure of merit for the space efficiency is developed for evaluating the MEA compactness with respect to the MEA bandwidth and the potential communications performance. The impact of element efficiencies, mutual coupling, correlation, diversity scheme, and propagation scenario are included, allowing a spherical volumetric comparison of different MEAs in different propagation scenarios. The measures are demonstrated with several examples.

4.1 Introduction

There is a need for compact MEAs for boosting communications performance. In practice, MEA designs for MIMO are often developed in a rather ad hoc way. Some statistical parameters, such as correlation, distributed

directivity, mean effective gain (MEG), capacity efficiency and diversity gain, etc., are used to measure the MEA performance in a given statistical propagation scenario, as discussed in Chapter 2. But these figures of merit do not address how compact the antenna is. For example, an array with very widely spaced elements will work well for most MIMO systems, but may be physically unsuitable because it is too expansive. On the other hand, if the elements are tightly spaced for a small volume, the MEA may not deliver the sought communications performance owing to high correlations and mutual coupling losses. Many MIMO antennas have been presented in the literature whose performance is discussed but without reference to the volume, or space efficiency.

For single port antennas, there are standard test procedures [27] and definitions of terms [1] for performance parameters. To evaluate compactness, the trade-off between volume (as measured by the electrical size of the inscribing sphere) and the bandwidth can be used. The Chu-MacLean [14][81] limits for lossless elements give a benchmark. However, MEAs are of course more complicated than single elements, and there is no standard for the evaluation of the MEA compactness, nor well developed trade-offs between the MEA volume and its performance, although [14] gives an idealized modal approach. We are interested in how electrically small a practical MEA could be for a required performance. A step in this direction is to develop a compactness measure for MEAs.

In this chapter, a space efficiency is proposed as a useful tool to comparatively evaluate the compactness of an MEA in the context of its

bandwidth (proportional to capacity) and its narrowband MIMO communications performance (governed by the correlation and losses). In the literature, the term space efficiency is sometimes used, e.g. in [123]-[127], but without a clear definition. In this chapter, its definition is developed for MEAs.

Two concepts are used for the MEA space efficiency here: an equivalent number of idealized elements, and an MEA radiation quality factor, which gives the radiation impedance relative bandwidth of the MEA. An MEA performance metric is used to define an equivalent number of idealized elements. This metric is the diversity gain or another convenient form such as the information-theoretic capacity efficiency for MIMO. We note here that an information-theoretic capacity does not sit well with practical communications considerations such as non-Gaussian signals, finite block lengths, protocols including multi-user access and other bandwidth sharing technologies, inaccurate models, imperfect signal processing, etc. These, along with the antenna performance, tend to dominate the achievable communications performance, but nevertheless an information theoretic metric offers a limit to which all systems can benchmark. These types of communications statistical metrics also depend, through the antenna, on the propagation detail, but can be considered fixed within a statistically fixed propagation scenario. Two antenna examples, including a realistic slot cube MEA [128]-[130] and an idealized dipole cube MEA [49], are used to illustrate the discussion. More familiar examples – classical, idealized dipole arrays – are also included for some theoretical performance benchmarking.

This rest of the chapter is organized as follows: Section 4.2 defines the equivalent number of idealized elements for a given MEA in a certain scenario. Section 4.3 takes the physical volume of the MEA and divides it by the equivalent number of idealized elements to define an effective element volume for the MEA. Section 4.4 discusses the efficiencies of the MEA, which are used in Section 4.5 to derive the radiation quality factor of the MEA. The results are combined in the Chu-McLean diagram with some MEA examples in Section 4.6, and the space efficiency is presented in Section 4.7, followed by a summary in Section 4.8.

4.2 Equivalent Number of Idealized Elements for MEA

As an MEA becomes more compact, there is a tendency for the mutual coupling to increase, resulting in extra losses in the element loads, which in turn decreases the MEA efficiency. MEA efficiencies are discussed in Section 4.5, in Chapter 3, as well as in [130]. Moreover, any associated circuitry such as analogue beamformers, feed structures, or matching circuits, etc., can also become more lossy (owing to higher current consumption) or degrade performance in some other way as they become more compact. The increase of mutual coupling and correlation between antenna elements, as well as the lower antenna efficiency, all act to degrade the MEA diversity performance and the associated capacity.

A diversity order (defined in Chapter 3 and in [130]) of an MEA can be defined by the equivalent number of elements of an ideal MEA (lossless, uncorrelated, equal power (MEG) in each branch, and no mutual coupling). The equivalence refers to having the same diversity gain, for a given diversity scheme

(e.g. Maximum Ratio Combining (MRC), Selection Combining (SC), etc.) and in a given propagation scenario. Similarly, a capacity order is the number of elements of an ideal MEA which has the same theoretical capacity efficiency in the given propagation scenario. The diversity order may be different to the capacity order for the same MEA since they are defined differently, and clearly both will be less than the actual number of elements used in a viable MEA. The equivalent number of idealized elements of an MEA, denoted M_e, is from here on defined as the diversity order in this dissertation. It includes the impact of MEA efficiency, mutual coupling, correlation matrix, diversity scheme, statistical propagation scenario, etc. We do not further discuss the use of capacity, but it follows the same method.

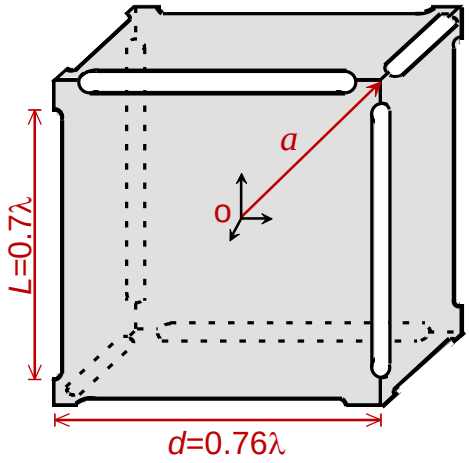

Figure 4.1 A realized hollow slot cube MEA

As an example, in Fig. 4.1, a 12-element hollow slot cube MEA [128][130] is used to demonstrate how to determine M_e based on its diversity order. The design detail and performance of this MEA is in Chapter 7 and in [130]. It has a

symmetric structure with 12 slot elements (L=0.7λ long) on the edges of a hollow metal cube. The diversity gain (G_{div}) of the MEA is available from the cumulative density function (*CDF*) of the *SNR* for a certain diversity scheme and in a certain propagation scenario. Statistical modelling of different propagation scenarios is an ongoing research subject, *cf.* [72]. In this dissertation, we adopt some simplified models, for example, summarized in [66].

(a)

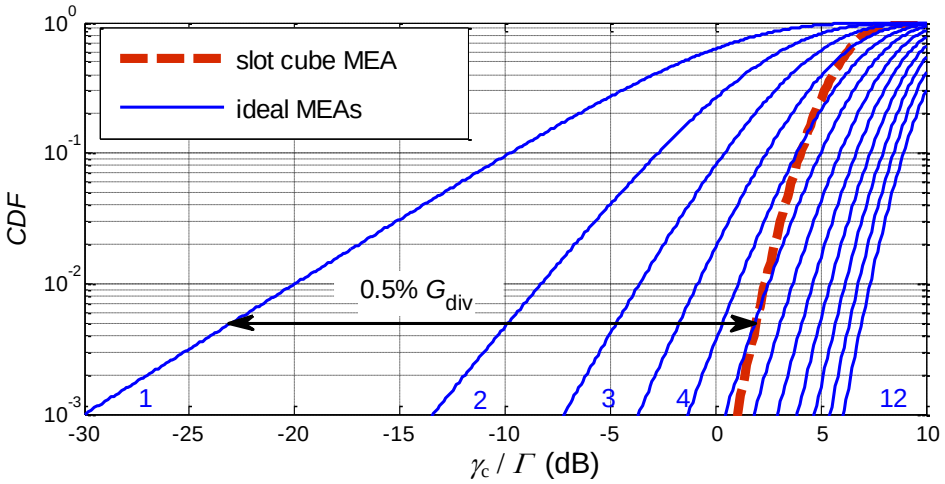

(b)

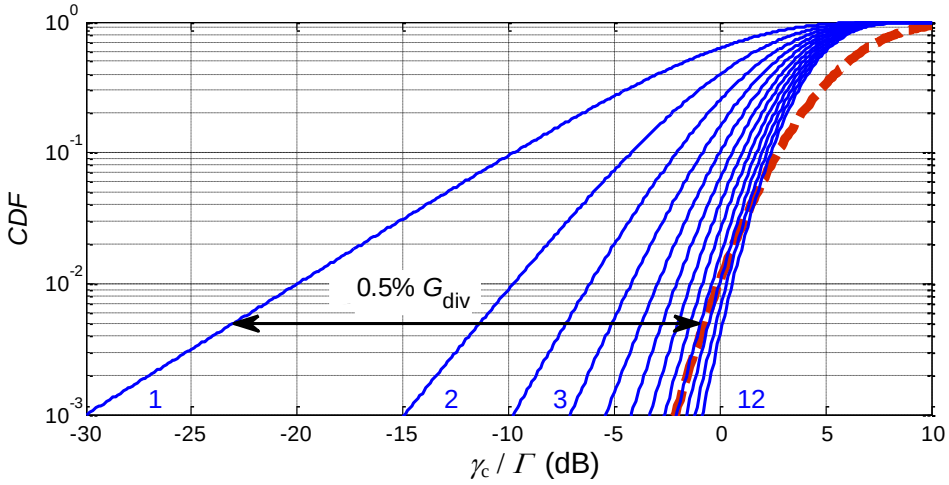

Figure 4.2 *CDF* and G_{div} of the slot cube MEA

(a) with MRC in an uniform scenario and (b) with SC in a Gaussian distribution scenario

This slot cube MEA is simulated, fabricated and measured. The results are in [128] and also in Chapter 7. The simulation and measurement results agree, so only the data from simulation are used in this chapter. The methods to derive the *CDF* and G_{div} are given in Chapter 3 and the results are shown in Fig. 4.2(a) for MRC in a scenario of incoming waves uniformly distributed and angularly uncorrelated for both polarizations, and in Fig. 4.2(b) for selection combining in an indoor scenario of incoming waves with a Gaussian distribution (*XPR*=5dB, $m_V=m_H=10^o$, $\sigma_V=\sigma_H=15^o$. The mathematical descriptions of these types of propagation models are described in, e.g., [12][66]. Other diversity schemes and propagation models can be applied with the same method, as in Chapter 3. The comparison of these results is for the purpose of demonstrating the way M_e is different for the same MEA when it is used in different scenarios or with different diversity combining.

All the solid curves in Fig. 4.2 are for the well-known *CDF*s of ideal MEAs (lossless, uncorrelated, equal power in each branch, and no mutual coupling) with 1 to 12 elements from the left to the right of the plot. The dashed curves are for the slot cube MEA. The double arrows show G_{div} at the probability of 0.5%, which indicates the realistic slot cube MEA has the same G_{div} as a 6-element ideal MEA in Fig. 4.2(a) and as a 9.5-element ideal MEA in Fig. 4.2(b). Thus, the diversity order is 6 and 9.5 in these two examples, so M_e=6 and 9.5, respectively. The detail of how the diversity schemes and propagation scenarios impact the MEA diversity order is discussed in Chapter 3.

4.3 Effective Element Electric Radius

The spherical compactness of a single element antenna can be characterized by the electric radius in radians (or electrical circumference in radians), denoted *ka*, of the inscribing sphere of the antenna [14]. An antenna with $ka \leq 1$ is considered electrically small, although some authors choose to define a compact antenna with $ka \leq 0.5$. For a thin wire half wavelength dipole, we have $a \sim \lambda/4$ and $ka \sim \pi/2$.

An MEA is normally larger than a single element antenna, but it can normally achieve better communications performance. For a fair comparison with the single element antenna, the volume of the inscribing sphere for an MEA is here normalized by its equivalent number of idealized elements, in the context of its performance.

The spherical volume which includes all the MEA elements (and any groundplane, matching circuits, etc.) is denoted V_{MEA}, and the normalized volume (an effective element volume) is V_e, where

$$V_e = V_{MEA} / M_e = \frac{4}{3}\pi a^3 / M_e = \frac{4}{3}\pi a_e^3 \tag{4-1}$$

and a_e is the associated radius for V_e, obtained as

$$a_e = \sqrt[3]{\frac{3}{4\pi}\frac{V_{MEA}}{M_e}} = \frac{a}{\sqrt[3]{M_e}} \tag{4-2}$$

Thus, ka_e is an electrical radius per equivalent element of the MEA.

It is important to note that, for an MEA with a common groundplane shared between antenna elements, the groundplane impacts the impedances and embedded patterns of the elements. For groundplane-mounted elements, the size of the groundplane often dominates V_{MEA}. When the antenna elements are moved round on such a fixed-size groundplane, V_{MEA} may retain the same value, but the mutual coupling may vary, so the MEA performance and the resulting M_e may vary. In this way, this type of change of the MEA configuration will be reflected in the values of V_e and a_e in Eqs. (4.1) and (4.2).

4.4 Efficiencies of MEA Elements

For a transmitting MEA, an embedded element refers to when this element is transmitting and the others are terminated according to the diversity signal combining scheme (e.g., open or short circuited, or loaded with their transmit source impedances). As discussed and formulated in Chapter 3, the efficiency of an MEA element is the total efficiency seen at the port of the embedded element. This efficiency is defined in the context of the mutual coupling, the diversity combining scheme and the corresponding terminations of the elements. The efficiency of receiving MEAs is also derived and the antenna reciprocity for MEAs is confirmed in Chapter 3.

For an embedded element, the radiation is not just from the excited element, but also from the other elements caused by mutual coupling. There are multiple causes of loss in an MEA, and they fall under two categories: the ohmic loss and the return loss. The return loss relates to the impedance mismatch between the source impedance and the input impedance of the embedded

element. The ohmic loss is the total ohmic loss in the entire MEA caused by the excited element. It includes the ohmic loss in the excited element, plus the ohmic loss in other elements and in the supporting structure, plus the loss in the loads of the other elements. The losses in the other elements and their loads are caused by mutual coupling, and it is referred to as the mutual coupling loss.

At an impedance resonance, each embedded element of the MEA can be modelled with a single resonance circuit. For example, a series *RLC* circuit is for a resonance, and a parallel *RLC* circuit is for an anti-resonance. Here the circuit model resonance is defined in the classical way by the reactance being zero. However, an actual antenna resonance is often better defined by the maximum of the resistance (or conductance) where its slope is zero, and here the reactance (or susceptance) is not necessarily zero, although its slope is likely a maximum. The simple circuit model can break down on this point, especially for higher order resonances present in electrically large structures. Moreover, the best available impedance match, or the centre frequency for the best match over a bandwidth, may not be at a resonance. However, for electrically small antenna elements at the first resonances considered below, we deal with impedance behaviour that tends to coincide with the circuit resonance behaviour.

Fig. 4.3 shows the terminology for the circuit model when taking the element 1 of an MEA at a resonance as an example. The input impedance of this embedded element is denoted

$$Z_{in,1} = R_{in,1} + jX_{in,1} = (R_{rad,1} + R_{\Omega,1}) + j(\omega L_1 - \frac{1}{\omega C_1}) \tag{4-3}$$

where $R_{rad,1}$ is the radiation resistance as seen by the embedded element. Again, note that the radiation power is from element 1 by direct excitation, as well as from the other elements through mutual coupling. Likewise, $R_{\Omega,1}$ presents the ohmic loss of the entire MEA, when the element 1 is excited and the rest of the MEA elements are present and terminated. The source resistance, $R_{s,1}$, is typically 50Ω, and ω is the usual angular frequency. The *LC* circuit represents the stored energy as seen by the embedded element.

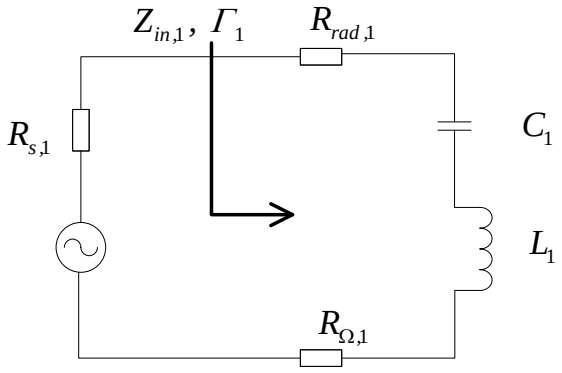

Figure 4.3 Circuit model of the MEA element 1 at or near resonance

The total efficiency of the embedded element 1 is decided by the matching efficiency, $\eta_{match,1}$, of the input impedance of this element to the excitation source impedance, and its embedded radiation efficiency, $\eta_{rad,1}$, as

$$\eta_{total,1} = \eta_{match,1}\eta_{rad,1} \tag{4-4}$$

where

$$\eta_{match,1} = 1 - \left|\Gamma_1\right|^2, \quad \Gamma_1 = (Z_{in,1} - R_{s,1})/(Z_{in,1} + R_{s,1}) \tag{4-5}$$

$$\eta_{rad,1} = \frac{R_{rad,1}}{R_{rad,1} + R_{\Omega,1}} = \frac{\eta_{total,1}}{1 - |\Gamma_1|^2} \tag{4-6}$$

and Γ_1 denotes the input reflection coefficient at the resonance of the embedded element 1. The *total efficiency* of the embedded elements with different diversity schemes and for the receiving MEAs is discussed in Chapter 3.

Eq. (4-6) leads to an expression of $R_{\Omega,1}$ in terms of $R_{rad,1}$ and $\eta_{rad,1}$, *viz*.,

$$R_{\Omega,1} = R_{rad,1}(1 - \eta_{rad,1}) / \eta_{rad,1} \tag{4-7}$$

which is used in the next section for deriving the radiation quality factor of the embedded element 1. For a zero radiation efficiency, the ohmic loss resistance becomes infinite, i.e., an open circuit.

There is a special class of MEA structures which are symmetric in the sense that each element sees an identical structure of elements around it. The analysis of these structures becomes simplified because if all the terminating impedances are the same, then all the elements will see the same impedance on transmit, and will invoke the same total radiation and losses, and the same efficiencies. Conversely, for a general MEA, there is asymmetry in the sense that the elements will have different losses and efficiencies. Some MEA examples below are symmetric, but the discussion is not limited to the symmetric structure.

4.5 Quality Factors of MEA elements

The quality factor for single element antennas [80][135]-[142] is classically defined using the derivative of the reactance, X_{in}, (or the susceptance, when

dealing with admittance). The use of the derivative of the impedance, Z_{in}, is proposed in [79] and this is equivalent to using X_{in} for a single narrowband resonance, because the slope of the resistance is zero ($\partial R_{in,1}/\partial\omega$=0). The quality factor of the embedded element 1, Q_1, is

$$Q_1 = \frac{\omega}{2R_{in,1}}\left|\frac{\partial Z_{in,1}}{\partial\omega}\right| = \frac{\omega}{2(R_{rad,1}+R_{\Omega,1})}\left|\frac{\partial Z_{in,1}}{\partial\omega}\right| \tag{4-8}$$

With Eqs. (6) and (7), Q_1 can be written as

$$\begin{aligned} Q_1 &= \frac{\omega}{2R_{rad,1}(1+(1-\eta_{rad,1})/\eta_{rad,1})}\left|\frac{\partial Z_{in,1}}{\partial\omega}\right| \\ &= \eta_{rad,1}\frac{\omega}{2R_{rad,1}}\left|\frac{\partial Z_{in,1}}{\partial\omega}\right| \\ &= \eta_{rad,1}Q_{rad,1} \\ &= \frac{\eta_{total,1}}{1-|\Gamma_1|^2}Q_{rad,1} \end{aligned} \tag{4-9}$$

Thus,

$$Q_{rad,1} = \frac{1-|\Gamma_1|^2}{\eta_{total,1}}Q_1 = \frac{1}{\eta_{rad,1}}Q_1 \tag{4-10}$$

where $Q_{rad,1}$ is the radiation quality factor of the embedded element 1 at the resonance. Since Γ_1 and $Z_{\text{in},1}$ (which derives Q_1 with Eq. (4-8)) can be directly measured at the port of the embedded element with a Vector Network Analyzer, and $\eta_{total,1}$ is usually measured with an anechoic chamber or perhaps a Wheeler cap, $Q_{rad,1}$ can be found with these measurements.

Note that Eq. (4-8) is for single resonance [79], so the derived Q_1 and $Q_{rad,1}$ are also for a single resonance. Most compact elements operate at their first resonance, so the above derivations hold for such MEAs. For the element being embedded with other elements which are contributing resonant behaviour at close frequencies, some care is needed here, but the basic method is still valid, as noted below.

Q_{rad} denotes the radiation quality factor of the whole MEA, and it must be a combination of the radiation quality factors of the embedded elements. For a symmetric MEA, the elements are identical, so Q_{rad} of the MEA is the same as that of the elements. But for asymmetric MEAs (and for practice symmetric MEAs which may not have ideally identical elements owing to fabrication errors), each embedded element may have a different radiation quality factor, so a certain combination is required to get an effective value of Q_{rad} for the MEA. A preferred way is to take the highest element radiation quality factor from all of the embedded elements. Another way is to take the average over all the elements. The example MEAs used in this dissertation are symmetric, so the averaged Q_{rad} is used, but the approach is not limited to such a structure.

4.6 Chu-McLean Diagram of MEAs

Chu's expression of Q against ka is the basis of evaluating antenna element spherical compactness. Chu's limit gives a size and bandwidth tradeoff limit for lossless antennas. Therefore Q relates to radiation conditions only, denoted above as Q_{rad}.

To demonstrate how to find Q_{rad}, one lossless first resonance dipole and some dipole MEAs are used as examples. The MEAs include:

1) A symmetric MEA which includes 12 first resonance dipole elements on the edges of a cube shape [13][49], as depicted in Fig. 4.4(a). The ratio of the dipole wire radius to its length is 0.007, a typical “thin dipole” value. The dipole elements are considered matched (an idealized matching circuit is assumed), and the mutual coupling between the elements is omitted, as per [49], and there is no feed structure or associated matching networks in the simulation, but the elements are lossy (embedded element radiation efficiency η_{rad}=0.5) and perfectly lossless (η_{rad} =1), respectively.

2) The second antenna is a single, lossless, first resonance dipole which is the same as the elements of the dipole cube.

3) A selection of linear, first resonance dipole arrays with 2 to 4 elements. As above, the arrays are assumed to be matched and uncorrelated, but with η_{rad}=0.5 and 1, respectively.

4) A selection of circular, first resonance dipole arrays with 3 to 6 elements. Similarly, the elements are matched and uncorrelated, with embedded element radiation efficiency of η_{rad}=0.5 and 1, respectively. A 4-element circular array is depicted in Fig. 4.1(b) as an example.

The spacing between the adjacent elements in the linear and circular array is the length of the dipole, so the mutual coupling is small and the MEAs can be assumed to be uncorrelated for a uniform propagation scenario.

For reference, Fig. 4.5(a) shows the simulated (with the so-called Finite Integration Technique [143]) input impedance of the lossless, single dipole against its electrical length, and Fig. 4.5(b) gives the computed radiation quality factor with Eqs. (4-8) and (4-10). (For this idealized reference antenna, the simulated total efficiency is 100% with the input reflection coefficient zero). At the first resonance of L/λ=0.45 (X=0Ω and R=68Ω, *cf.*, [144]), Q_{rad}=4.75 and it is plotted against the dipole electrical radius of $ka=(2\pi/\lambda)\times L/2$=1.41 with an asterisk in Fig. 4.6.

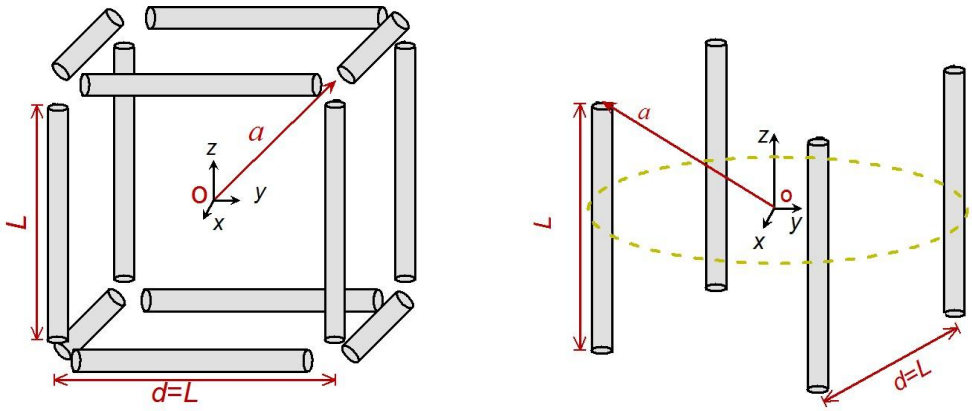

Figure 4.4 Example MEAs

(a) dipole cube and (b) circular dipole array

In Fig. 4.6, Q_{rad} of the idealized dipole cube MEA against its ka_e is plotted with a cross mark. Since the mutual coupling between the elements is omitted, each element is not influenced by the presence of other elements, so all the element are assumed to have the same radiation quality factors at the

resonances, so Q_{rad}=4.75 for this dipole MEA. Additionally, with the elements taken as lossless, matched and uncorrelated, the equivalent number of idealized elements (or the diversity order) is taken to be the same as the number of the dipole elements (M_e=12). As a result, ka_e of this dipole MEA is:

$$ka_e = \frac{2\pi}{\lambda}\frac{a}{\sqrt[3]{12}} = 1.07, \qquad \text{where} \quad a = \frac{\sqrt{3}}{2}L,\ L = 0.45\lambda \tag{4-11}$$

Note that the dipole cube is calculated as more compact than the single dipole since its ka_e is shorter. This is due to its improved communications performance. But if this dipole MEA is not idealized, its M_e value will be less than the number of elements and its ka_e will be larger, and it will be much less compact than depicted in the figure.

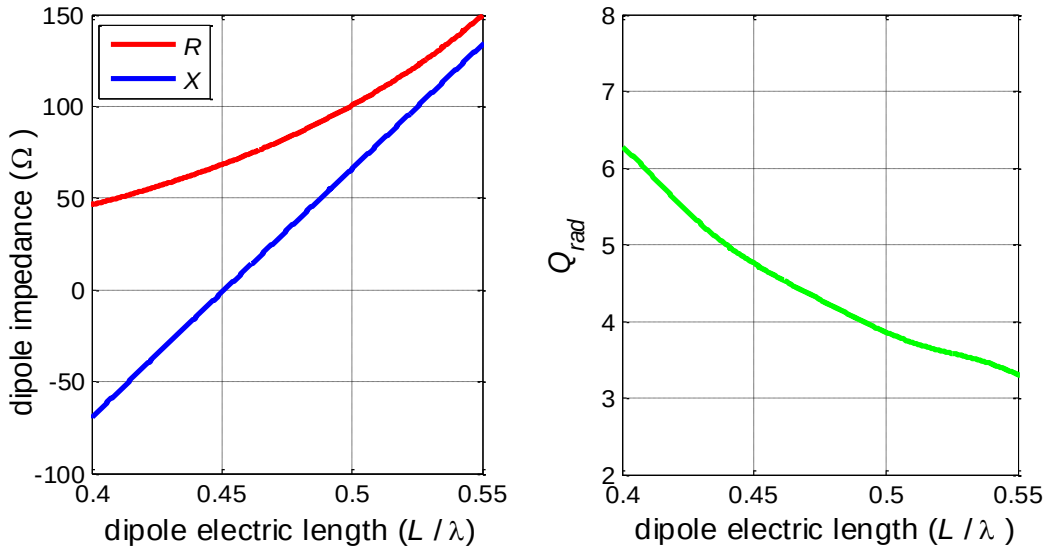

Figure 4.5 Simulated impedance and Q_{rad} of the single lossless dipole

(a) Impedance; and (b) Radiation quality factor near the first resonance

To see how the MEA efficiency impacts it compactness, the lossy (η_{rad}=0.5) dipole cube remains assumed uncorrelated, so the radiation quality factor is also Q_{rad}=4.75. The (unloaded) quality factor computed from the input impedance is reduced by half because of the antenna loss, see Eq. (4-9), and the feed point bandwidth is doubled. Furthermore, if all the elements are matched, the 0.5% diversity order is reduced to M_e=7.8 read from Fig. 3.6 for η_{rad}=0.5. As a result, the effective element electrical radius of this lossy 0.45λ MEA is

$$ka_e = \frac{2\pi}{\lambda}\frac{a}{\sqrt[3]{7.8}} = 1.23, \qquad \text{where, } a = \frac{\sqrt{3}}{2}L,\ L = 0.45\lambda \tag{4-12}$$

Q_{rad} of this lossy dipole cube against its ka_e is plotted with a cross in Fig. 4.6 for comparison.

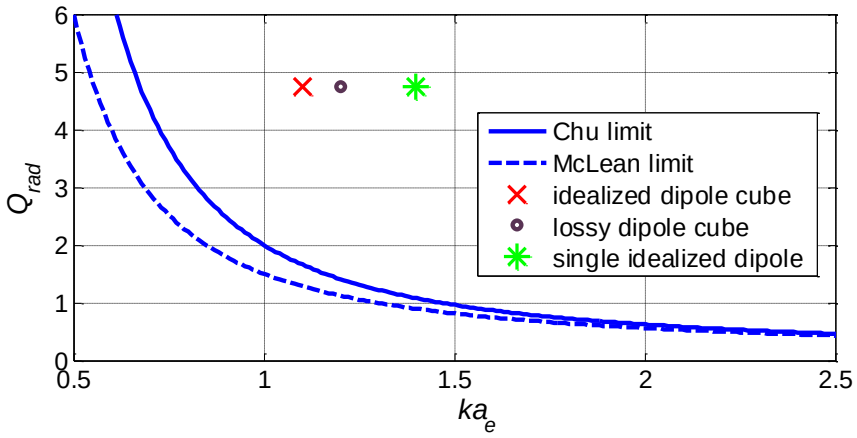

Figure 4.6 Q_{rad} against ka of a single dipole and ka_e of the dipole MEAs

Although ka_e is associated with the electrical size of the MEA, it contains no bandwidth information, so alone it cannot quantify the compactness of the MEA. The next section discusses how to associate ka_e and Q_{rad} to define a space efficiency and evaluate the compactness of MEAs.

4.7 Space efficiency for evaluating MEA compactness

A space efficiency, η_{space}, is presented here which measures the compactness of the antenna. η_{space} is defined as the ratio of the electrical radius on the Chu limit, ka_{Chu}, at the given MEA Q_{rad}, over the MEA's ka_e, ie.,

$$\eta_{space} = ka_{Chu} / ka_e \quad , \text{ at the } Q_{rad} \text{ of the MEA} \tag{4-13}$$

The value of η_{space} is from 0 to 1. Unity space efficiency is when the MEA is on the Chu limit. For increasingly lossy MEAs, the diversity gain and capacity efficiency of the MEA are decreased caused by the lower antenna efficiency, as discussed in Chapter 3. The resulting M_e is smaller, so ka_e increases (Eq. (4-2)), and η_{space} decreases.

Table 4.1 shows the parameters leading to the space efficiencies presented in Fig. 4.6. It compares the dipole cube MEA with the linear and circular arrays of first resonance dipoles with half wavelength spacing. The dipole elements are matched, uncoupled, uncorrelated, and their signals are combined using perfect MRC. When the dipoles elements are lossless, their M_e is the same value as their element numbers. For lossy MEAs, M_e is obtained from Fig. 3.6 for the equivalent diversity gain at the probability of 0.5%.

Table 4.1 Comparison of different matched, uncorrelated dipole MEAs

	number of elements	M_e	ka_{Chu}	ka_e	η_{space}
idealized single dipole	1	1	0.7	1.41	0.5
idealized linear dipole array	2	2	0.7	1.59	0.44
	3	3	0.7	2.19	0.32
	4	4	0.7	2.82	0.25
lossy linear dipole array (η_{rad}=0.5)	2	1.4	0.7	1.79	0.39
	3	1.9	0.7	2.55	0.27
	4	2.2	0.7	3.44	0.20
idealized circular dipole array	3	3	0.7	1.49	0.47
	4	4	0.7	1.54	0.45
	5	5	0.7	1.63	0.43
	6	6	0.7	1.74	0.4
lossy circular dipole array (η_{rad}=0.5)	3	1.9	0.7	1.72	0.41
	4	2.2	0.7	1.88	0.37
	5	2.7	0.7	2.00	0.35
	6	3.0	0.7	2.20	0.32
idealized dipole cube	12	12	0.7	1.07	0.65
lossy dipole cube (η_{rad}=0.5)	12	7.8	0.7	1.23	0.57

Fig. 4.7 gives η_{space} of these MEAs against their equivalent numbers of idealized elements. The idealized MEAs give reference space efficiency curves for these familiar arrays, which are often discussed in the array literature. The idealized dipole cube has the highest space efficiency. The lossy dipole cube has nearly 10% lower space efficiency than the idealized cube, and this space efficiency reduction is from the diversity performance reduction caused by the ohmic loss of the MEA elements.

The space efficiency provides a method to evaluate the compactness of MEAs in the context of their communications performance, but, as with any antenna parameter, it does not directly provide the methods on how to design a

more space efficient MEA. However, the ability to compare different MEAs suggests some design guidelines, as discussed below.

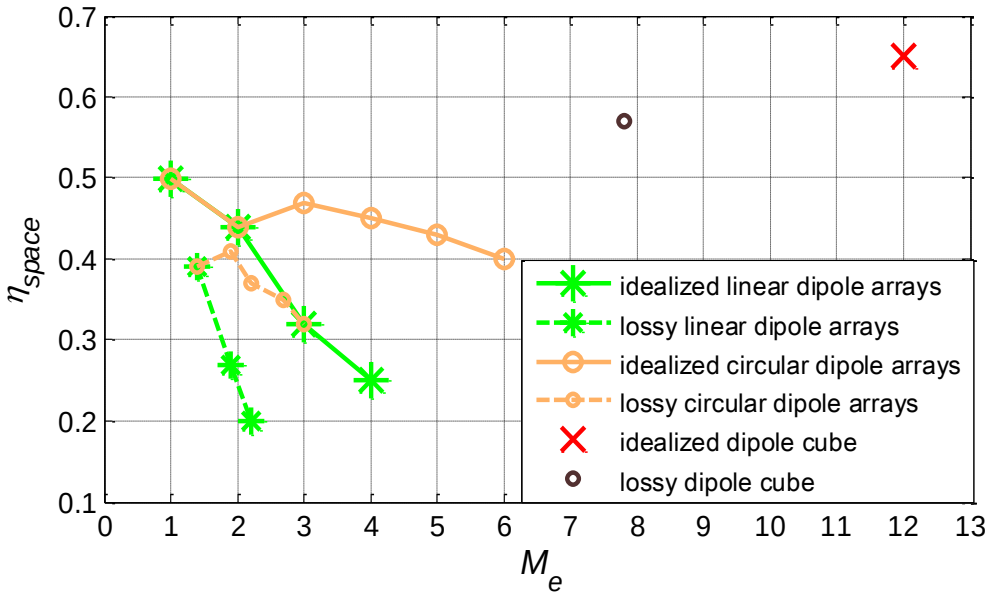

Figure 4.7 Comparison of space efficiencies

In Fig. 4.7, η_{space} of the linear dipole MEAs decreases quickly with the number of elements. The circular MEAs follow the same trend but in a slower fashion. This demonstrates how the linear array is not well suited to a spherical volume. Similarly, the circular configuration is also not well suited to a spherical volume measure, especially when the number of elements becomes very large and its profile reduces to only a Great Circle locus on the sphere. The idealized dipole cube MEA achieves the highest η_{space} among these MEAs since it fills the sphere more efficiently. For a treatment of generalized volumetric shapes, see

[145]. The comparison of the idealized dipole MEAs suggests volume configuration can greatly increase the MEA space efficiency.

But if the dipole cube is a realistic MEA with the losses and correlations considered, its η_{space} will be reduced drastically. This is observed from the lossy dipole cube in Fig. 4.7.

The space efficiency formulation is general, with no limitation on the antenna configuration, for example the electrical distance between the antenna elements. Mutual coupling effects are included in M_e. When the mutual coupling is very high, the performance becomes poor as expected, so the resulting M_e is small, and ka_e is larger, and the space efficiency is smaller.

Although it is not demonstrated here, for brevity, the space efficiency for the same MEA with different diversity schemes or in different propagation environment is different. The derivation is straightforward from the definition of M_e in Section 4.2. The example of M_e=6 for the slot cube MEA with MRC and in an uniform scenario, and M_e=9.5 for the same MEA with SC and in an indoor environment demonstrates the different space efficiencies for the same MEA in different scenarios with different combining methods.

4.8 Conclusion

The evaluation of MEA compactness is discussed with respect to the antenna bandwidth and MIMO communications performance, *viz*, the diversity order. An equivalent number of idealized elements of an MEA is defined from the diversity gain in the context of the propagation scenario, diversity scheme,

antenna correlation, and embedded element efficiencies which contain the mutual coupling losses. This equivalent number can also be defined from other communications performance measures such as the capacity efficiency. The space efficiency is defined using this equivalent number of elements and an MEA radiation quality factor. The space efficiency evaluates the spherical compactness of an MEA with respect to the MEA bandwidth and communications performance. It includes the impact of MEA efficiencies, mutual coupling, correlation, diversity scheme, and propagation scenario. Therefore, this space efficiency also provides a method to compare different MEAs in different propagation scenarios. Some MEAs presented in the literature are used as examples, as well as some idealized dipole MEAs for reference, and these offer design guidelines for antenna configurations.

CHAPTER 5: OPEN SLOT ANTENNA IN A FINITE GROUNDPLANE

The above chapters discuss MEA evaluation techniques. From here on, the focus is on slot elements and slot MEAs for MIMO applications. In this chapter, the open slot antenna in a finite groundplane is investigated. The impact of the finite groundplane on the open slot antenna performance is studied parametrically and the far field pattern behaviour is clarified. The pattern of this slot configuration is fundamentally different from its complementary dipole. Here, a parametric study of a slot antenna is presented including the impact and use of a finite groundplane with different sizes and bending angles along the slot axis. As a result, we demonstrate a simple, effective antenna comprising a slot in a small groundplane, which has direct matching to 50Ω, high efficiency and medium gain over a wide bandwidth. The slot length at the second resonance dictates the centre frequency, and the slot width influences the bandwidth. Only a small groundplane is required to maintain the performance. The impedance is also insensitive to the groundplane bending angle from 180^{o} (flat) down to 30^{o}. This bent groundplane configuration allows some control over the front-to-back ratio, and hence the directivity. The resulting slot antenna is exploited as elements of slot-based MEAs in the next two chapters.

5.1 Introduction

The slot antenna is a fundamental elemental antenna. It also has practical applications, in particular as a one-sided radiator in a metallic aperture, including in an array [107]-[109]. Here we are interested in the pattern and impedance behaviour for the open slot (double sided radiation), and particularly for a small groundplane. This configuration comprises an important element, as we show in the performance of new antenna examples, and yet has had almost no treatment in the literature. A finite groundplane is known to influence the impedance and pattern of an element mounted on the groundplane. The solution for a monopole centred on a circular groundplane, including the small groundplane case, has been solved [146][147], but this is not the case for the slot, and especially the open slot. The groundplane relationship cannot be inferred from the case of monopole on a groundplane to the case of slot in a groundplane.

Despite treatment in most texts and papers, there are aspects of the slot antenna in a finite groundplane that are not widely understood. Some examples are given here, and elaboration follows in later sections. Principal antenna texts include [4]-[52][148]-[150]. The basic slot material in these texts is similar, and the principles and some results are discussed for the single sided slot. Of these texts, only [52] and [148] mention the pattern of the open slot in a finite groundplane, although these are large groundplane examples. Of all the texts, [52] offers the most descriptive treatment, and here it states that the pattern is null in all directions on the groundplane. This is incorrect. Below we argue that ideally the co-polar component is indeed a null in all directions, and the cross-

polar pattern is finite and significant in all directions along the groundplane except exactly at broadside to the slot - where there is a null. To the authors' knowledge, no text specifically treats the small groundplane open slot (the smallest discussed is a relatively large 2λ by 2λ groundplane [148], where λ is the wavelength at the nominal centre frequency of operation). As befits the ongoing topicality and incremental understanding of the slot antenna, papers are continually being published, e.g., [151]-[176], but these are mostly for electrically large groundplanes (or with an unspecified groundplane size), and single–sided radiation (cavity backed arrangement). The basic diffraction solution for the relatively small 1.12λ groundplane is given in [153], but this is for the single-sided slot. The configuration is a half-wavelength slot located about a half wavelength from the edge, and yet uniform excitation of the groundplane edge is assumed (without elaboration) for the diffraction solution. It is unlikely that accurate analytic 3D pattern information can be obtained for such a small groundplane with such an approximation, although the pattern cut through the plane of symmetry can have reasonable accuracy. More recently, [154] claims that the cavity-backed, half-wavelength slot pattern is not sensitive to the groundplane size for large groundplanes (greater than 2λ by 2λ), and the patterns are still very similar for an electrically small size of about 0.5λ by 0.5λ. We show here that this is not the case for open slots. In particular, the pattern is very sensitive to the groundplane size when it transitions to larger than about a wavelength square. This is because of the spacing and strength of the edge diffraction contributions. For example, for a one wavelength square groundplane and smaller ones, we have

single lobed patterns at each side of the groundplane; but for groundplane larger than one wavelength square, we have a multiple lobes pattern, and the lobe number increases with the groundplane size.

There appear to be few papers on the open slot in a small groundplane. Experimental patterns for the open slot in a large 2λ by 2λ groundplane are given in [155]. The pattern shapes appear to be somewhat different to the results presented here, possibly due to large experimental error, but no explanation of the experimental setup is provided in [155]. Further to the comment above, [148] contains a Geometrical Theory of Diffraction (GTD) calculated pattern for a half-wavelength (first resonance) open slot in a large 2λ by 2λ groundplane.

In recent years, there has been increasing interest in how to feed slot antennas. This will not affect the basic radiation mechanisms and so should not significantly affect the patterns. Much of this literature has addressed microstrip-fed and CPW-fed printed slot antennas in mobile handsets and RFID tags, including UWB, WLAN/WiMAX and cognitive radio applications. Due to their simple fabrication and integration, low cost and low profile, much research has focused on the design and improvement of printed slot antennas, including tapered slots [156], circular slots[157], folded slots [158]-[160], fractal slots [161]-[163] and miniaturized spiral slots [164][165]. After the papers by Cary in 1952 and Johnson in 1955, notch, or monopole slot [149][166] is a derivation on the slot analogous to a monopole derived from a dipole. For printed slot antennas, a substrate is required on the groundplane. The groundplane is a necessary part of the slot antenna and is used to support feed lines to the slot. The minimum

required size for the groundplane has not been well-defined in previous literature, but the groundplane defines the total size of the antenna. In discussing compact antennas or antennas whose size is important, any matching circuit should be included in the total size for fair comparison. In most articles about printed slot antenna designs, the groundplane sizes are either decided by the size and configuration of the device (e.g. a cellphone), or not discussed. However, with the increasing need of small antennas for MIMO, the size of the slot antenna, including its feed structure and its supporting groundplane, becomes more critical. There is little analysis available on the effects of small groundplane (e.g. <~2λ square) and no parametric study of the small groundplane details has been previously reported.

In this chapter, the size of the small groundplane and its effect on the slot antenna are investigated in order to correct and augment the existing literature. We look at the simplest configuration - a basic open slot in a metallic groundplane. We feed centrally with a 50Ω coaxial cable. The groundplane is assessed parametrically, including its size, its shape and the slot position, for the effect on the impedance and pattern over a broad frequency range. When the groundplane dimensions are smaller than λ, the open slot antenna performance is insensitive to variations of groundplane detail over a wide bandwidth around the second resonance. However this is not the case for the usual first resonance, or half-wavelength slot. The slot width plays a key role in the antenna impedance at the second resonance. This has not been reported before, although its impact on the bandwidth at the first resonance is well known [166]-[168]. Further, we

introduce the groundplane bent along the slot axis to realize a new antenna configuration. The bending angle influences the pattern, with the 50Ω impedance bandwidth remaining essentially the same. There is an optimal angle for maximum directivity of a given (i.e., groundplane size) open slot-wedge. This has stand-alone applications as a particularly simple and effective antenna, or it can be integrated into complex-shaped platforms, such as conductive cases, as a MIMO antenna element.

In terms of analysis methodology, for infinite groundplanes, there are theoretical formulations of the slot antenna impedance and radiation patterns. They are often derived from the slot's complementary dipole [105][148]-[150]. When the groundplane is finite, i.e., the groundplane edges are part of the antenna, the edge diffractions become radiation sources. The impedance and patterns change with the size of the groundplane, as is known for large groundplane sizes [148]-[150][155][173], and there is no straightforward rigorous general solution. For this case when the groundplane is considered large (about 2λ squared and larger) and when the diffraction sources are in the far field of the slot, GTD [174] can be used to approximate the patterns, but not in all directions, as mentioned above. When the groundplane is small and the diffraction sources are in the near field of the slot, GTD can no longer be easily applied. In general, physical measurement and numerical solution are the only estimation techniques for the antenna impedance and patterns in this case. The methods used in this dissertation are: 1) the Finite Integration Technique (FIT) [143] for numerical simulation of impedance and radiation patterns, with internally supplied values for

the conductivity of copper; 2) network analyzer [177] for impedance measurement; and 3) anechoic chamber [178] for radiation pattern measurement. Here, the claimed gain accuracy is < ±0.5dB and pattern accuracy < ±2dB@-20dB.

The rest of the chapter is organized as follows. In Section 5.2, we review the impedance and pattern behaviour of a slot in a finite groundplane using numerical and physical experiments. This lays the basis for the discussion in Section 5.3 on the groundplane effects, including the change of the size, shape and the slot position. This discussion extends to very large groundplane as well, for a better understanding of the finite groundplane effects. The minimum groundplane size is found that retains the practicality of the second resonance (i.e., wideband) antenna for a given rectangular slot width to length ratio. In Section 5.4, the relation between the slot width and impedance bandwidth at the second resonance is discussed, followed by the slot-wedge at the second resonance and its applications as a MIMO antenna element in Section 5.5. Correlation of two orthogonal slot elements in different distances is studied through measurements in Section 5.6, with Section 5.7 concluding the chapter.

5.2 Open antenna in finite groundplane

The configuration of the antenna is illustrated in Fig. 5.1. The groundplane with the width (*a*), length (*b*) and depth (*d*) is placed in the *y*-*z* plane. The slot has width (*w*) and length (*L*), and it is cut centrally along the *z* axis and fed at the centre with a 50Ω discrete port in the simulations. In physical measurement, the

slot is instead fed with a 50Ω coaxial cable which is fixed flush to the groundplane, and loaded with ferrite beads to suppress currents on the outer conductor. The reflection is slightly reduced by using the beads, and the loss in the beads is negligible from gain comparisons. The inner and outer conductors of the cable are fixed to either side of the slot, as sketched in Fig. 5.1.

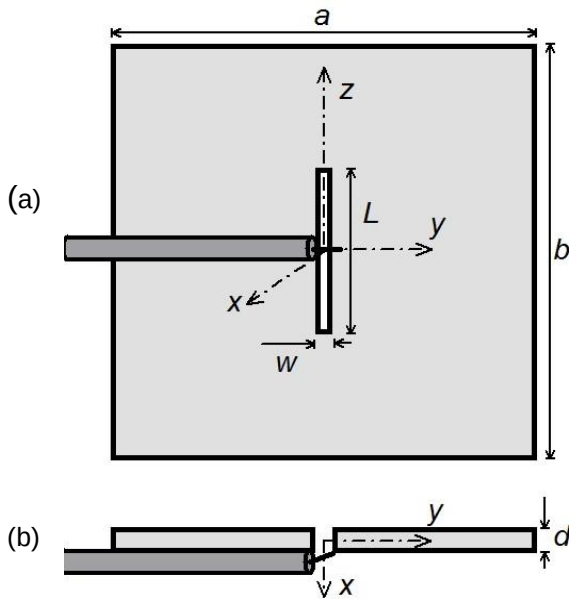

Figure 5.1 Centre fed open slot in a finite groundplane

(a) Front-view (*y*-*z* plane); (b) Cross section (*x*-*y* plane)

5.2.1 Input impedance

Such a slot with w=0.04L (and L=60mm) in a square copper sheet (a=b=2L, d=0.01L) was measured and simulated in the frequency range of 1 GHz to 5 GHz. The slot electrical length (L/λ) is therefore from 0.2 to 1, and the groundplane size is 2λ square for the upper frequency of 5GHz.

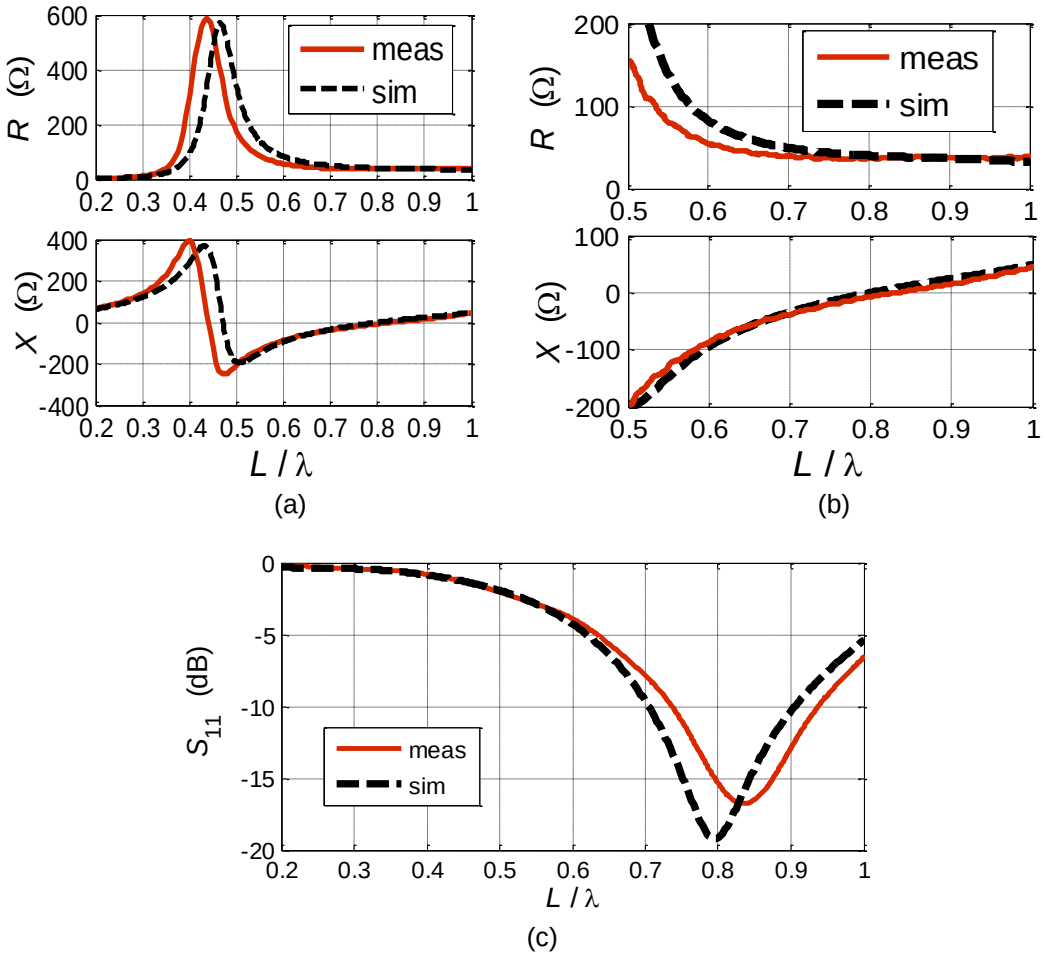

Figure 5.2 Comparison of measured and simulated slot in a finite groundplane

(a) Impedance over a wide bandwidth where the first and second impedance resonance are evident at zero reactance; (b) Impedance near the 2nd resonance where the reactance goes through zero at about L=0.8λ; (c) Refection coefficient

Fig. 5.2(a) gives the input impedances of the slot against its electrical length. The agreement between the measurement and simulation is poor around the first resonance, which is near L/λ=0.5 (f=2.5GHz) as predicted from the first resonance of the equivalent dipole. Here, the impedance is changing quickly and the bandwidth is rather narrow. Analysis and design of such narrowband regions

are sensitive to the measurement setup, the accuracy of dimensions and shape of the physically implemented antenna, and the numerical approach of FIT, and other simulation techniques.

The second resonant frequency range ($0.7 \leq L/\lambda \leq 0.9$) is of particular interest, as magnified in Fig. 5.2(b). Here, both the reactance and resistance change slowly with frequency, and the agreement between the measurement and simulation appears better. The resistances remain around 40Ω over the bandwidth of interest and stay essentially constant. This "flat" region provides a wide bandwidth, direct match to coaxial cable (50Ω), and for analysis and design, an improved tolerance to the differences between the results from the numerical models and the physical realization. The broadband feature of the second resonance has been noticed before [158][175][176] but not widely utilized. For a single resonance slot, the half-wavelength size is ubiquitously treated in the literature, and used in applications, but it does not have the wide bandwidth of the second resonance. By carefully choosing the location and the width of the strip feed, a microstrip-fed half wavelength wide slot can include two resonances within the -10dB bandwidth so that the bandwidth is significantly enlarged [166]-[168]. However, a larger groundplane area is required, and multiple pattern modes are included. In this dissertation, we are interested in the basic single resonance open slot antenna and the impact of the groundplane. An understanding of this fosters better antenna design and places broadbanding techniques in the context of a dominantly single mode slot.

In Fig. 5.2(c), the simulated reflection coefficient, S_{11}, shows the -10dB relative bandwidth is 25% at the second resonance where L/λ=0.8. The measured bandwidth is 27%, which is within reasonable agreement with the simulated result.

5.2.2 Radiation pattern

The normalized (maximum set to be 0dB) measured patterns of the same slot antenna are compared with the numerical results at the first two resonances in Fig. 5.3. For the slot along the *z*-axis, E_ϕ is the dominant component and E_θ is much lower. Unlike a dipole whose patterns are described in just two planes – the so-called *E*- and *H*-plane, the slot antenna has different patterns in the three Cartesian planes. Fig. 5.3 shows the patterns in the *x-y, x-z* and *y-z* planes, and they convey a lot of information.

Fig. 5.3(a), 5.3(b) and 5.3(c) are the normalized patterns at the first resonance (L/λ=0.5) in the three Cartesian planes respectively, and 5.3(d), 5.3(e) and 5.3(f) are at the second resonance (L/λ=0.8). E_θ in the *x-y* and *x-z* planes and E_ϕ in the *y-z* plane from simulations are below -80dB, so are not shown. From measurements they are mostly below -20dB. The difference between the measured and the simulated patterns includes the finite accuracy of both simulations and chamber measurements, the construction accuracy, the orientation of the antenna under test, and the different feeds used in simulation and measurement.

There are no measurement data for a cone of about 30 degrees cantered at -z axis (θ=180°). This is because of the support platform in the chamber. The missed data can impact the directivity calculation and care must be taken to minimize this effect.

In the direction along *y*-axis, the E_ϕ pattern has nulls, as suggested in [51][52][148], owing to the opposite polarities of the E_ϕ components from each side of the finite groundplane along the y-axis. The symmetry of the groundplane to the *x*-*y* plane is critical for creating these pattern nulls. There is no direct excitation of the E_θ component for this direction.

There is no component cancellation, and associated pattern nulls, along the *z*-axis where a null would be expected for the electric dipole. This is different to what is stated in [52] – *viz.*, that there is a null in all directions of the groundplane. The E_θ component is non-zero in the groundplane directions. In the *y*-*z* plane, E_θ is the dominant component but is small, mostly in the range of -10dB to -20dB, except at the "nulls" (< -80dB in the simulation) along the *y*-axis. In the measurement, the E_θ null in the positive *y*-axis direction is not evident. This is considered as measurement error, probably from a feed alignment issue. The maximum E_θ is along the *z*-axis, where the components originating from each side of the groundplane add constructively.

At the second resonance, the fixed size groundplane is electrically larger, so the pattern starts to undulate, as is well known, because of the larger electrical spacing of diffraction source (groundplane edge) contributions. The

peaks of the pattern move away from the *x*-axis and there are two peaks at each side of the groundplane, as can be seen in Fig. 5.3(d).

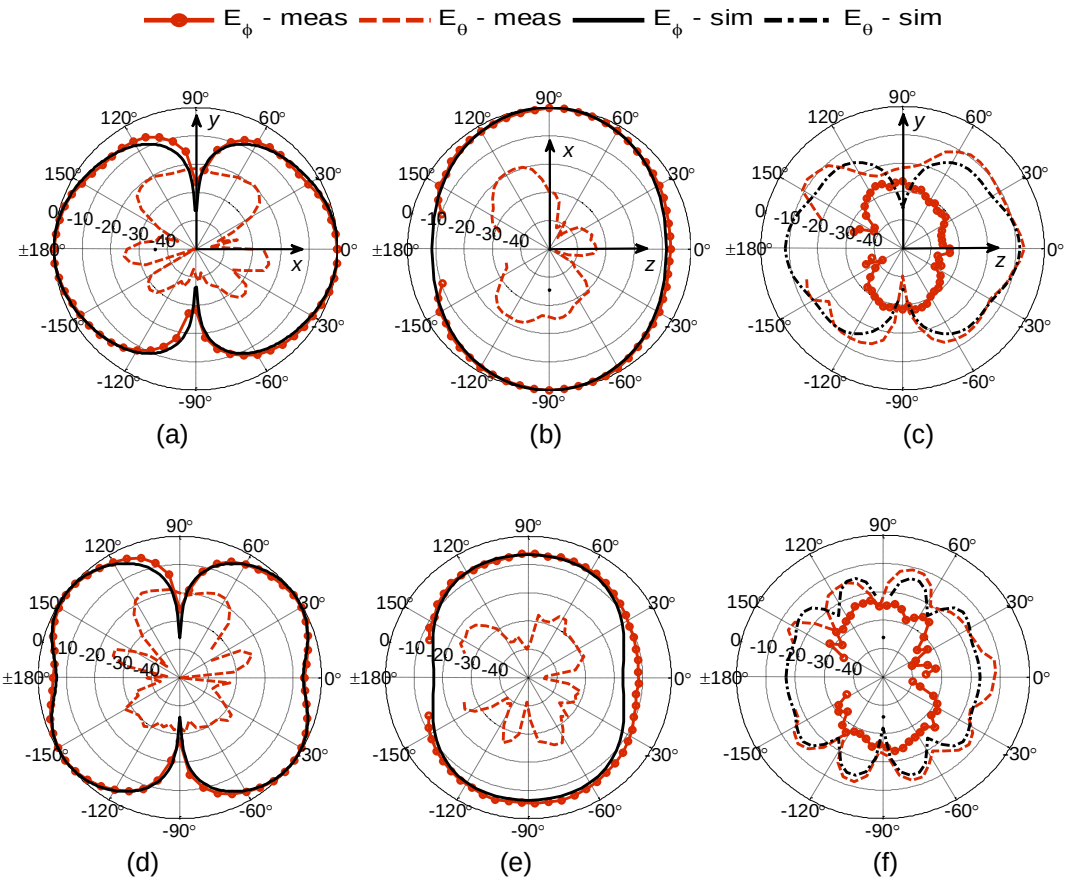

Figure 5.3 Comparison of measured and simulated patterns of an open slot

The normalized patterns in (a) *x-y* plane at L/λ=0.5; (b) *x-z* plane at L/λ=0.5; (c) *y-z* plane at L/λ=0.5; (d) *x-y* plane at L/λ=0.8; (e) *x-z* plane at L/λ=0.8; (f) *y-z* plane at L/λ =0.8

Up to this point, the measured and simulated impedances and patterns of a slot with fixed width and length in a finite groundplane are discussed. In the next section, the groundplane size, shape and the slot position are varied. Only

simulated patterns are presented and physically measured patterns are not used for this section owing to the agreement between these two methods shown above.

5.3 Impact of groundplane

5.3.1 Size of groundplane

The impact of the groundplane size on the slot impedance and pattern are studied by fixing the slot shape (w=0.04L) and changing the size of the groundplane. This is done in two steps: 1) reducing the overall size of the square groundplane from a=b=20L to a=b=1.04L; 2) further reducing the width, a, from 1.04L to 0.2L but retaining the length, b, at 1.04L. Here the groundplane takes a rectangular shape.

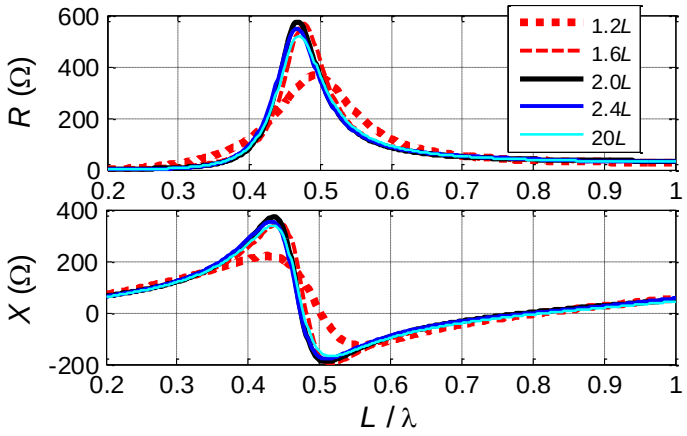

Figure 5.4 Simulated impedance over slot electric length in varied groundplanes

In Fig. 5.4, simulated impedances against the slot electric length for a few sample groundplane sizes are compared. This figure shows that the impedance

at the first resonance is sensitive to the change of the groundplane size. The change is more than a couple of hundred ohms when the groundplane is small. However, at the second resonance, the impedance remains rather stable, explaining its wideband character.

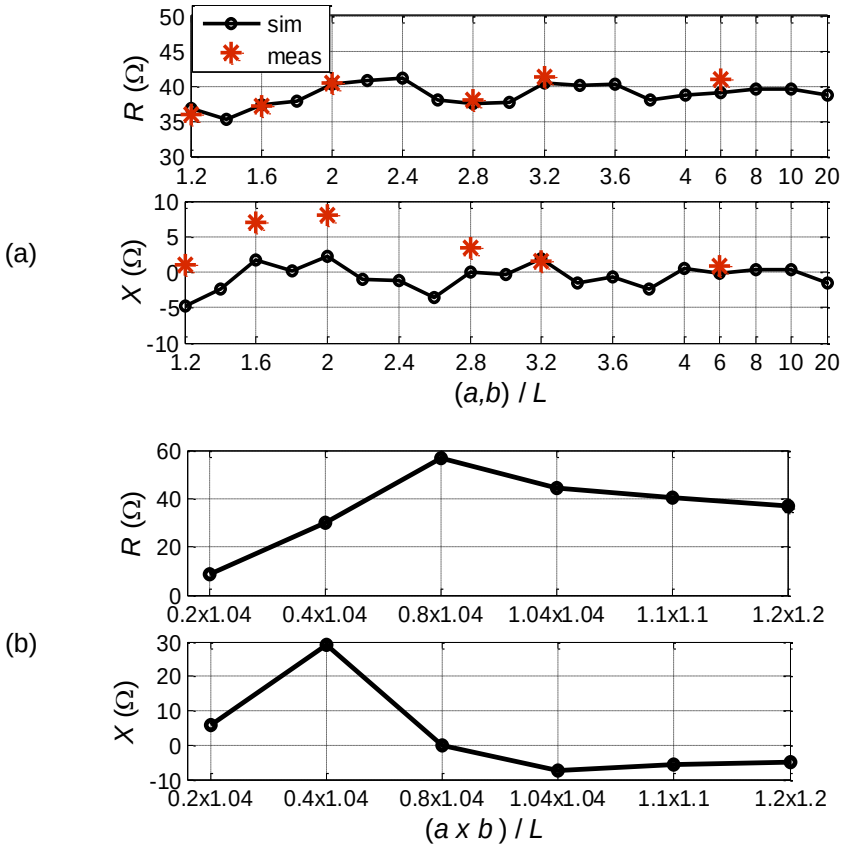

Figure 5.5 Variation of slot impedance against different groundplane size

(a) Simulated(circles) and measured (stars) impedance at L/λ=0.8 for slot in square groundplane

(b) Simulated impedance at L/λ=0.8 for slot in rectangular groundplane. The larger groundplane (to the right of 1.04) is square; and the smaller groundplane (to the left of 1.04) is rectangular

Fig. 5.5 shows the simulated and measured impedances. Figs. 5.5(a) and 5.5(b) give the variation of the simulated impedance at the second resonance. Fig. 5.5(a) includes measured results of some sample sizes. For large ground planes - the square groundplane is reduced from $20L(16\lambda)$ to $1.04L(0.83\lambda)$, the resistance stays around 40Ω and reactance remains near zero, with a variation range within 5Ω. For small groundplanes - when the width of the groundplane is further reduced from $1.04L$ till $0.4L(0.32\lambda)$, and the groundplane becomes rectangular, conforming to the slot shape, the change of the impedance is more noticeable, but an acceptable match to 50Ω is still possible. When a is $0.2L$, the small groundplane size causes the resistance to drop to 10Ω. It can be concluded that the size of the groundplane required to maintain a wideband, direct match to 50Ω at the second resonance is about $1.04L \times 0.4L$ $(0.83\lambda \times 0.32\lambda)$, for the given slot shape ($w=0.04L=0.03\lambda$). For example, for 4GHz, this size is only about 62mm×24mm. The length (larger side) of the groundplane is governed by the length of the slot. Recall that for the usual first resonance slot, such a minimum does not exist since a small groundplane like this greatly changes the impedance.

In Fig. 5.5(a), the resistance agrees reasonably well between the simulation and measurement, whereas the reactance has some differences, especially for the smaller groundplane. One obvious source of discrepancy is the presence of the coaxial cable feed within the near field in the measurement.

We now look at the impact of groundplane size on the slot pattern. This is undertaken using both FIT for small and large groundplane and GTD for an even larger groundplane but in the x-y plane cut only.

Fig. 5.6 gives the patterns of the same slot, w=0.04L, in four different square groundplanes: a=b=1.2L, 2L, 3L, and 4L at L/λ =0.5 and 0.8, respectively. The patterns of the complementary strip dipole (same size as the slot) are also given for comparison. Fig. 5.7 includes both simulated and theoretically derived patterns from GTD for larger groundplanes in x-y plane. As mentioned above, for a slot along the z-axis, E_ϕ is the dominant far field component; for a dipole in the same orientation, E_θ is dominant (ideally it is pure). It can be seen in both figures that, as the groundplane size increases, the pattern undulations become denser, as expected. The nulls remain along the directions of the y-axis for all frequencies and all finite groundplane sizes.

In popular text books, E_θ is not discussed and, as such, seems to be assumed (although not stated) to be zero. However, it is finite in the plane of the finite groundplane, see Figs. 5.6 (e) and 5.6 (f). It is also stated in [52] that E_ϕ undulation owing to the finite groundplane size will decrease as the groundplane becomes large, and the pattern becomes close to a circular shape. This is correct, but we emphasize here that the circular shape has nulls in the direction of the y-axis and that these will remain regardless of the finite groundplane size, with a reducing null width as the groundplane size increases. This is demonstrated in Fig. 5.7 with GTD. For instance, for the square groundplane as large as 200L=160λ, the GTD pattern gives a 3dB null width in E_ϕ of about 5^o.

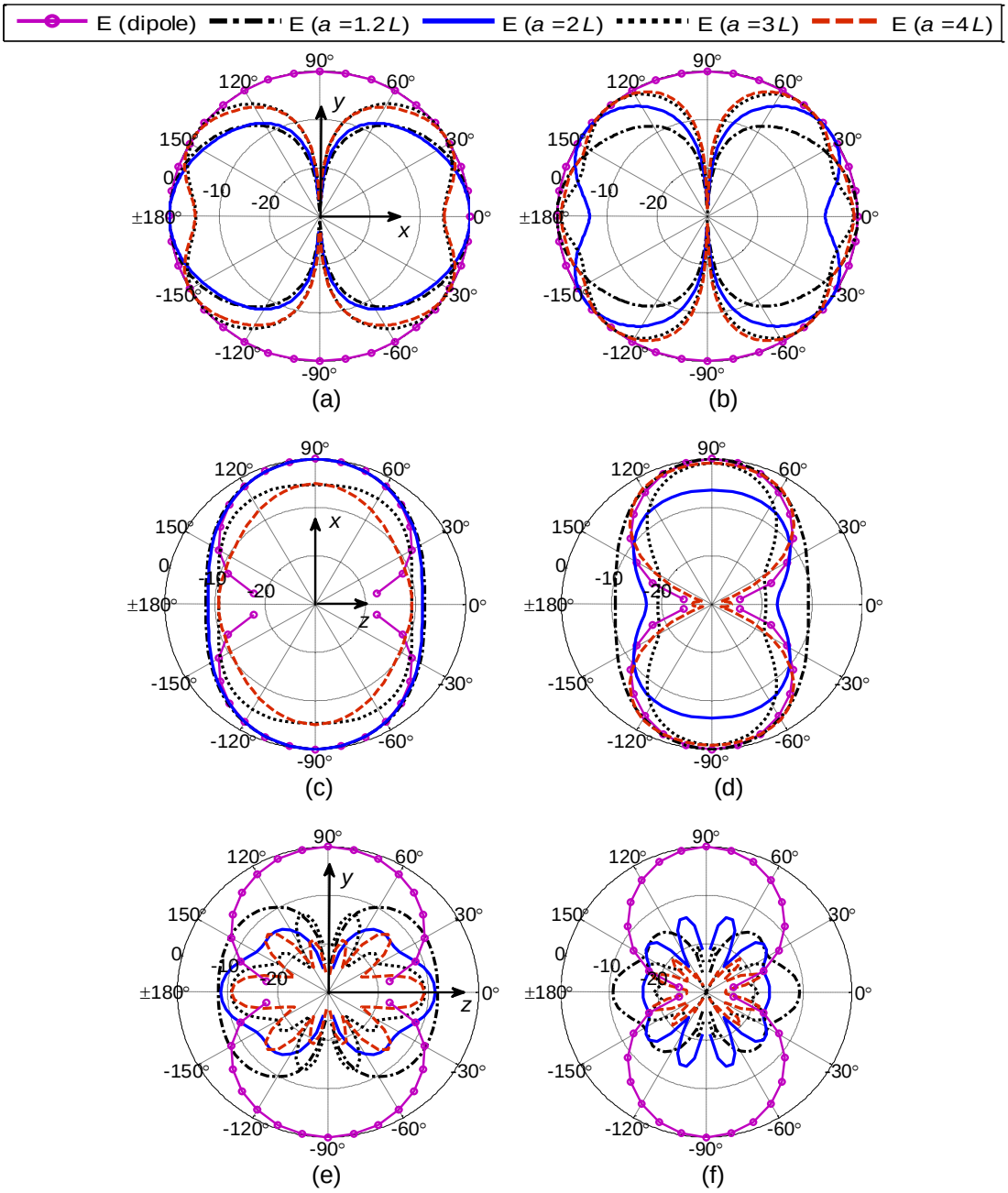

Figure 5.6 Simulated patterns of dipole and slots in various groundplanes

E_θ of dipole and E_ϕ of slot (a) in *x*-*y* plane at L/λ=0.5, (b) in *x*-*y* plane at L/λ=0.8, (c) in *x*-*z* plane at L/λ=0.5, (d) in *x*-*z* plane at L/λ=0.8, (e) in *y*-*z* plane at L/λ=0.5, (f) in *y*-*z* plane at L/λ=0.8

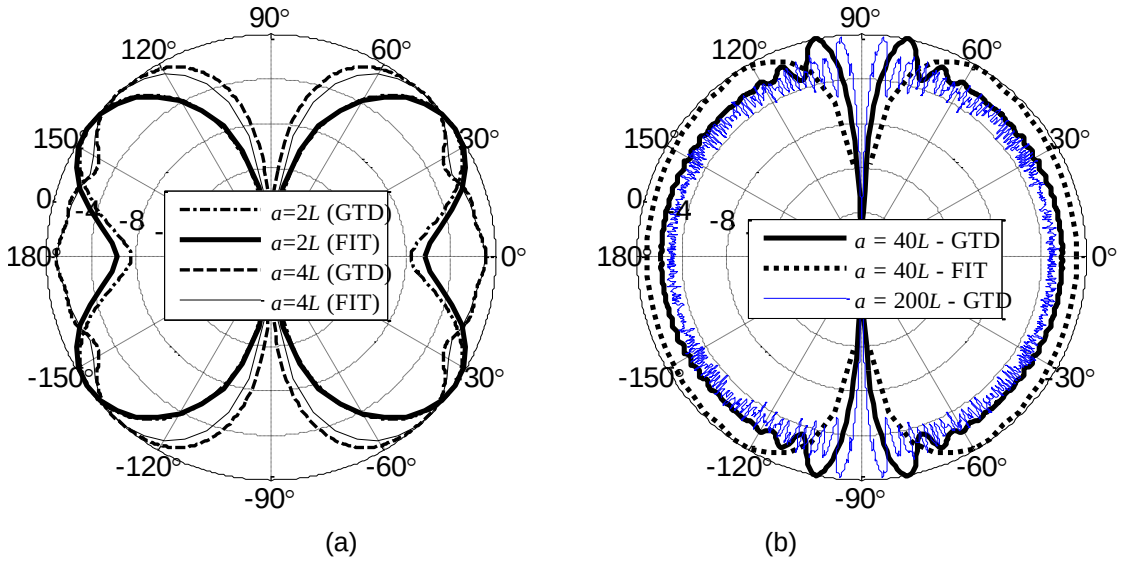

Figure 5.7 Comparison of slot patterns from GTD and FIT

$E\phi$ in x-y plane at L/λ=0.8 for slots in (a) smaller groundplanes and (b) larger groundplanes

Any confusion on this matter may stem from where the far field pattern is measured. For a large (but still finite) groundplane, the “far field of the antenna” may be interpreted as the far field of just the slot. In the far field of the slot, but on the groundplane, and well away from the groundplane edges, there are pattern maxima along the *y*-axis directions, as per the dipole equivalence. However, this is hemispheric radiation rather than a full sphere of radiation because we are only looking above the groundplane. Away from the edge of the finite groundplane (allowing a full sphere of radiation), the maximum of the far-field (of the groundplane) pattern along the y-axis becomes a null, independent of the finite groundplane size. We emphasize that the patterns discussed here are 3D patterns for the open slot on a finite groundplane, and the far-field must be interpreted as including the finite groundplane as part of the antenna.

As mentioned earlier, the simulation is not practical for a very large groundplane, owing to practical limits on program and computing resources. On the other hand, when the groundplane is very large and regular shaped, GTD is a better approach for the *x-y* pattern cut. The difference of these two approximations is more noticeable when the groundplane is larger, as can be seen in Fig. 5.7.

For a smaller groundplane, such as $a<1.2L$, the patterns have single lobes on each side of the groundplane, similar to the ones for $a=1.2L$ in Fig. 5.6, so they are not plotted here. This single-lobed shape remains even when the groundplane is much smaller and has become rectangular. Table 5.1 lists the simulated gain and radiation efficiency of the slot ($w=0.04\lambda$) in different groundplanes. The efficiency is almost unity (rounded to 2 decimal places), thus there is little energy dissipated in the groundplane, and the directivity is essentially the same as the gain. To offer one comparison of how the pattern changes, Fig. 5.8 summarizes the directivities (by simulation) of the slot in small rectangular (to the left of the 1.04 value) and larger square (to the right from the 1.04 to 20 values) groundplanes, for both resonance frequencies. When the groundplane is small, the directivity for the first resonance varies between 5.6dBi to 4.4dBi; at the second resonance, the directivity is higher (around 6.2 dBi) with a much smaller variance. Therefore, the slot in a very small groundplane at its second resonance retains a rather stable pattern in the face of a changing symmetric groundplane shape and size. When the groundplane is larger, the directivities fluctuate and generally reduce with the increase of the groundplane

size, but even for a 20λ×20λ groundplane. The directivities, at around 4.5dBi, are still well above that of the corresponding wire dipoles in free space.

Table 5.1 Simulated gain and efficiency of slot in varied groundplane (*w*=0.04*L*)

a / *L*		0.2	0.4	0.8	1.0	1.2	2	3	4	6	8	10	20
b / *L*		1.04	1.04	1.04	1.04	1.2	2	3	4	6	8	10	20
L/λ=0.5	Gain (dB)	5.7	5.3	4.5	4.5	4.8	5.9	5.6	5.8	5.0	4.5	4.5	4.8
	Efficiency	0.96	0.99	0.99	1.00	1.00	1.00	0.99	1.00	1.00	1.00	1.00	1.00
L/λ=0.8	Gain (dB)	6.4	6.2	6.1	6.1	6.4	6.0	5.8	4.7	5.9	5.1	5.4	4.2
	Efficiency	0.99	0.98	0.99	0.97	1.00	1.00	1.00	1.00	1.00	1.00	1.00	1.00

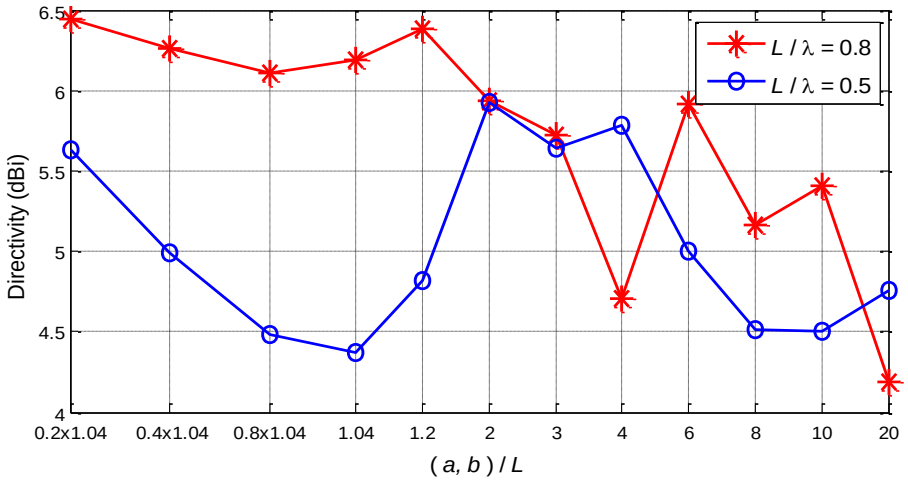

Figure 5.8 Directivity against the groundplane size

The groundplane size (x-axis) is a rectangle of a by b and these measurements are normalized by the slot length *L* on the x-axis. To the right of the groundplane value of b/*L*=1.04, the value a/*L*=b/*L*=1.04 is plotted, and the groundplane stays square to the right of this.

5.3.2 Asymmetric small groundplane in slot broadside direction

Here we discuss groundplane asymmetry in the *y* direction where the widths of the half groundplanes (a_L and a_R) at each side of the slot are different. The examples are a_L/a_R=0.39*L*/0.5*L*, 0.78*L*/0.5*L* and 1.13*L*/0.5*L*. We only look at the second resonance here since the slot at the first resonance is sensitive to the changes of the small groundplane.

As given in Table 5.2, the impedance remains near 40Ω despite the change of the ratio. However, the change of the directivity is more noticeable. This is expected since the diffraction contributions from the groundplane edges are asymmetric.

Table 5.2 Slots in asymmetric groundplanes at the second resonance

a_L / a_R	0.39*L*/0.5*L*	0.78*L*/0.5*L*	1.13*L*/0.5*L*
Impedance (Ω)	38+j0.3	40-j1.6	40-j2.8
Directivity (dBi)	6.3	5.9	5.2

From the above parametric study, we conclude that, for a given slot shape (*w*=0.04*L*, *L*=0.8λ), the groundplane size can be as small as about 1.04*L*×0.4*L* (0.83λ×0.32λ) in order to support the second resonance slot matched to 50Ω. The directivity is about 6.2 dBi when the slot is symmetric in the groundplane, which is more than 3dB higher than the dipole. There are pattern nulls along the groundplane direction at broadside to the slot. In particular, there is no null along the slot axis.

5.3.3 Impact of slot width

The impact of the slot width on the impedance bandwidth for the useful second resonance has not been previously addressed in literature. Such impact and the resulting quality factor are investigated. The slots are length L, and have widths w=0.2L, 0.1L, 0.05L, 0.04L, 0.01L and 0.005L, in the square groundplane (a=b=2L, d=0.01L). The change of the slot width has little influence on the pattern, so specific results for this are omitted.

Fig. 5.9 gives the simulated impedances against the slot electrical length. Over the range of 0.6≤L/λ ≤1, the curves of the resistance are rather flat but with different values, while the reactance crosses zero with different slopes, so the bandwidth for each slot width is expected to be different.

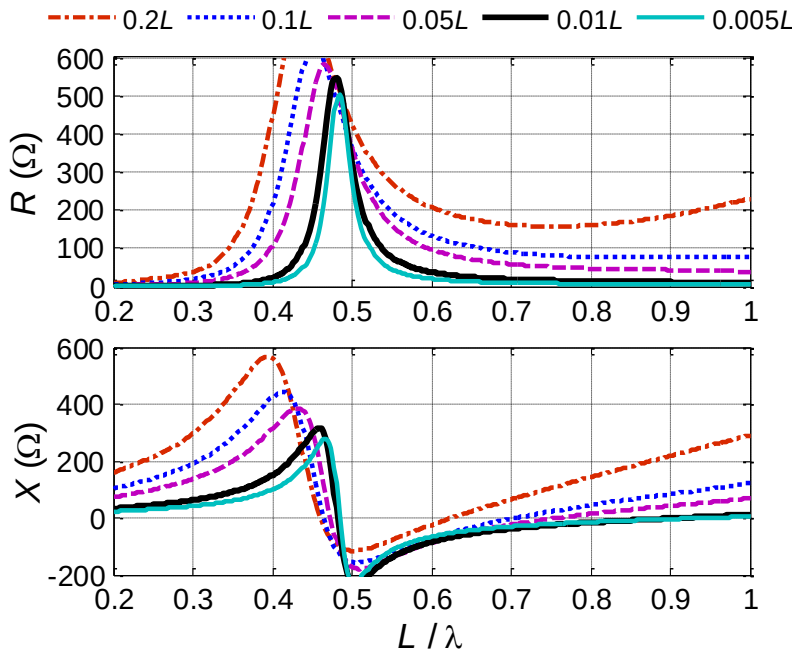

Figure 5.9 Simulated impedance over slot electric length for varied slot widths

The -10dB theoretical bandwidth (the available bandwidth at each frequency when the antenna is tuned with an idealized matching circuit, *cf*. [12][79]) is obtained from the quality factor, *Q,* as

$$Q = \frac{\omega}{2R}\left|\frac{\partial Z}{\partial \omega}\right| \tag{5-1}$$

$$BW_{\text{-10dB}} = \frac{2}{3}\frac{1}{Q} \tag{5-2}$$

Fig. 5.10 shows how the fractional -10dB impedance bandwidth increases with the slot width from 0.005*L* to 0.2*L* over the frequencies of interest. This bandwidth is reasonably constant over the central frequency range for a given slot width. Along these curves, the rectangular shape of the slot is constant but the electrical size is changing. So at the second resonance, the theoretical bandwidth is dependent on the shape of the slot rather than its electrical size.

Fig. 5.11 shows that the 50Ω impedance bandwidth is best when the slot width is 0.04*L* among these sample slot widths. Here the 10dB bandwidth (without matching circuit) is close to 25%. This is close to the theoretical bandwidth of 24% from Fig. 5.10.

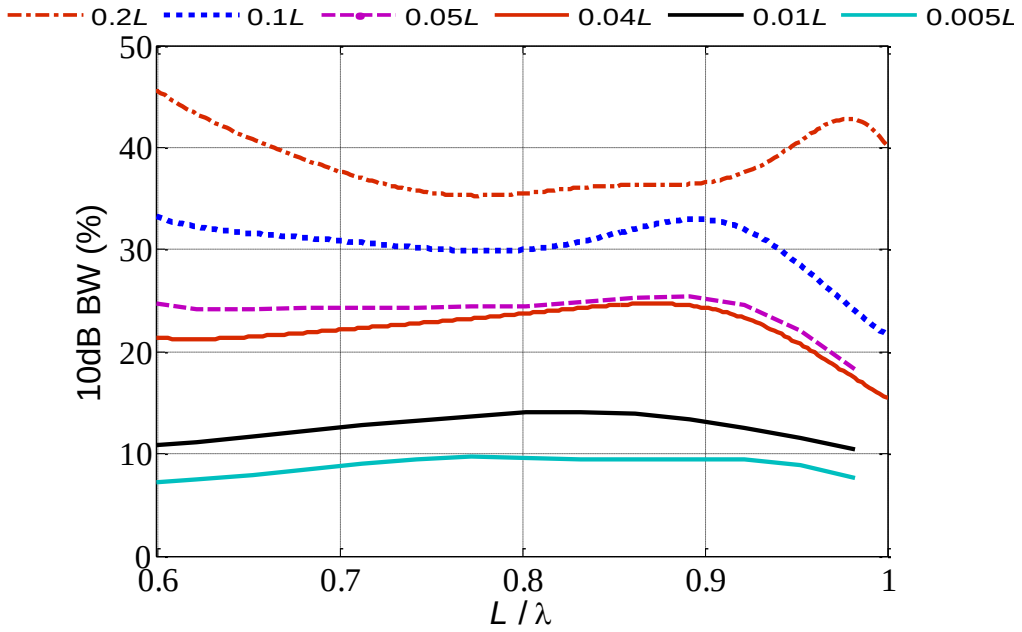

Figure 5.10 Bandwidth derived from *Q* over *L*/λ for varied slot widths

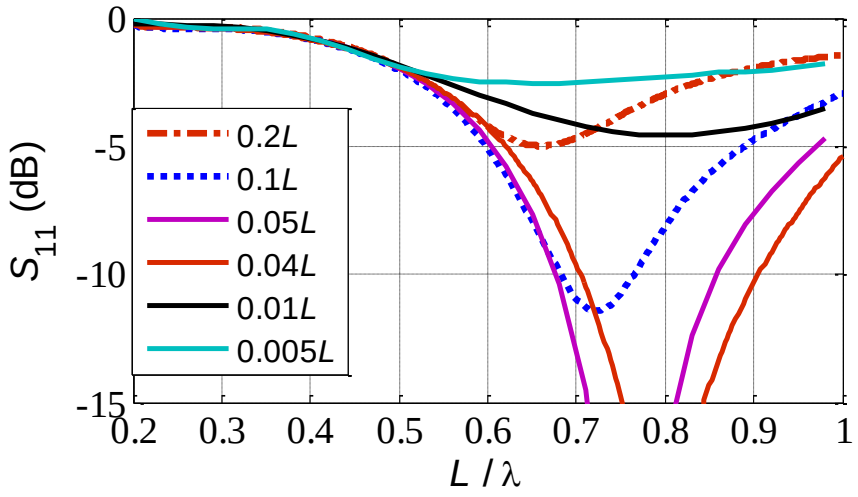

Figure 5.11 S_{11} over *L*/λ yields 50Ω impedance bandwidth.

5.3.4 Impact of slot depth

A slot antenna is often cut on a thin metallic sheet or etched from a circuit board, so the slot depth (which is also the groundplane depth) is usually very thin. To the author's knowledge, the impact of the slot depth on the antenna performance has not been treated in the literature. Such impact is investigated here by varying the depth of the groundplane from d=0.008L, 0.083L to 0.167L for the slot (w=0.06L) in the small groundplane (1.04L×0.4L). The far field radiation pattern includes single lobes on each side of the groundplane with a directivity of 6.2±0.1dBi for each slot depth from simulation.

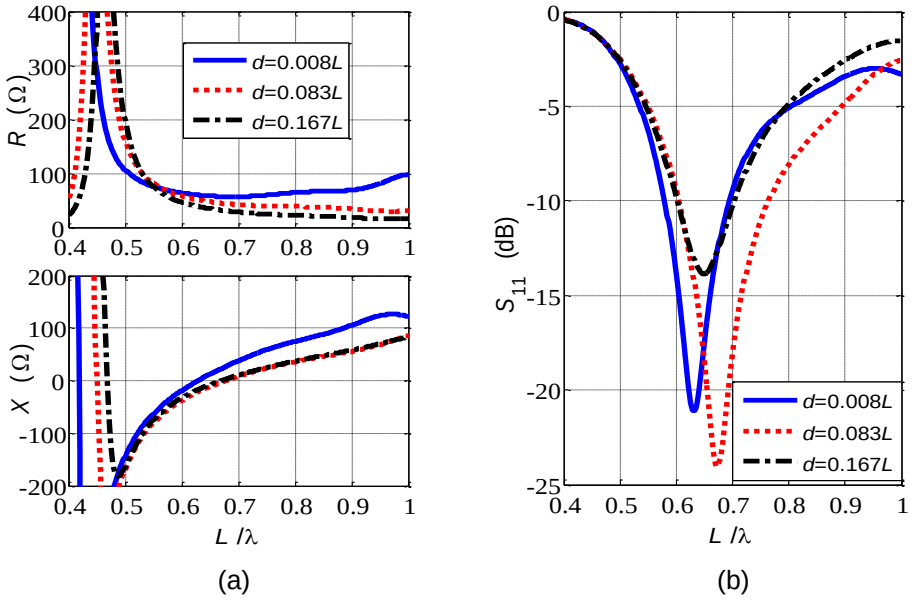

Figure 5.12 Impact of slot depth from simulation

(a) impedance and (b) reflection coefficient of slots with different depths

Fig. 5.12(a) shows the simulated impedance of the slot antenna against its electric length. The resistance remains near 50Ω at the second resonance when

the slot depth is 20 times deeper from 0.008*L* to 0.167*L*. The change of the reactance is more noticeable when the slot is thinner, which brings the slot second resonance to a lower frequency, as can be seen from the reflection coefficient given in Fig. 5.12(b). The 50 Ω impedance bandwidths are 18%, 23% and 17% for these three sample depths from shallow to deep, respectively.

5.4 Slot antenna in a bent small groundplane

In this section, the impact of a bent groundplane is considered through measurements and simulations. The slot antenna with *w*=0.04*L*, *a*=*b*=2*L* and *d*=0.01*L* is bent along the *z*-axis and becomes a slot-wedge, as in Fig. 5.13. The acute wedge angle between two halves of the groundplane is denoted as α. The dimensions of six such slot-wedge antennas are listed in Table 5.3.

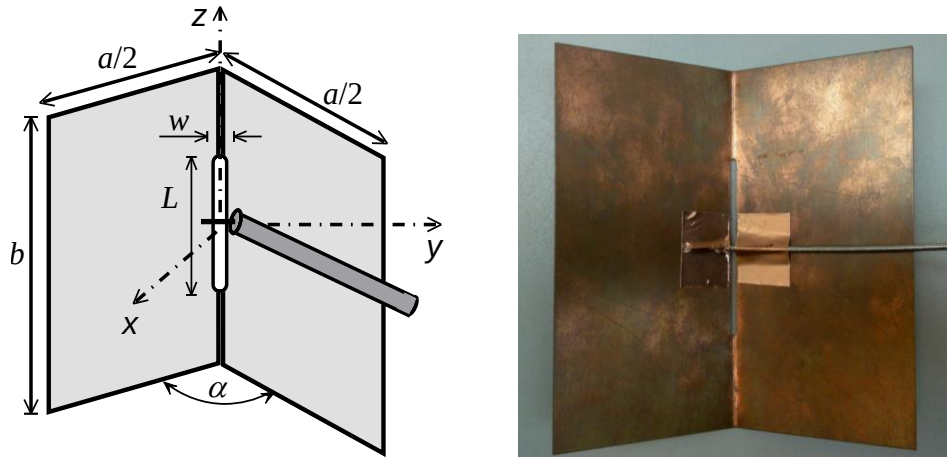

(a) (b)

Figure 5.13 Slot-wedge antenna

(a) Schematic and (b) photo with α=90^o as an example

5.4.1 Impedance of slot-wedge antenna

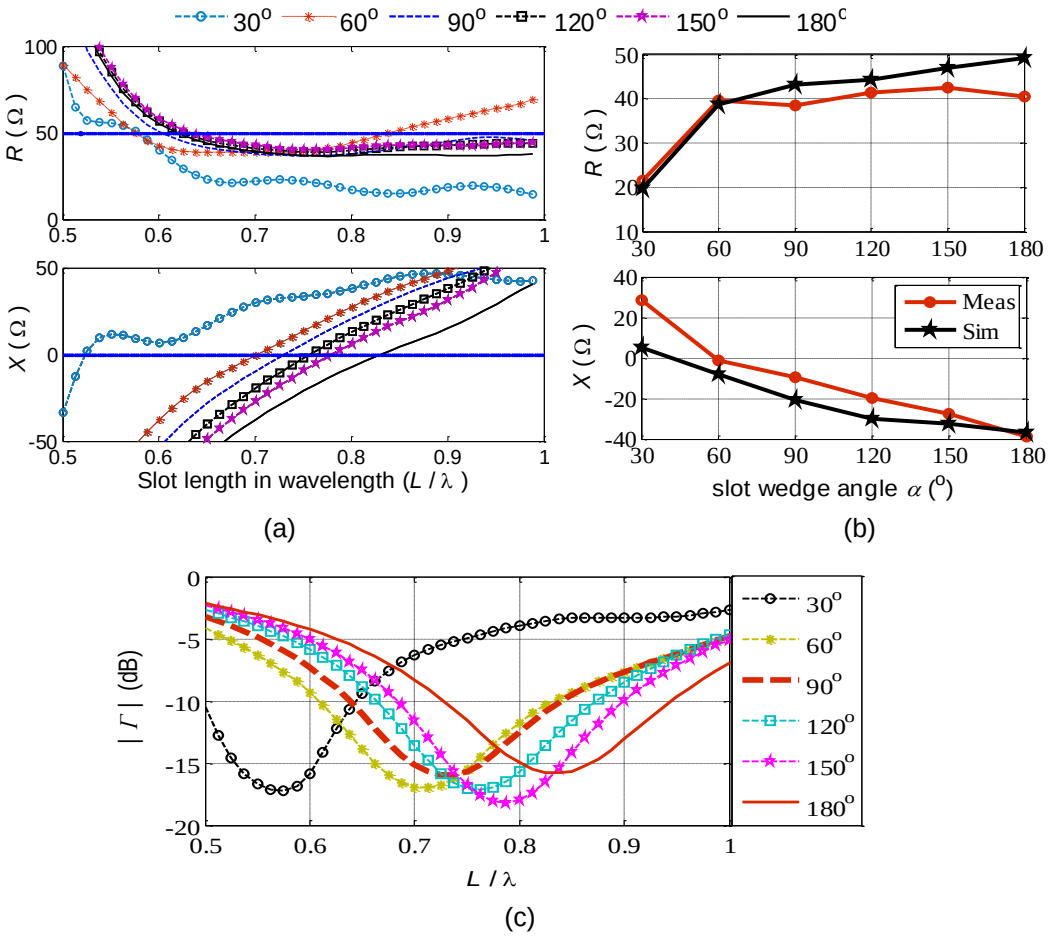

Figure 5.14 Impedance of slot-wedge antenna

(a) measured results; (b) measured results compared with simulation results at L/λ=0.7; and (c) magnitude of measured refection coefficients of the six slot-wedge antennas

The impedance versus slot length and wedge angle is given in Fig. 5.14(a). The second resonance remains in the range of L/λ=0.7 to 0.8, except for α=30° where the locus departs from the others. In Fig. 5.14(b), the impedance at L/λ=0.7 shows that the physical measurements agree reasonably well with the

simulations. Of practical interest is that the slot-wedge antennas remain well matched for a large range of bending angles. Fig. 5.14(c) gives the magnitude of the measured reflection coefficient against the slot electrical length and wedge angle. The corresponding 50Ω impedance bandwidth remains wide for a large range of the wedge angles. The -10dB relative (50Ω) bandwidth is between 31% and 27% as listed in Table 5.4, with a decreasing center frequency when the groundplane is bent from α=180^o to 30^o.

Table 5.3 Dimensions of six slot-wedge antennas

L	*w*	*a*	*b*	*D*	α
60mm	0.04*L*	2*L*	2*L*	0.01*L*	30^o, 60^o, 90^o, 120^o, 150^o, 180^o

Table 5.4 -10dB bandwidth of the slot-wedge antenna with varied wedge angles

α	30^o	60^o	90^o	120^o	150^o	180^o
BW	28 %	31 %	28 %	29 %	28 %	27 %

5.4.2 Patterns of slot-wedge antennas

The normalized E_φ for L/λ=0.7 are given in Figs. 5.15(a)-(d) from simulation, and in Figs. 5.15 (e)-(f) from physical measurement. Of particular interest from 5.15 (a) and 5.15 (b) is that, for this groundplane size, as α changes from 180° to 30°, the beamwidth first decreases, reaches a minimum at α=90°, and then increases again. Therefore, the maximum directivity, at least for the sample angles and groundplane size tested here, is when the wedge is a right angle.

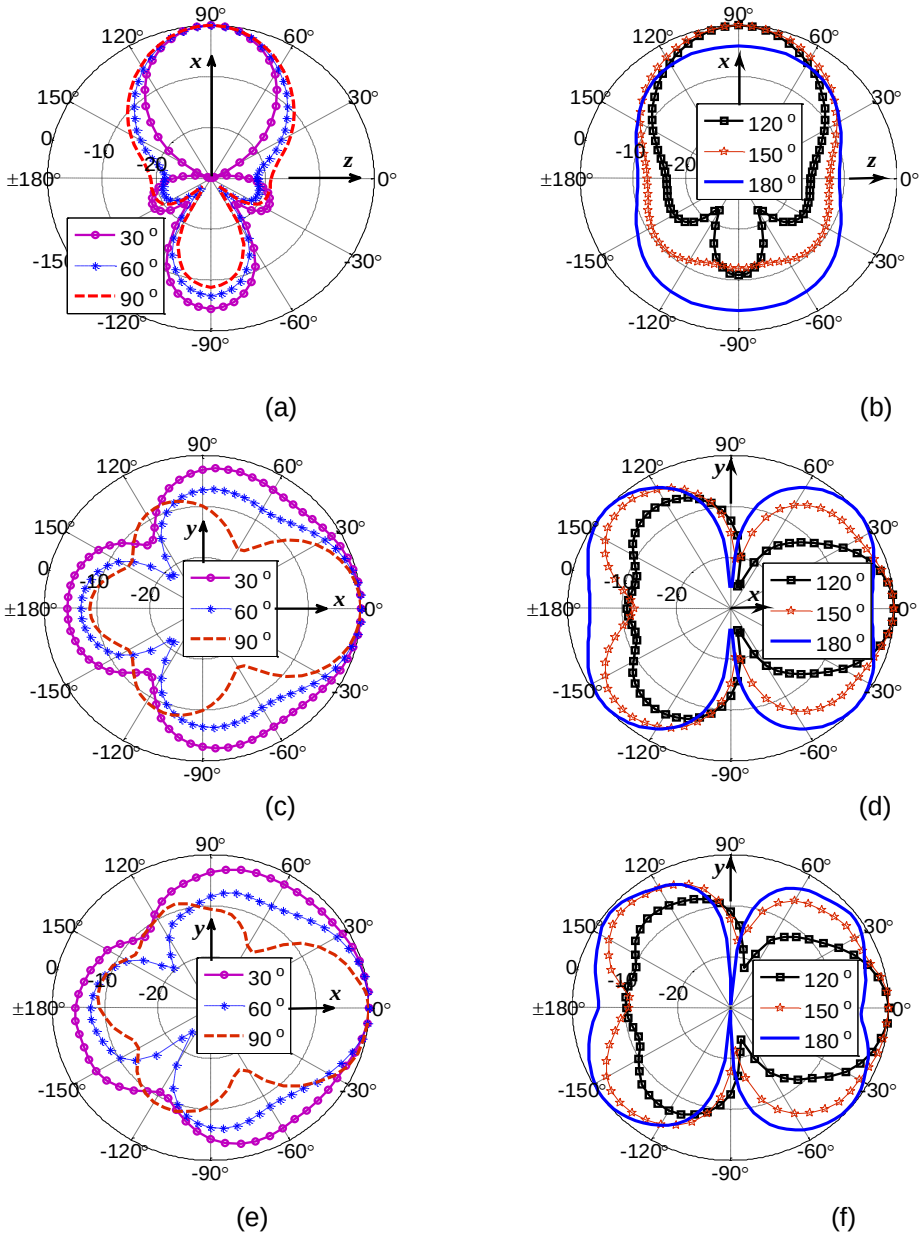

Figure 5.15 E_ϕ for L/λ=0.7

(a) and (b) in *x-z* plane (φ=0°), FIT simulations; (c) and (d) in *x-y* plane (θ=90°), FIT simulations; (e) and (f) in *x-y* plane, physical measurements; In (a) and (b), the wedge opening is in the x-axis direction.

The measured E_ϕ in the *x*-*y* plane shown in Figs. 5.15(e)-(f) agrees well with the simulated results in Figs. 5.15(c)-(d). As noted in Section 5.2, the maximum of the pattern is not along the *x*-axis at L/λ=0.7 for a flat groundplane. It can be seen from the results here that, by bending the groundplane, the maximum gain direction is forced forward and aligns with *x*-axis.

Directivities are plotted in Fig. 5.16 for comparison. Here, the directivities from measurement and simulation are in reasonable agreement (1dB worst case for α=30°). The differences between the two approaches include the presence of the feeding cable in the physical measurement configuration, which is not modelled in the simulation; and to a lesser extent, the contribution of missing pattern measurement data due to the support platform in the physical measurement.

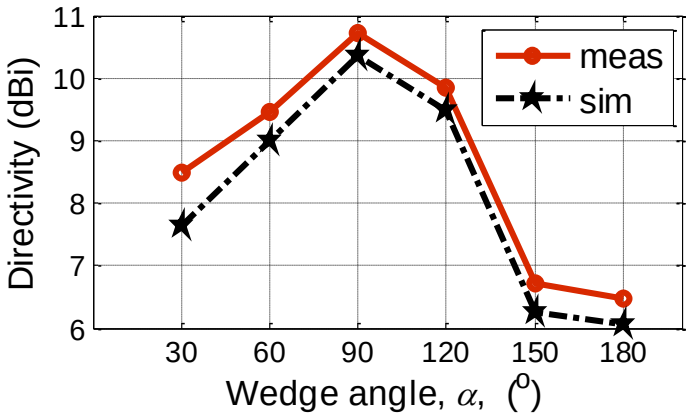

Figure 5.16 Directivities at L/λ=0.7 from measurement and simulation

Compared to a dipole, or a slot in an infinite groundplane, the directivity of the slot-wedge is firstly increased by about 3dB due to the finite, flat groundplane

diffraction, and then by another 4dB due to the bending of the groundplane into a right angle along the slot. A right-angled slot-wedge provides a simple, medium gain antenna with direct 50Ω matching to coaxial cable over a broad bandwidth. We have not formally optimized the configurations because the incremental performance would be small, and the optimization would have to be made for a numerical implementation (with its inherent inaccuracies, and its finite differences from a physical implementation), or else by iterative cut-and-try physical experimentation, and this would optimize only for a given physical feed configuration and given antenna-bearing platform arrangement.

5.5 Closely spaced orthogonal slot antennas

The correlation of parallel and echelon slot elements in the same groundplane can be found only approximately from the patterns of their complementary dipoles, e.g., [4][51], however, there are no simple formulas available for skew slots or dipoles, which are used for polarization diversity. Here we look at skew slots and their measurements [182].

We can conveniently build slots that are arranged at different angles and spacing, and accurately measure their impedance matrix. With the impedance approach in Section 2.2.4, Eq. (2-9), the correlation of slot elements is estimated. The same approach is also exploited in [183] for patch antenna applications, and is illustrated here for a pair of slots. The process of multiport measurement, calibration, reference plane setting, and matching are the usual building blocks for developing compact arrays. The measurement system and processing of data are described in detail in [182].

Fig. 5.17 shows two orthogonal, central-fed, narrow, half-wavelength slots placed in a thin rectangular ground plane. The frequency is 3GHz, so the length of the slot is *L*= 50mm. The slots are electrically narrow with a width of 2mm, in other words, the width is only 0.02% of the wavelength. The size of the groundplane is 400mm×400mm×1.7mm, which is sufficiently large to have very similar impedance to the slot in an infinite ground plane.

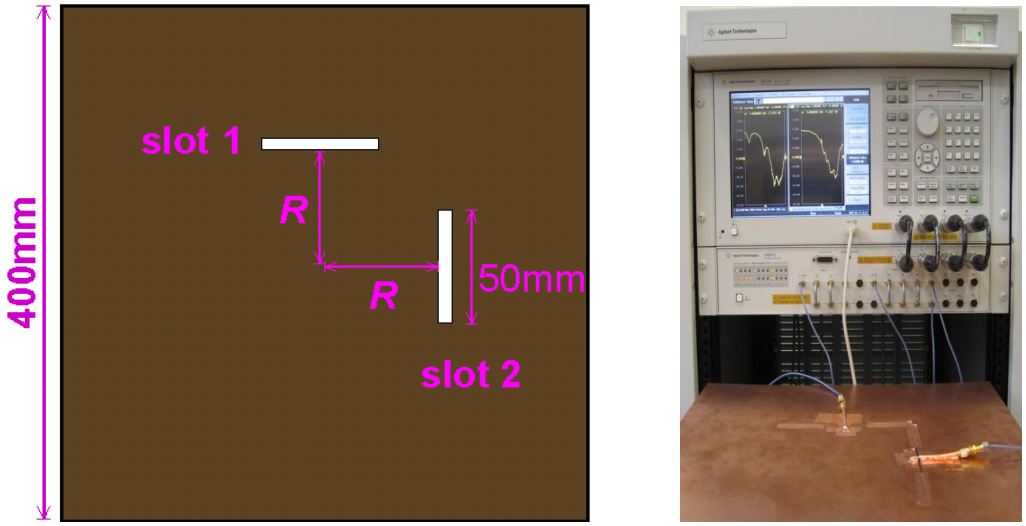

(a) (b)

Figure 5.17 Two orthogonal slots in different separations
(a) Schematic and (b) measurement setup

The coupling between the slots are of interest when the slots are moved away from an adjacent (intersecting slots) location, where *R* is slightly larger than 0.25λ to *R*=1.25λ. Despite the orthogonal polarizations, when the slots are close, there are non-radiating fields and current paths between the feeds of the slots, and as a result the closest slots are expected to have the largest mutual

coupling. As the separation of the slots increases, the coupling can be expected to drop quickly.

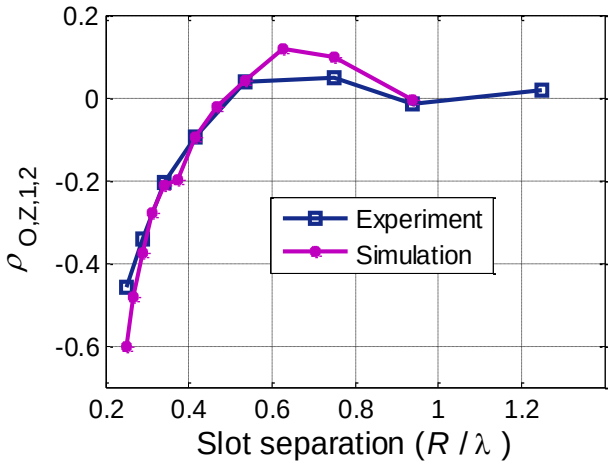

Figure 5.18 Normalized mutual resistances with different slot separations

In Fig. 5.18, the measured normalized mutual resistance, $\rho_{O,Z,1,2}$, at 3GHz is given with the change of the slot separation. The magnitude of $\rho_{O,Z,1,2}$ drops quickly from 0.6 to 0.1 when R/λ increases from 0.25 to 0.4. It shows the small increment of the separation of the orthogonal slots will significantly decrease the antenna correlation. The same observation can be seen from simulations implemented with Agilent ADS Momentum [177] given in Fig. 5.18. The same slots in the same finite ground plane were simulated in Momentum. The experimental results match the simulation results well.

5.6 Conclusion

The pattern of an open (i.e., double sided) slot in a finite groundplane cannot be accurately estimated from its complementary electrical dipole. In particular, the slot antenna pattern has a broadside null in the groundplane direction, whereas there is a maximum here for the dipole; and the slot antenna pattern does not have null along the axis of the slot, whereas there is a null for the dipole. The simulations and physical measurements demonstrate these differences, and the mechanisms for these effects are discussed.

New pattern and impedance results for the open slot antenna are presented from numerical and physical experiments. We include the impact of slot width, groundplane detail, and the angle of a bent groundplane. The physical and numerical experiments agree well, although in the narrowband region of the first resonance (a half wavelength - the traditional slot length of interest) the impedances from simulations do not correspond well with measurements. This is a typical phenomenon for narrowband antennas. However, we demonstrate that around the second resonance (slot length is about 0.8 wavelength) the agreement between the approaches is improved significantly and comprises a much wider band antenna than the ubiquitous half wavelength slot. There is a minimum groundplane size that allows the second resonance to have wide bandwidth for a given rectangular slot. Such a minimum is not so well-defined for the half wavelength slot, because the narrowband impedance changes quickly with small groundplane variations.

We show that the open slot with length of about 0.8λ in a small groundplane makes a simple wideband antenna with a medium gain. The theoretical bandwidth increases with the slot width, but for a 50Ω impedance bandwidth, a rectangular slot width of $w=0.04L=0.03\lambda$ is the best of the configurations tested here. The minimum groundplane size is about 0.16λ by 0.83λ for the given slot shape ($w=0.03\lambda$). The groundplane can also be bent along the slot axis, without reducing the bandwidth, to give some control over the antenna pattern and higher directivity. As an example, for a groundplane size of $(1.6\lambda)^2$ and a bending angle of 90^o, the directivity is about 10dBi.

These slot-wedge elements are feasible for MIMO antennas. The combination of four identical right-angled slot-wedge elements into a circular array forms a 4-element slot-wedge MEA [179][180], and to double, eight of such elements with wedge angle of 45^o are in a circular array to form an 8-element slot-wedge MEA [179]. Both MEAs allow slot sharing between different feeds with different patterns suitable for multi-beam scanning or angular space diversity for MIMO. For achieving 3-dimentional orthogonal beams, 12 identical right-angled slot-wedges can be on the edges of a hollow metallic cube [128][181]. This slot cube is an example of polyhedron slot-wedge MEA. These slot-wedge based MEAs provide good designs for many elements on given volumes, and they are feasible for the applications of base stations, Wi-Fi access points, and mobile terminals. These slot-wedge based MEAs will be introduced in detail in the next two chapters.

The study of the correlation between two closely spaced orthogonal slots in a common groundplane suggests that a small increment in separation between the orthogonal slots significantly decreases the antenna correlation for the use of antenna pattern diversity. The resulting relation of the estimated correlation over the slot spacing assists the design of slot-based MEAs in the later chapters.

CHAPTER 6: SLOT–WEDGE MEA

As explored in Chapter 5, a slot at its second resonance (strictly speaking, an impedance anti-resonance) makes a wide band antenna. The wide bandwidth is insensitive to the groundplane details including the size and shape, as long as the groundplane is large enough to support the current distribution for the second mode.

When the finite groundplane is bent along the slot, a slot-wedge antenna is formed. The radiation pattern changes with the bending angle while the bandwidth is retained. The combination of several slot-wedge elements into a circular array forms an MEA, which allows slot sharing between different feeds with different patterns suitable for multi-beam scanning or angular space diversity. The number of the beams and their coverage area depend on the number of the slot-wedge elements. Two array examples with 4 and 8 elements, respectively, are presented in this chapter.

6.1 Four-element slot-wedge MEA

As in the photo in Fig. 6.1(a), two flat groundplanes are joined at their centres to form a four element array. Each groundplane is $2L \times 2L$, where L is the length of the slot and its width is $w=0.04L$. The slot is cut centrally along the join of the groundplanes. The four right-angled slot-wedge elements are labelled as

w1 to w4. Each element is fed at the centre of the slot with a coaxial cable. The outer conductor of the cable is connected to the one side of the slot and the inner conductor is connected to the other side, Fig. 6.1(b).

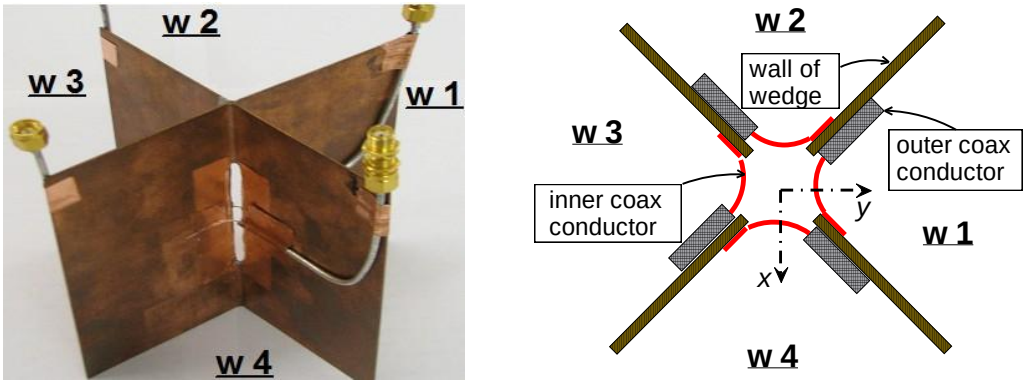

(a) (b)

Figure 6.1 4-element slot-wedge MEA

(a) Photo; (b) Plan view of the feeds in x-y plane cross section of the 4-element MEA

6.1.1 S-parameter and impedance matrices

Fig. 6.2(a) gives the magnitudes of the measured *S*-parameters against the slot electrical length, L/λ. The reflection coefficients, $S_{ii,\ i=1...4}$, (solid curves) yield an averaged -10dB relative bandwidth of 40% for the embedded MEA element at the centre frequency corresponding to $L/\lambda=0.7$. This frequency is near the slot second resonance. At the first resonance (below $L/\lambda=0.5$ and not shown here), the slot impedance is too high to match to 50Ω directly. The dash-dot curves are for the transmission coefficients, ($S_{ij,\ i\neq j}$), which indicate the mutual coupling between any elements. For this MEA, although the element slots are collocated, $|S_{ij}|$ are all below -8dB, so there is reasonably low mutual coupling

over the band of interest. Fig. 6.2(b) gives the simulated *S*-parameters and these are in good agreement with the measurements owing to the wideband nature of the structure.

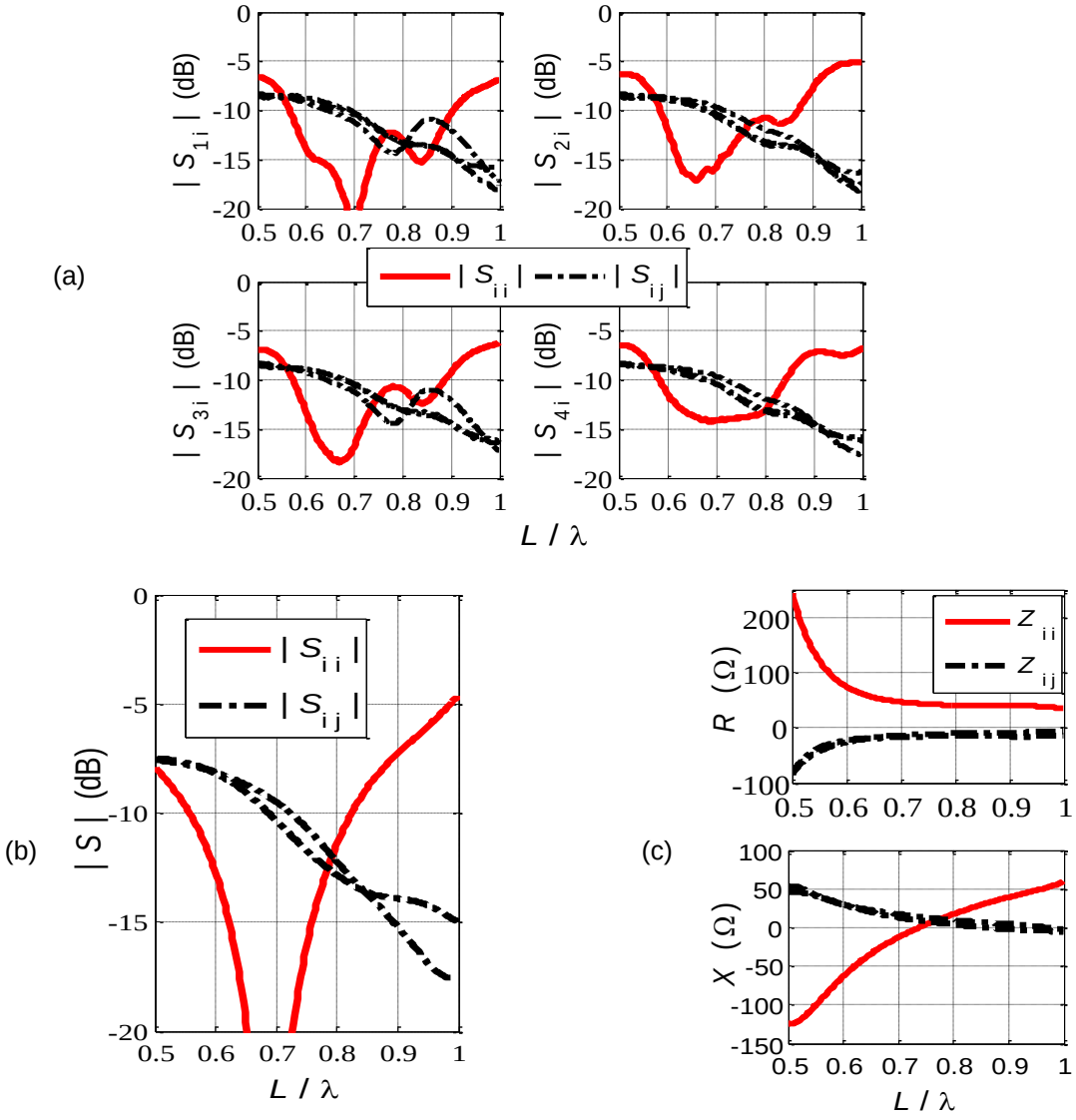

Figure 6.2 S-parameters and impedances of 4-element MEA

(a) S-parameters from measurement; (b) S-parameters from simulation; (c) simulated impedances

Fig. 6.2(c) gives the self impedances ($Z_{ii,\ i=1...4}$) and the mutual impedances ($Z_{ij,\ i\neq j}$). Within the -10dB bandwidth, the self resistances R_{ii} remain almost constant at 45Ω, and of particular interest, the absolute mutual resistances, $|R_{ij}|$, are less than |-10|Ω, i.e., the magnitude of maximum normalized mutual resistance is about |-0.22|, which offers insight into the impact of the coupling.

6.1.2 Embedded element patterns

The patterns of the embedded element includes open circuited or loaded patterns, defined with the transmitting element connected to the transmitter and other elements open circuited or load, respectively. Only the loaded embedded element patterns are given here.

For slots aligned with the *z* axis, E_φ is the dominant component, and E_θ is mainly below -20dBi so not given here. Fig. 6.3 gives the normalized E_φ pattern for the element w1 in the *x*-*y* and *y*-*z* planes, from both measurement (solid curve) and simulation (dash-dot). In Fig. 6.3(b), there is no measurement data available for a cone of about 30 degrees centred in the -*z* axis direction ($\theta = \pm 180^o$), owing to the platform to support the antenna in the pattern measurement chamber. These missing data are a cause for the difference between the measured and simulated gains and efficiencies, discussed below.

For the element w1, the maximum E_φ is in the *y*-axis direction, towards the opening direction of the wedge element. Towards the openings of the other wedge elements (-*y* axis and ±*x* axis direction), the pattern is 10dB lower. This is also indicative of low mutual coupling between wedge elements.

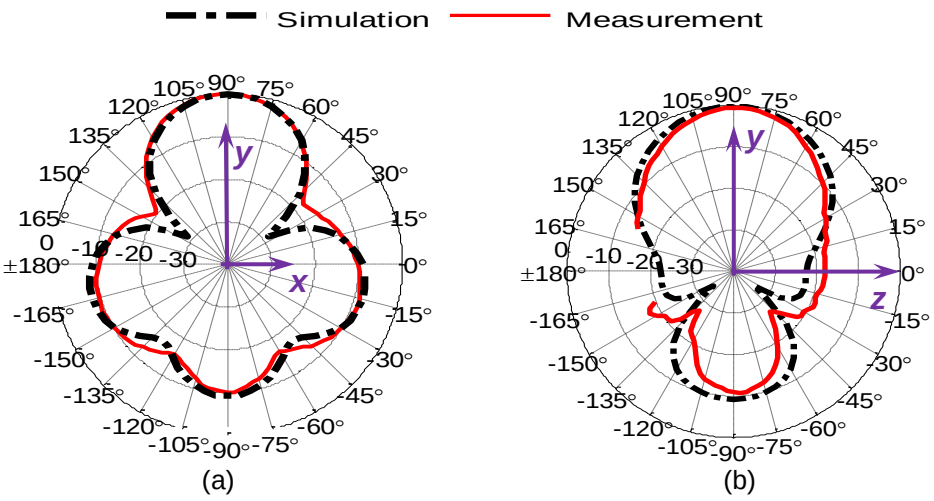

Figure 6.3 Normalized E_ϕ of element 1 in the 4-element MEA

(a) in *x*-*y* plane; and (b) in *y*-*z* plane for L/λ=0.7

Table 6.1 summarizes the embedded element gain, element total efficiency (η_{total} – includes ohmic loss, mutual coupling loss, and 50Ω impedance mismatch loss), front-to-back ratio (FBR) and 3dB beamwidth (BW) of the E_φ pattern in different planes. The measured and simulated element gains of the 4-element MEA are seen to be around 10dBi. The difference is probably caused by the missing measured data noted above. The total efficiencies are in good agreement between measurement and simulation. The loss is mainly from the mutual coupling between the elements. In the azimuthal plane (*x*-*y* plane), each slot-wedge element has a 3dB beamwidth of about 45 degrees.

A smaller version of the 4-element slot-wedge MEA, which has smaller groundplane size of 0.8λ×0.8λ, is simulated for comparison. The bandwidth of the small MEA retains wide. However, the element pattern gains reduce by about

3dB, but they are still considered high, compared to the gain of a dipole, for example.

Table 6.1 Gain, total efficiency, front-to-back ratio and beamwidth (*L*/λ=0.7)

	4-element MEA		4-element small MEA	8-element MEA		8-element small MEA
	Sim.	Meas.	Sim.	Sim.	Meas.	Sim.
Gain (dBi)	10.6	9.2	7.1	8.2	8.5	5.7
η_{total}	0.74	0.71	0.62	0.84	0.81	0.61
FBR (dB)	10	9.5	5.3	10	11	14
3dB BW in *x-y* plane ($\theta = 90^o$)	43^o	45.5^o	68.8^o	61.5^o	53.3^o	89.4^o
3dB BW in *y-z* plane ($\phi = 90^o$)	48.4^o	42^o	55.3^o	52^o	53^o	58.9^o

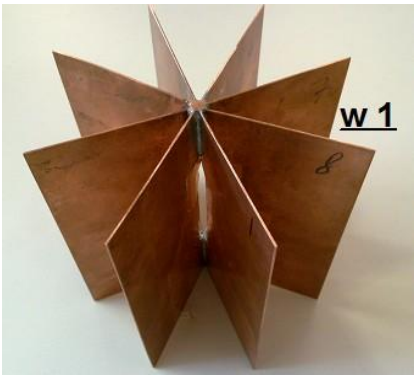

Figure 6.4 8-element slot-wedge MEA

6.2 Eight-element slot-wedge MEA

Fig. 6.4 is a photo of the 8-element MEA which combines eight slot-wedges with element wedge angle of 45^o. Each element is fed with coaxial cable in the same way as in Fig. 6.1(b), but the feeds are not included in the photo.

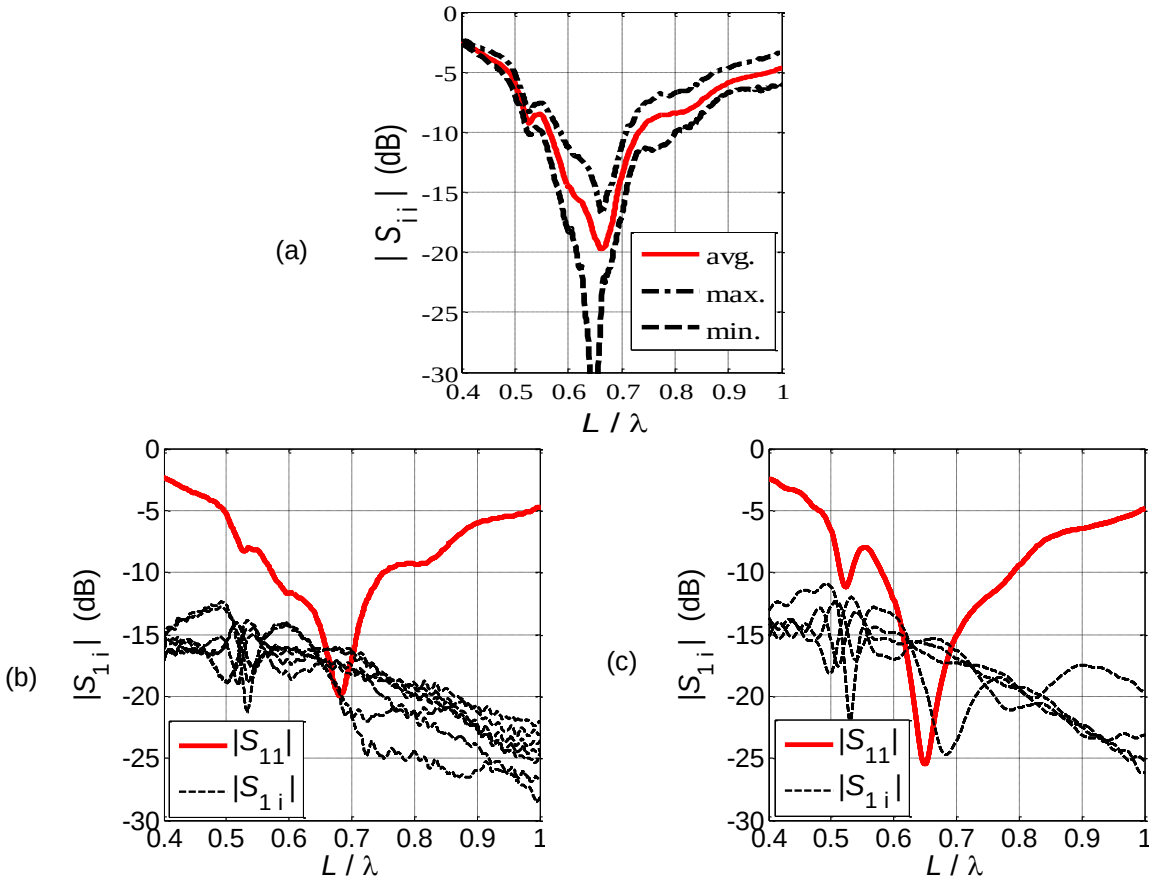

Figure 6.5 Measured S-parameter of wedge element 1 of the 8-element MEA

(a) Measured reflection coefficients of all 8 elements; *S*-parameters of Wedge 1 from (b) measurements and from (c) simulations

Fig. 6.5(a) summarizes the measured $|S_{ii,\ i=1\ldots8}|$. The variation of the measured data is indicated by the maximum (dash-dot) and minimum (dash-dash) of $|S_{ii}|$ over eight wedge elements. The average (solid curve) gives the mean of $|S_{ii}|$, which yields an average -10dB bandwidth of about 33%. The measured transmission coefficients $|S_{ij,i\neq j}|$ are all below -15dB so the mutual coupling appears lower than the one measured in 4 element array above. The simulated results are in good agreement with the measured results for all

elements, again because of the wideband nature of the structure, as can be seen in Figs. 6.5(b) and (c) for the measured and simulated *S*-parameters of the slot-wedge element 1.

Fig. 6.6 gives the normalized E_φ patterns from measurements and simulations. The element gain, efficiency, FBR and 3dB beamwidths are also given in Table 6.1. The element gain of the 8-element MEA appears to be lower than that of the 4-element array, thus the beamwidth is wider. In other words, the 3dB coverage in the azimuth plane is wider for the 8-element MEA and this is expected intuitively. The 10dB FBR remains at about -10dB. The element total efficiency is about 10% higher than for the 4-element MEA, and this is consistent with the lower mutual couplings of the 8-element MEA.

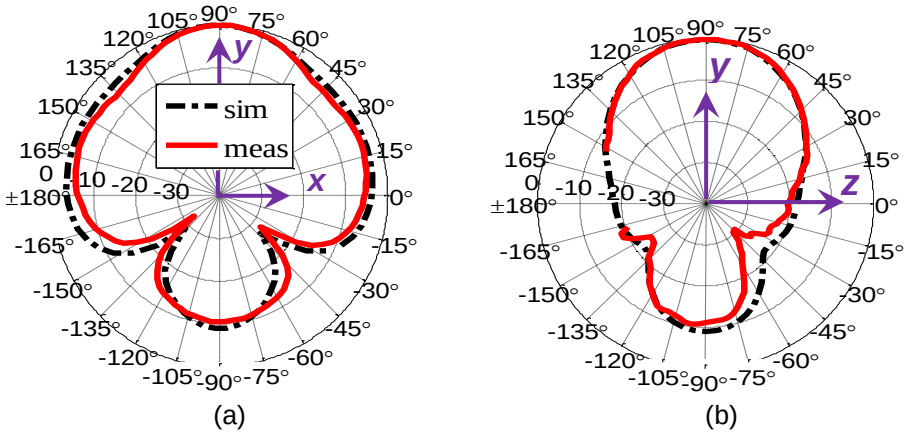

Figure 6.6 Pattern of wedge element 1 in the 8-element MEA

Normalized E_ϕ at L/λ=0.7 in (a) x-y plane and in (b) y-z plane

The slot-wedges used in these MEAs have large groundplanes of $2L\times2L$=1.4λ×1.4λ for high antenna element pattern gains (see Table 6.1). As

mentioned earlier, slot-wedge in smaller groundplanes remain wide bandwidth. However, the element pattern gains reduce by about 3dB, but they are still considered high, compared to dipole, for example. The pattern information and total efficiencies of the smaller MEAs (such as: $0.8\lambda \times 0.8\lambda$) are in Table 6.1. The sizes of the MEAs can be further reduced by fixing the height (the height of the wedge is limited by the slot length) and reducing the width, but the radii of the spheres inscribing the MEAs would not be changed.

6.3 Correlation matrix and approximations

As introduced in Section 2.2.4, The MEA correlations give the degree of similarity of the signals received by different antenna elements. This similarity degrades the MIMO performance, so the MEA correlation is desired to be as low as possible.

Several methods to estimate MEA correlation coefficient matrix have been introduced in Section 2.2.4, and they are summarized in Table 6.2. Only the embedded pattern approach is suitable for estimating the MEA correlation in various propagation scenarios. The impedance and scattering parameter approaches are derived for a uniform propagation scenario only. It is of interest to compare these three different approaches for the same MEA, so in the following discussion on the slot-wedge MEA correlation, only the uniform propagation environment is considered.

Table 6.2 MEA correlation coefficient estimation approaches

open circuit voltage correlation coefficient	$\rho_{o,z}$	Impedance approach	Eq. (2-9)
	$\rho_{o,H}$	embedded pattern approach	Eq. (2-8)
loaded circuit voltage correlation coefficient	$\rho_{L,z}$	Impedance approach	Eqs. (2-9) & (2-7)
	$\rho_{L,s}$	scattering parameters approach	Eq. (2-10)
	$\rho_{L,H}$	embedded pattern approach	Eq. (2-8)

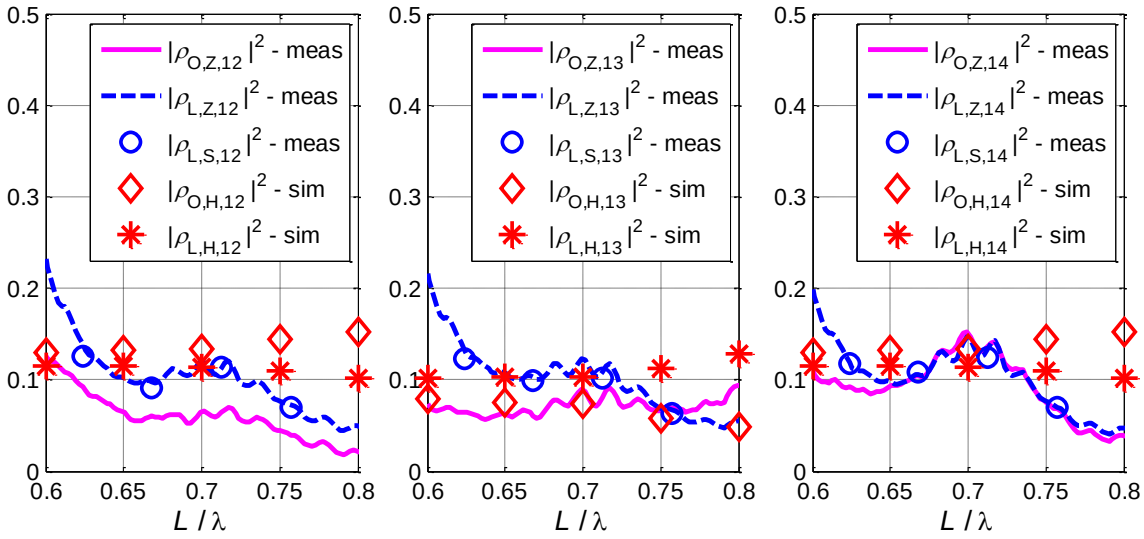

Figure 6.7 Estimated correlation coefficient matrix of the 4-element MEA

In Fig. 6.7 and 6.8, the estimated correlation coefficients are compared for each MEA, respectively. Taking the wedge 1 as the reference (see Fig. 6.1 and 6.4), the correlations between wedge 1 and other elements are plotted as the examples of the correlation matrices. $\rho_{o,z}$ and $\rho_{L,z}$, and $\rho_{L,s}$ are derived from the

measured impedance matrix and the *S*-parameter matrix, respectively, and they are compared with $\rho_{O,H}$ and $\rho_{L,H}$ from simulated patterns. As given in Figs. 6.3 and 6.6, the measured patterns agree well with simulated ones, so $\rho_{O,H}$ and $\rho_{L,H}$ from measurement are expected to agree well with the evaluations from simulation.

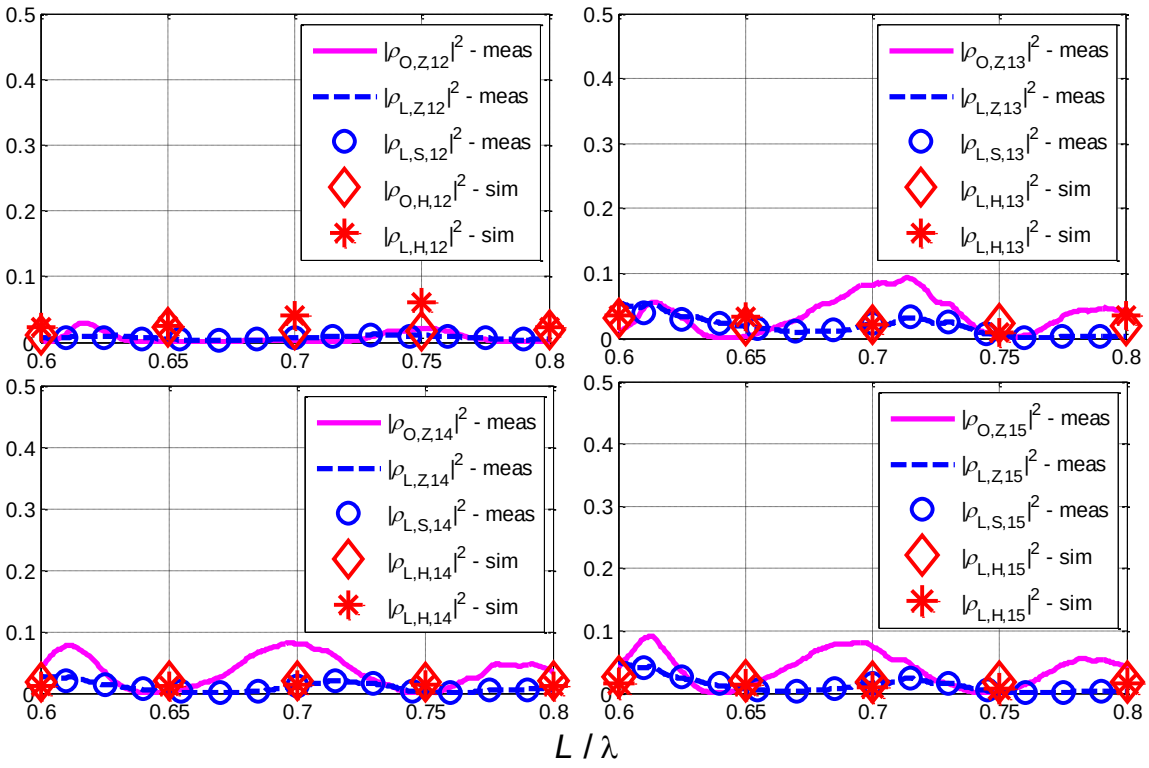

Figure 6.8 Estimated correlation coefficient matrix of the 8-element MEA

In Fig. 6.7 for the 4-element MEA, the estimated correlations between the wedges 1 and 2 are the same as the ones between the wedges 1 and 4, owing to the symmetric structure of the MEA. But they are slightly different to the ones between wedge 1 and 3. These differences are more evident in $\rho_{O,Z}$ and $\rho_{O,H}$. All

the estimated correlations are low with their magnitude square being lower than 0.2 over the frequency range of interest.

In Fig. 6.8 for the 8-element MEA, only the estimated correlations between the wedges 1 and 2 to 5 are given. The correlation between wedges 1 and 6 to 8 are the same to their symmetric ones. For this MEA, the estimated correlations are even lower (magnitude squares lower than 0.1), as expected from the lower mutual coupling in Figs. 6.5(b) and (c).

These experimental results in both Figs. 6.7 and 6.8 demonstrate that $\rho_{L,S}$ is equivalent to $\rho_{L,Z}$ since they are both derived with circuit methods, although with different approaches.

All the curves for the estimated correlations from measured data have similar magnitudes as those from simulated correlations. The differences are reasonable for the low values of the correlations. (Low correlations tend to be more difficult to estimate accurately.)

Here, the estimated correlations are only given in the range of $0.6 \leq L/\lambda \leq 0.8$, which overlaps with the -10dB impedance bandwidth. The correlation bandwidth is defined as the frequency range in which the correlation coefficient function is below certain value, e.g. 0.5. For these two MEAs, the correlation bandwidths are larger than the impedance bandwidths. So the MEAs are considered low-correlated within the -10dB impedance bandwidth.

The comparison of $\rho_{O,Z}$ and $\rho_{L,Z}$ demonstrates how the open circuit correlation contains different information from the loaded circuit voltage

correlation. $\rho_{O,Z}$ relates to the MEA itself, while $\rho_{L,Z}$ relates to the MEA with its terminations. For full-MIMO (eigen-MIMO) performance analysis, $\rho_{L,Z}$ is more useful since all the elements must be simultaneously terminated. For switched-type combining, only the selected element needs to be loaded, and the open circuit voltage correlation may be more useful. However, in practice, selection is often applied to the loaded signals.

As mentioned above, finite correlation decreases MIMO/diversity performance. The following section is to investigate the MIMO/diversity performances of these two MEAs, and how the efficiency and correlation impact their diversity performances.

6.4 Diversity performance

The measured total efficiencies are listed in Table 6.3 for open circuited (for non-simultaneous combining) and loaded (for simultaneous combining) MEA embedded elements, respectively. Since both MEAs have symmetric structures, the total efficiency is expected to be the same for each element, denoted as η_{total}. For each MEA, the efficiency for the loaded embedded element is lower than the efficiency for the open circuited ones, because there is more power lost to the loads of the elements, while open circuited elements are not terminated, so there is no power lost to the loads of other elements through mutual coupling.

The estimated correlation coefficient matrices, $\rho_{O,Z}$ and $\rho_{L,Z}$, from the measured data are used to estimate ρ_O (for non-simultaneous combining) and ρ_L (for simultaneous combining), respectively. They are scaled by the MEA total

efficiencies with Eq. (3-14), and then orthogonalized using singular value decomposition with Eq. (3-15).

Table 6.3 Measured embedded MEA total efficiency

	4-element MEA open circuited	4-element MEA loaded circuited	8-element MEA open circuited	8-element MEA loaded circuited
η_{total}	0.97	0.71	0.95	0.81

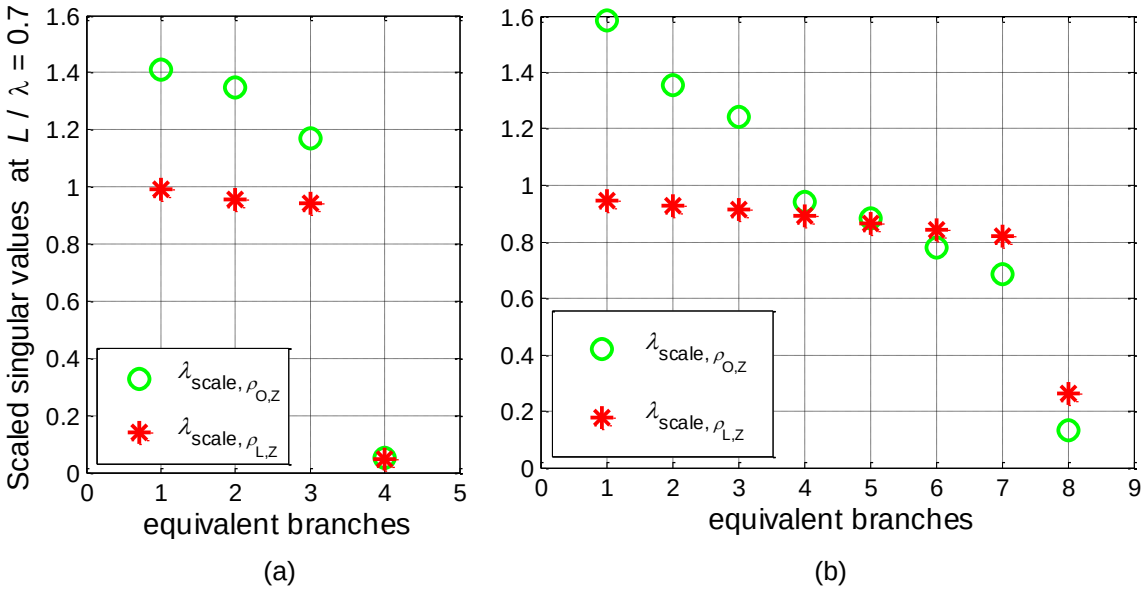

Figure 6.9 Scaled singular values at each equivalent branch of the MEAs

Singular values of the scaled ρ_O and ρ_L at L/λ=0.7 for (a) the 4-element and (b) the 8-element MEA

Fig. 6.9 gives the scaled singular values against the equivalent orthogonal branches for both MEAs at *L*/λ=0.7. The sums of the scaled singular values for

non-simultaneous combining are close to 4 and 8 for the two MEAs, respectively, which are the numbers of the elements of the MEAs. This is owing to the (almost) unity MEA total efficiencies for non-simultaneous combining. But for the case of simultaneous combining, the total efficiencies are significantly lower, so the sums of the scaled singular values are less than the numbers of elements of the MEAs.

Fig. 6.10 gives the *CDF* curves of the MRC combined *SNR* of the MEAs at L/λ=0.7, compared with idealized MEAs with 1 to 8 elements. MRC is simultaneous combining which gives the highest *SNR*. It is used as an example to demonstrate the diversity analysis here. The *CDF* of non-simultaneous combining is not given in Fig. 6.10. Including the impact of MEA total efficiency and correlation, the *CDFs* are found with the scaled singular values in Fig. 6.9 and with Eqs. (3-16).

The MRC *CDF* curves suggest that the loaded 4-element MEA is equivalent to a 3.3-branch ideally lossless and uncorrelated MEA (M_e=3.3), with a diversity gain of G_{div}=19dB for the probability of 0.5%. Likewise, the loaded 8-element MEA is equivalent to a 7-branch idealized MEA (M_e=7) with G_{div}=26dB for the same probability. Although both MEAs have low correlations, the mutual coupling causes loss in the loads of the elements, so the combined *SNR* is reduced, and the diversity order is reduced to M_e=3.3 and 7, respectively, as summarized in the following table.

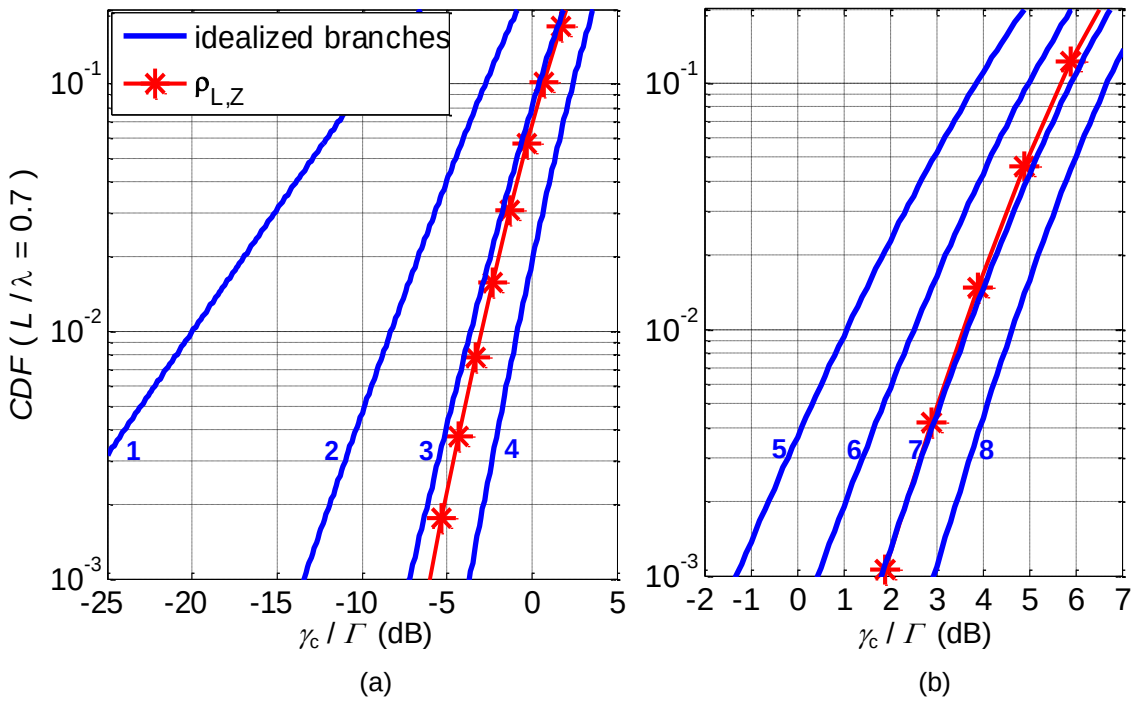

Figure 6.10 MRC *CDF* for diversity gain

(a) 4-element and (b) 8-element MEAs from measurement data

Table 6.4 Diversity performances of the slot-wedge MEAs

	Diversity order branches (M_e)	G_{div} (0.5%)
4-element MEA	3.3	19 (dB)
8-element MEA	7	26 (dB)

6.5 MIMO capacity

The impact of MEA correlation and efficiency on the MIMO capacity is discussed in Section 3.4. The Kronecker model provides the effective channel matrix, which includes the impact of the MEA at the receiver only (see Eq. (3-23)) or at both the transmitter and receiver (Eq. (3-21)), respectively.

In Fig. 6.11, the capacities of the simultaneous combined MEAs ($\rho_{L,Z}$ and loaded circuit η_{total} are used in the computation of the effective channel matrix) are given as in the following: the dash–dash curve is for the case when the 8-wedge MEA is at the receiver and an idealized 8-element MEA is at the transmitter; the dotted curve is for the case when the 8-wedge MEA is used at both ends; the dash-dot curve is when the 4-wedge MEA is used at the receiver only, and the transmitter uses an idealized 4-element MEA; the dash-circle is when the 4-wedge MEA is used at both ends; and the solid curves are for the idealized MIMO system in different orders from 1 to 8. The propagation scenario for all these MEAs is uniform and uncorrelated in both polarizations.

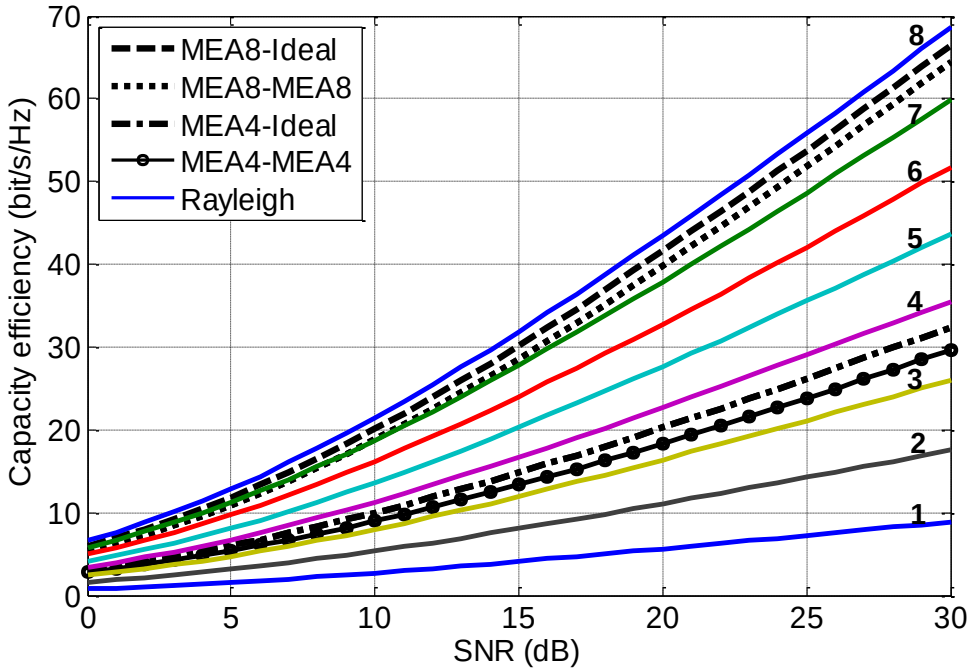

Figure 6.11 MIMO capacities of different systems

Both the correlations and the losses of the MEAs decrease their MIMO capacity performances. At a given *SNR*, e.g., 20dB, the 8-element MEA used at both ends of the communication link provide a capacity equivalent to an M_e=7.5 -order idealized MIMO system, and the 4-element MEA at both ends of the link provides a MIMO capacity order of M_e=3.3.

6.6 Compactness and space efficiency

The evaluation of the compactness of these MEAs follows the method discussed in Chapter 4. The space efficiency is the basic metric of this method. First we need to find the radiation quality factors, Q_{rad}, and the effective element electrical radii, ka_e, of the MEAs.

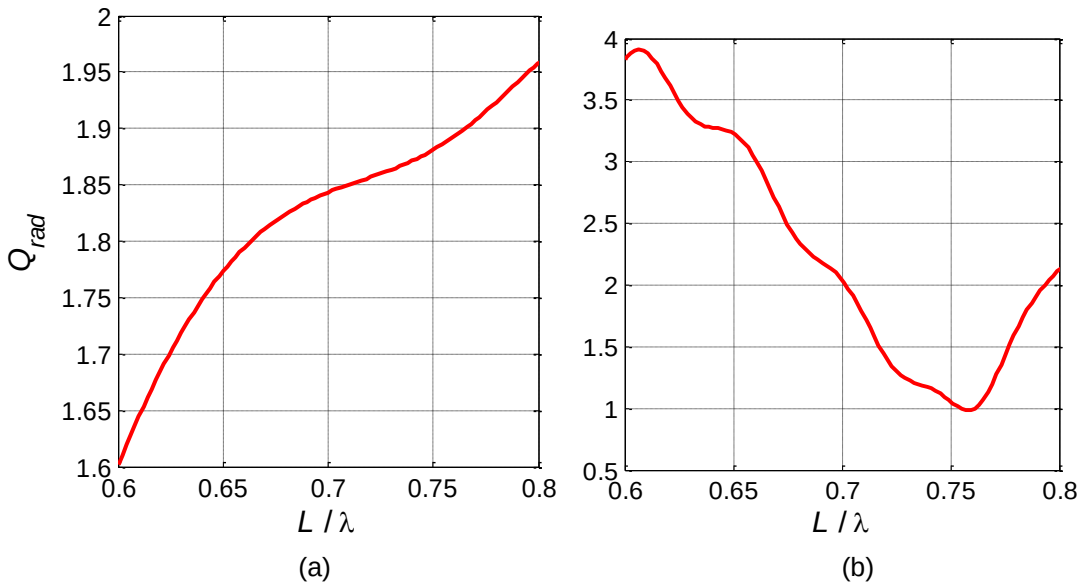

Figure 6.12 Q_{rad} derived from simulated element input impedance

(a) 4-element MEA and (b) 8-element MEA

Fig. 6.12 gives Q_{rad} of the MEA embedded elements over their electrical lengths near the resonances. As introduced in Chapter 4, Q_{rad} of an MEA embedded element is derived from its embedded input impedance with Eqs. (4-8) and (4-10). It is emphasized that the MEA embedded element is referred to as either the open circuited or loaded embedded element. Here the embedded input impedances are from simulations of the loaded MEAs.

In Table 6.5, the values of Q_{rad} at L/λ=0.7 from Fig. 6.12 are listed for both MEAs. Since the radiation efficiencies of the MEAs are near unity, the unloaded quality factors, Q, are the same as Q_{rad}. With the well accepted relation in Eq. (5-2), the fractional impedance bandwidth obtained from Q is close to the 50Ω impedance bandwidth, obtained from the reflection coefficient, as listed in Table 6.5 for both MEAs respectively.

Table 6.5 Quality factors and bandwidths of slot-wedge MEAs at L/λ=0.7

	Q_{rad}	η_{rad}	Q	-10dB BW from Q	-10dB 50Ω BW from $S_{i,i}$
4-element MEA	1.84	~1	1.84	36%	40%
8-element MEA	2.03	~1	2.03	33%	33%

Table 6.6 Compactness evaluation of the MEAs

	Q_{rad}	M_e	ka_{Chu}	ka_e	η_{space}
4-element MEA	1.84	3.3	1.04	4.18	0.25
8-element MEA	2.0	7.5	1.00	3.18	0.31

The effective element electrical radius of the MEAs is

$$ka_e = \frac{2\pi}{\lambda}\frac{a}{\sqrt[3]{M_e}}, \qquad \text{where, } a = L = 0.7\lambda \tag{6-1}$$

Values are listed in Table 6.6, together with Q_{rad}, ka_{Chu}, and with the resulting and η_{space}.

Fig. 6.13 compares the radiation quality factors and effective element electrical radii of the slot-wedge MEAs with the reference dipole arrays discussed in Chapter 4.

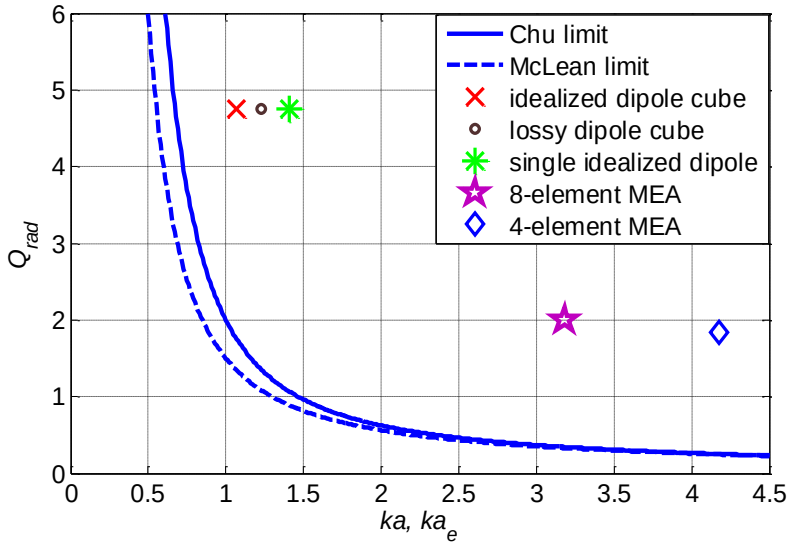

Figure 6.13 Q_{rad} against ka, ka_e of dipole arrays and slot-wedge MEAs

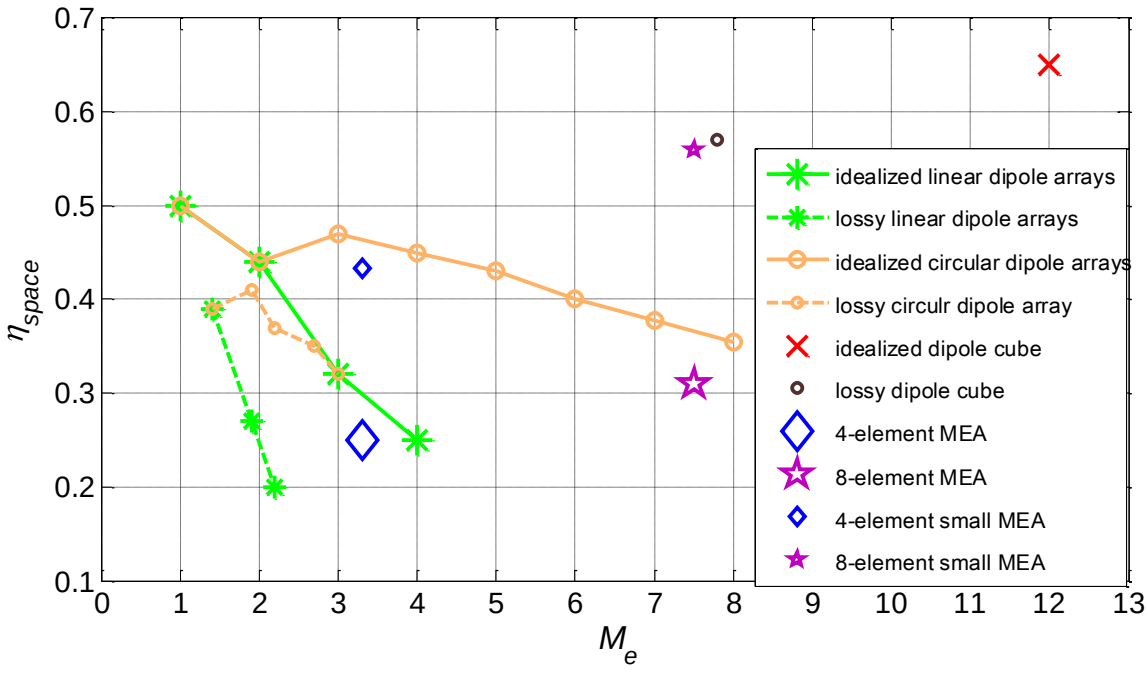

Figure 6.14 η_{space} of dipole arrays and slot-wedge MEAs against M_e

In Fig. 6.14, this observation is confirmed with the space efficiencies of the MEAs. The top right corner direction in the figure is where the antenna has a larger effective number of elements and higher space efficiency. The large star with the coordinates of M_e=7.5 and η_{space}=0.31 corresponding to the 8-element MEA is closer to the top right corner than the large diamond (M_e=3.3 and η_{space}=0.25) corresponding to the 4-element MEA.

In terms of space efficiency, the 4-element MEA is equivalent to a 4-element linear idealized dipole array, but it is much worse than a 4-element circular idealized dipole array. The 8-element MEA also has a lower space efficiency, η_{space}, than an idealized circular dipole array with the same number of

elements. Therefore, these realized slot-wedge MEAs have little space efficiency improvement over the idealized dipole arrays, and this is because of the low but finite correlation and non-unity efficiency. But it provides wider bandwidth and higher element gain. Smaller versions of the slot-wedge MEAs with the groundplane sizes reduced from 1.4λx1.4λ to 0.8λx0.8λ have significantly increased space efficiencies, as shown in Fig. 6.14 with the small star and small diamond for the two MEAs respectively, however antenna gains are reduced by about 3dB as summarized in Table 6.1.

6.7 Conclusion

The pattern of the single slot-wedge antenna changes with the wedge angle, but its impedance bandwidth remains wide. A right-angled slot-wedge antenna provides medium gain (~10dBi), low loss, and direct 50Ω match to coaxial cable.

Four right-angled elements in a circular array can share the slot with different feeds, providing multiple beams in the azimuth plane. Such an MEA is feasible for sectored beam scanning or angle diversity for a circular field of view. An eight element version is also presented for denser coverage.

The results for two such MEAs are presented. From both the simulated and measured data, there is reasonably low mutual coupling caused by the co-located feeds at the slots. The MEAs retain their match to 50Ω at each port, and their wide bandwidths around the second resonance. The MEAs have embedded element medium gains in the wedge element opening directions, with wide

azimuth coverage in each beam. The front-to-back ratio of each beam remains at about -10dB.

From the low mutual couplings between any two elements, the MEA correlations are low as well. However, since the antennas have multiple elements, the total power lost to the loads of the elements through mutual coupling is still considerable, so the total efficiencies of the MEA element are impacted by the low but finite mutual coupling.

Because of the finite correlations and the non-unity total efficiency, the diversity orders and MIMO capacity orders are less than the number of the elements. The compactness of the MEAs is not improved, and their space efficiencies are indeed lower than the reference idealized first resonance dipole circular arrays with the same numbers of elements. But these MEAs provide higher pattern gains and wider bandwidths than the dipole arrays. Smaller versions (smaller goundplanes) of the slot-wedge MEAs have significant space efficiency improvement, but with about 3dB reduction in maximum gain.

Finally a note of the decorrelation mechanism is in order. Although the slot-wedge antenna is derived from slot element considerations, *viz*., shared slots between elements, the MEA can also be viewed as elements comprising non-shared currents on the surfaces of the different wedges.

CHAPTER 7: SLOT POLYHEDRON MEA

In Chapter 6, slot based wedge MEAs are realized in circular arrays. Slot elements could also be placed on both the faces and the edges of polyhedrons to realize broadband MEAs. In this chapter, cube versions are presented with 12 slots on the edges of a hollow volume [128] and on a partitioned volume. Slots are along the edges of cubes and centrally fed for good match to 50Ω at the second resonance.

7.1 Slot polyhedron MEA

Any conductively enclosed volume in the shape of a polyhedron can be used to support slots on its faces and edges of its exterior (or shell). Symmetric regular polyhedra are of interest since they provide identical faces and edges. Examples are given in Fig. 7.1, including tetrahedron, hexahedron (cube), octahedron, icosahedron, etc. A specific example that is developed and measured in this dissertation is a cube, which has 6 identical faces and 12 identical edges, and so can support 12 slots on the edges, without resorting to placing slots in the flat faces of the cube.

Another example is Archimedean solids, which are highly symmetric, semi-regular convex polyhedrons composed of two or more types of regular polygons meeting in identical vertices, *cf*. [186]. There are 13 Archimedean solids

defined for different numbers of faces and edges. One example in Fig. 7.2 provides 92 faces and 150 identical edges.

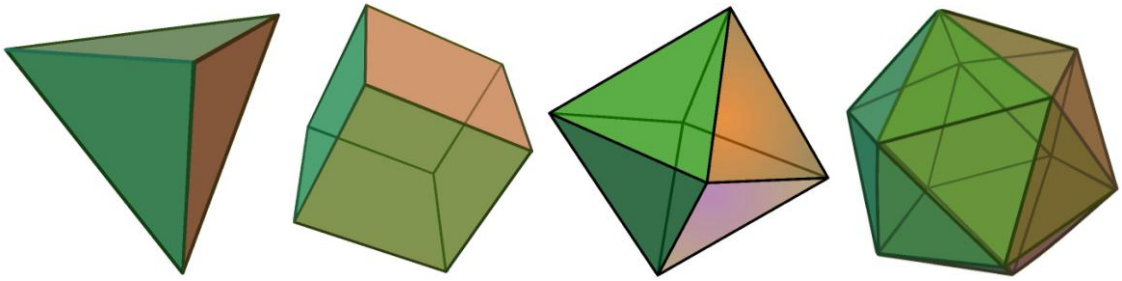

Figure 7.1 Examples of symmetric polyhedra

(a) tetrahedron; (b) cube or hexahedron; (c) octahedron; (d) icosahedrons from [185]

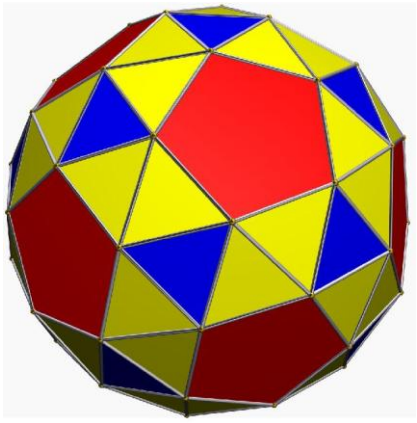

Figure 7.2 An example of Archimedean solid with 92 faces and 150 edges

Besides the numerous choices in shape, slot polyhedron MEAs can also have many different variations and extensions. Some examples are as follows.

1) A slot MEA can be sectored for providing partial coverage, rather than full spherical coverage. For example, a slot MEA on a hemispherically truncated polyhedron placed on a horizontal ground could provide antenna patterns covering the upper hemisphere only.

2) Slots of different lengths can be placed in the edge positions. This arrangement could allow different radio frequency bands to be integrated into the same MEA structure.

3) Slots can also be placed in the surfaces (faces) between the edges.

4) The idea of slot polyhedron MEA can also extend to designs comprising spaced slots on a curved volume such as a sphere. An advantage of the polyhedron shape is that it lends itself to building a shell from flat plates. Spherical and other double curved surfaces are difficult to manufacture in general.

7.2 Hollow slot MEA

The wire dipole structure comprising 12 dipoles at the edges of a cube shape is proposed in [49] and evaluated using idealized assumptions in Chapter 4. A slot cube is a more easily realized antenna than the dipole cube. There are other metallic cube MEAs, e.g., [43]-[45], and an open structure with multiple slots [44], but these all use the first resonance (half wavelength slot) which does not provide wide bandwidth.

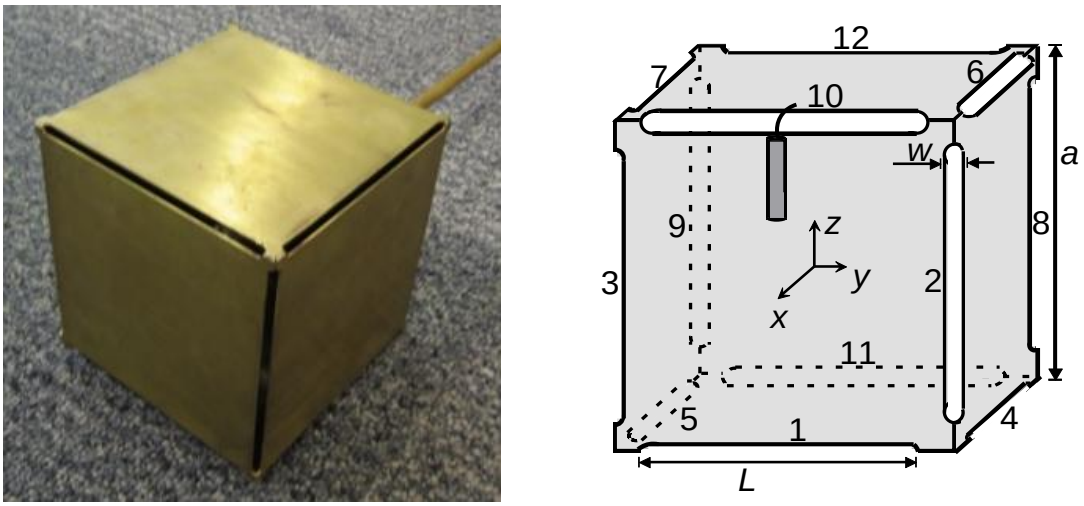

Figure 7.3 Slot cubes

(a) Photo and (b) schematic of the hollow cube

Fig. 7.3 gives the photo and schematic of the hollow cube. The cube edge is a=132mm long and the metallic walls are 0.8mm thick. Each edge of the cube is cut with a slot of L=120mm long and w=0.02L wide. The frequency range is 1GHz to 2.5GHz, so the corresponding slot electric length, L/λ, is from 0.4 to 1. These slots are centrally-fed with 50Ω coaxial cables, with the outer conductor of the cable fixed flush to one side of the slot and the inner conductor fixed to the other side of the slot, as one example drawn in Fig. 7.3(b). In Fig. 7.3(a), no feed cables are included.

The slots are numbered as in Fig. 7.3(b). For later study of the mutual coupling between the slot elements, slot 1 is taken as a reference element. Other

slots are grouped based on their relative geometry relation to this reference slot. Table 7.1 explains the grouping.

Table 7.1 Grouping slots 2 to slot 12 with slot 1 as reference

Group 1	slot 2, 3, 4, 5	orthogonal and adjacent to slot 1
Group 2	slot 6, 7, 8, 9	orthogonal but not adjacent to slot 1
Group 3	slot 10, 11	parallel to and share a common cube wall with slot 1
Group 4	slot 12	parallel to slot 1 and diagonally opposite

7.2.1 S-parameters and impedances of the hollow cube

Fig. 7.4(a) compares the magnitudes of the measured and simulated reflection coefficients of the slot elements, $|S_{i,i,\ i=1\ldots12}|$, against L/λ. In simulation, $|S_{i,i}|$ for all slots are the same, as given in the solid curve. But the measured $|S_{i,i}|$ are not identical owing to measurement errors and imperfect prototype implementation. To quantify this variation, Fig. 7.4(a) gives the maximum and minimum of the measured $|S_{i,i}|$ from all 12 slots, and the average is given by the dashed curve. In this way, the bounds of the measurements are clear to read. The figure also demonstrates the differences between the simulation and measurement, but this is mainly when $|S_{i,i}|$<-10dB. The 50Ω -10dB impedance bandwidth is about 30% cantered at the second resonance, L/λ=0.7 (f=1.75GHz).

Fig. 7.4(b) gives the averaged measured $|S_{i,1}|$ (dashed curve), which indicates the mutual couplings from slot 1 to any other slots. In the frequency range of interest, the $|S_{i,1}|$ are below -10dB, except $|S_{12,\ 1}|$ (diagonally opposite slots) whose peak is -7dB. The agreement between the measured and the

simulated results (solid curve) confirms that this MEA has reasonably low mutual coupling. The highest coupling is between the diagonal slots, and this can be expected from the element behaviour explained in Chapter 5 and in [180].

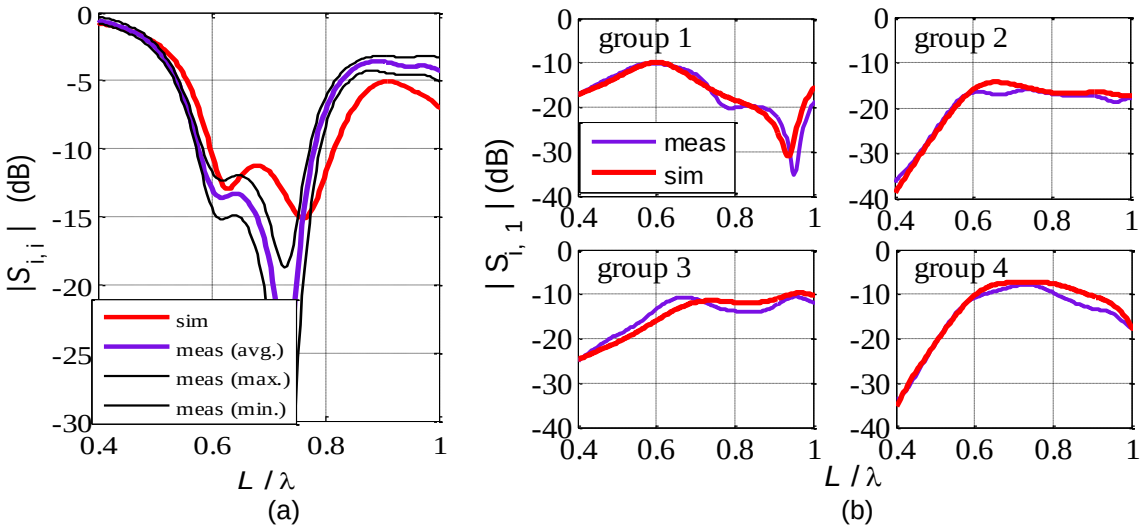

Figure 7.4 S-parameters of the hollow slot cube

(a) Reflection coefficients; and (b) transmission coefficients

7.2.2 Element far field patterns of the hollow slot cube

All slot elements are identical and element-symmetric to the cube, so their embedded element patterns are expected to be the same, but in different orientation. The element-symmetric term is defined in section 2.2.5. Fig. 7.5(a) gives the 3-dimention simulated pattern of the slot 1, and Fig. 7.5(b)-(d) are for the normalized patterns in two example cuts from simulation and measurement.

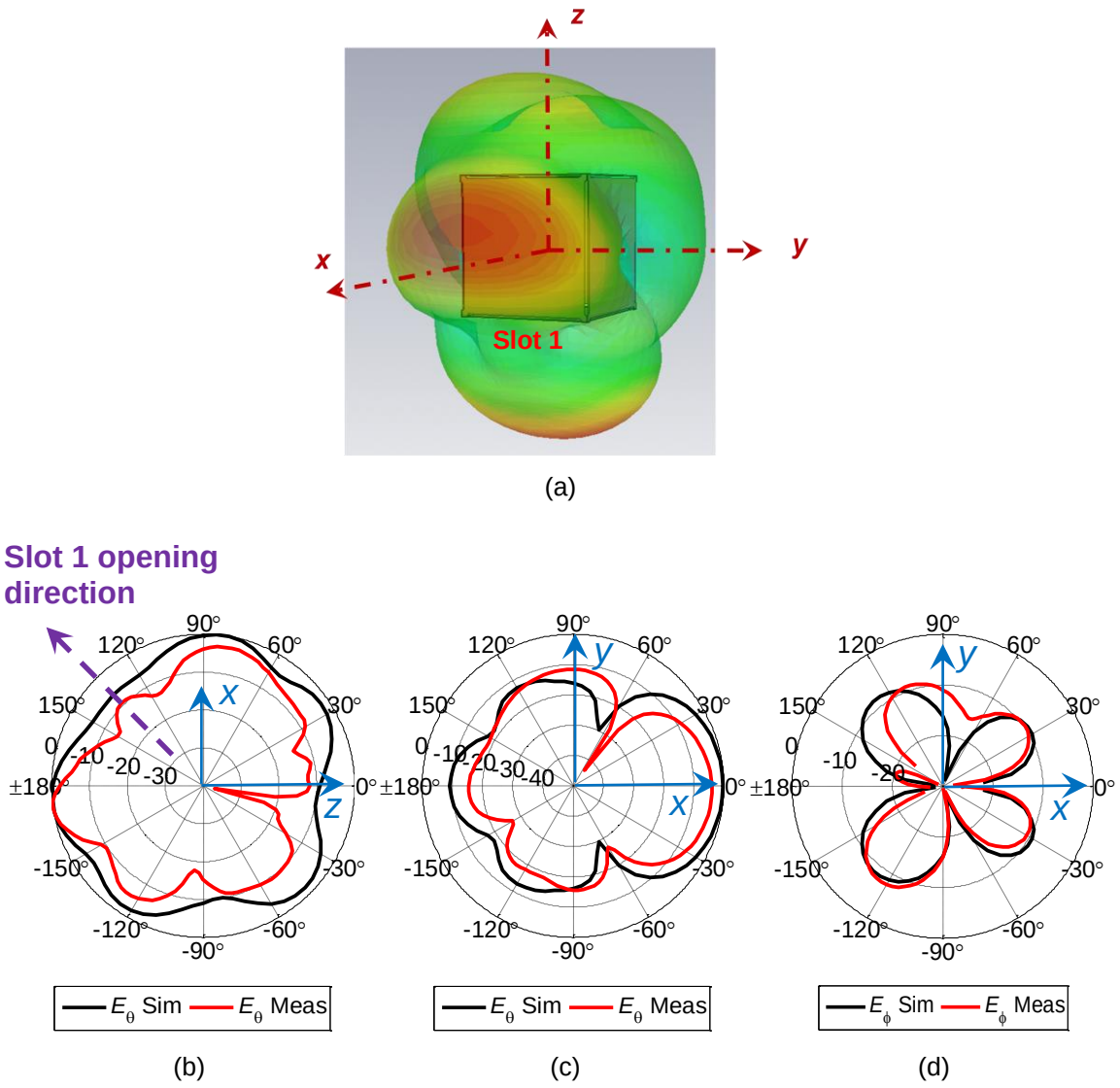

Figure 7.5 Normalized patterns of the slot 1 of the hollow cube at L/λ=0.7

(a) 3D simulated pattern; (b) E_θ in *x-z* plane (ϕ=0^o), simulated and measured ; (c) E_θ in *x-y* plane (θ=90^o), simulated and measured; (d) E_ϕ in *x-y* plane (θ=90^o), simulated and measured

In *x-z* plane, E_θ is the dominant component, and E_ϕ is 90dB lower from simulation and 20dB lower from measurement so it is not plotted here. The slot 1 opening direction is to θ=135^o, as indicated in Fig. 7.5(b). The maximum radiation

is towards the *x* and *-z* directions, rather than aligned with the slot's opening direction. This means that the slot 1 couples to the rest of the cube structure, including to the other slots, via the cavity of the hollow cube. In Fig. 7.5(d) E_ϕ is no longer negligible but it remains low. The simulated directivity is 5.9dBi for each embedded element at L/λ=0.7 and measured one is about 4.2dBi.

The hollow cube has low but finite mutual coupling. The cavity inside the cube is likely to be the cause of coupling. In the next section, this internal coupling is eliminated by partitioning the cube into 12 identical cells. The transmission coefficients and the patterns are compared with those of the hollow cube, in order to clarify the dominant cause of the coupling of the cube.

7.3 Partitioned slot cube MEA

Fig. 7.6(a) and (b) shows the photo and design schematic of the combined cube with 12 identical cells and how the external coaxial feed cables are arranged to minimize their presence. The photo of one cell is shown in Figs. 7.6(c) as an example. The cell is created by connecting the cube centre (indicated as "O" in Fig. 7.6(a)) to the diagonals of the cube walls (lines AB, BC, AD and CD) with metal sheets. This partitioning uses all the volume of the cube, but clearly other partitioning methods are possible which leave volume available for feeding, electronics, etc. The cable arrangement is the same for the hollow cube measurement in the preceding section.

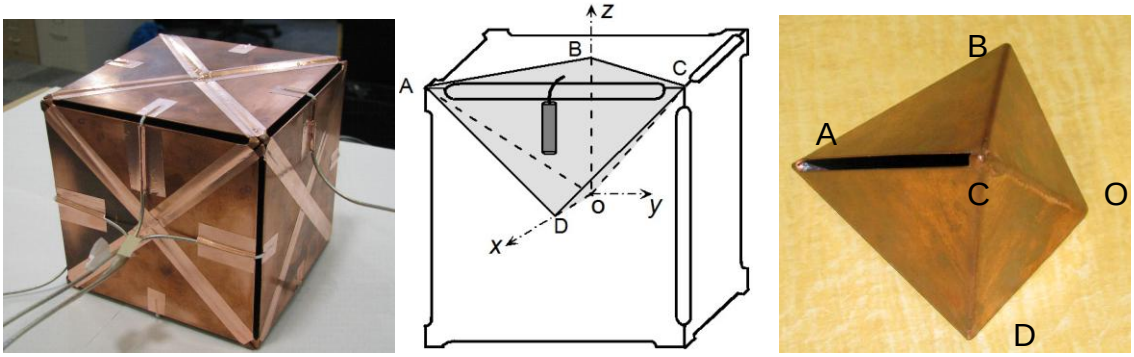

(a) (b) (c)

Figure 7.6 Partitioned slot cube

(a) photo and (b) schematic; (c) photo of one cell of the partitioned cube

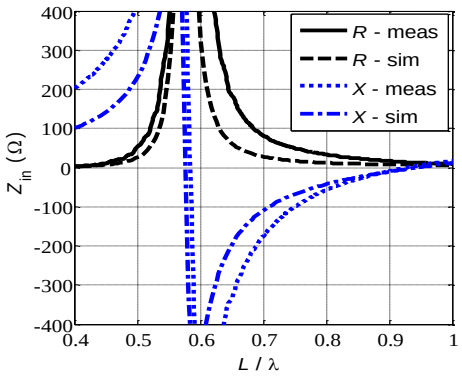

Figure 7.7 Input Impedance of one cell of the partitioned cube

Each cell is a cavity-backed slot comprising 1/12 of the cube volume. The volume in the cavity has a strong influence on the impedance of the slot. Fig. 7.7 shows the second resonance moves to a higher frequency and the input resistance is no longer around 50Ω over a wide frequency range. Now all the $|S_{i,1}|$ are about 20dB lower than the ones of the hollow cube, with typical values

from -30dB to -50dB over the frequency range of interest. This decoupling is from the partitioning of the cube, and it is also evident from the simulated normalized patterns of slot 1 in Fig. 7.8. In the *x-z* plane, E_θ is more directional towards the slot opening direction. The cross-polar level, $E_{\phi,}$ is lower, despite the complex shape of the antenna. The simulated directivity is 4.9dBi at L/λ=0.7.

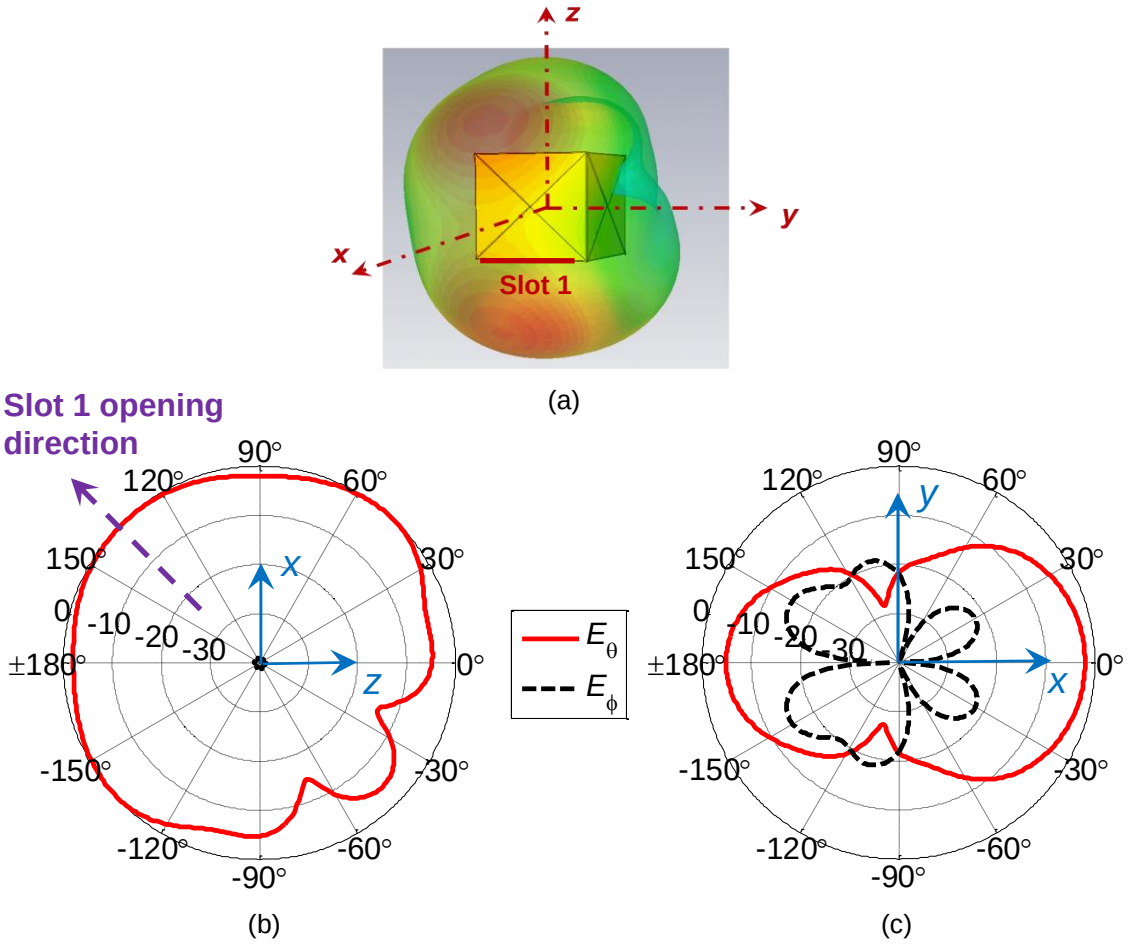

Figure 7.8 Normalized patterns of slot 1 of the partitioned cube MEA at L/λ=0.7

(a) in *x-z* plane (ϕ=0°); (b) in *x-y* plane (θ=90°)

7.4 Correlation matrix and approximations

The correlation approximation uses the same approach as in Section 2.2.4 and Section 6.4.

In Fig. 7.9 and 7.10, the hollow cube's estimated open and loaded circuit voltage correlation coefficient, in the range ($0.6 \leq L/\lambda \leq 0.8$), are computed from simulation and measurement data, respectively. The results from measurement and simulation agree reasonable well.

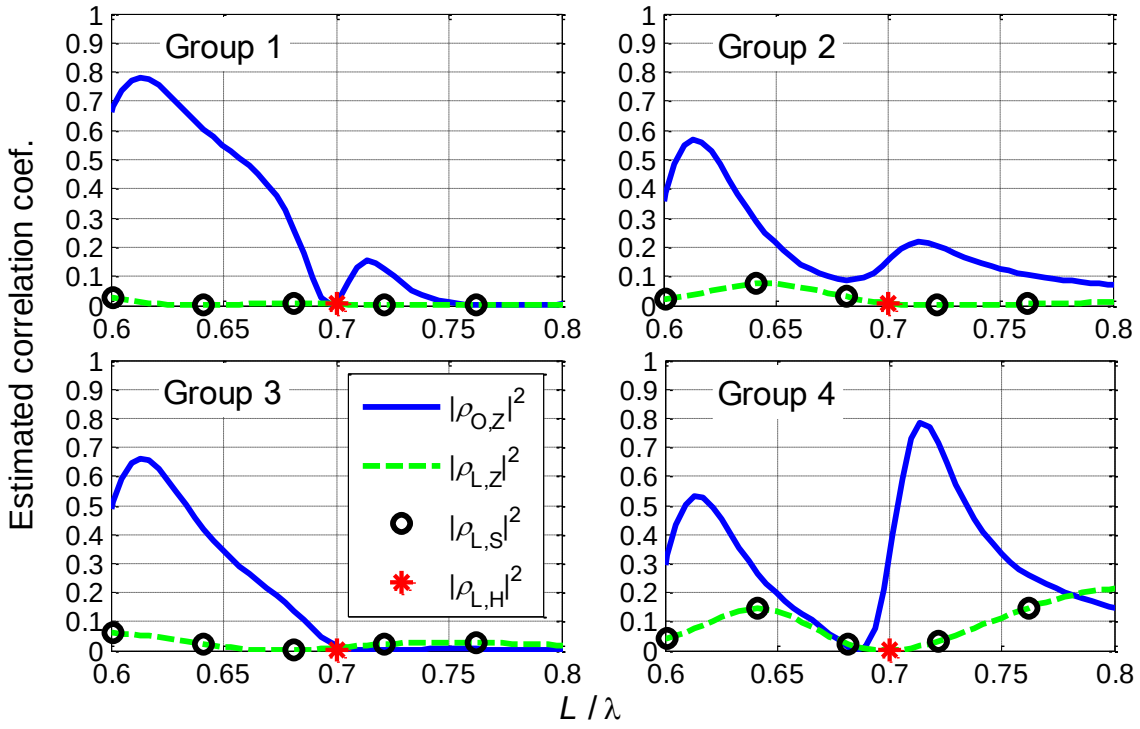

Figure 7.9 Estimated correlation coefficients of the hollow cube from simulations

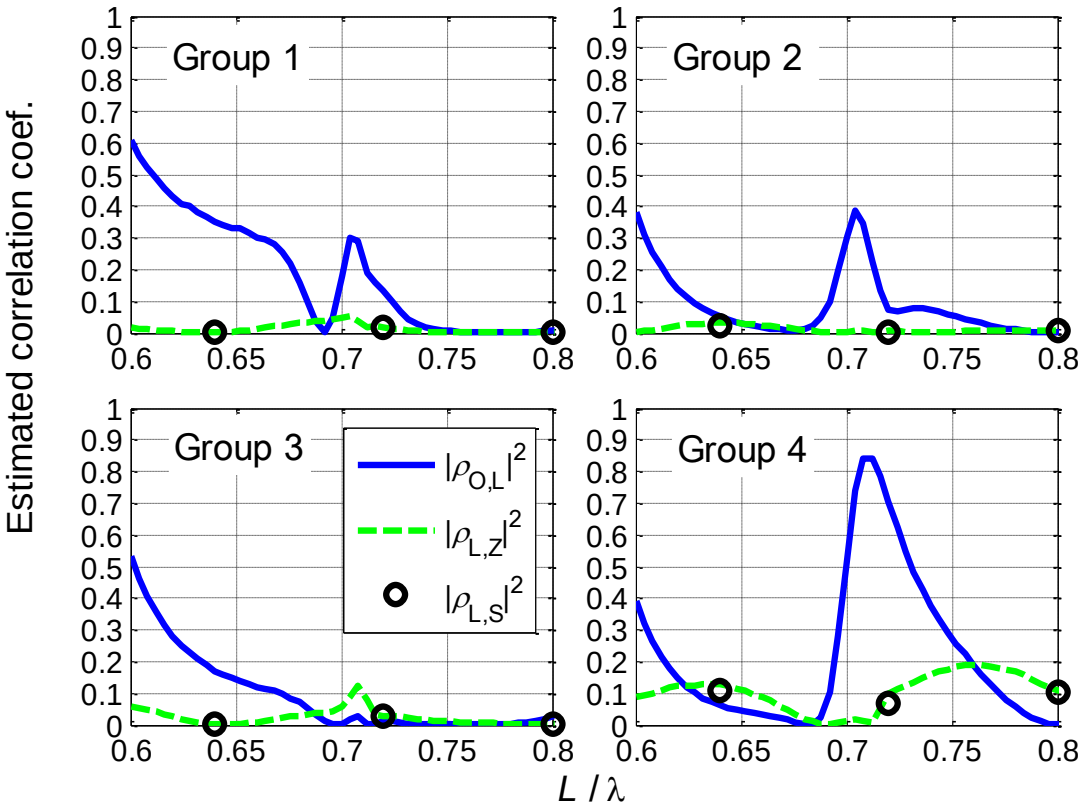

Figure 7.10 Estimated correlation coefficients of the hollow cube from measurements

In Figs. 7.9 and 7.10, $|\rho_{O,Z,ij}|^2$ is mostly lower than 0.5 for slots in the first three groups, but it is nearly 0.8 for the slots in the fourth Group. These higher correlations between the slots in Group 4 agree with the observation of highest mutual coupling in the same group in Fig. 7.4. $|\rho_{L,Z,ij}|^2$ is much lower than $|\rho_{O,Z,ij}|^2$ with all the values well below 0.1 across the band of interest. The estimated loaded circuit voltage correlation for the slots in Group 4 is no longer higher than for the other groups, so the stronger mutual coupling is not evident in ρ_L.

As mentioned in Chapter 6.3, the comparison of $\rho_{O,Z}$ and $\rho_{L,Z}$ demonstrates how the open circuit voltage correlation contains different information than the loaded circuit voltage correlation. $\rho_{O,Z}$ relates to the MEA itself and can be used for non-simultaneous combining, while $\rho_{L,Z}$ also includes the impact of the MEA terminations, and is used for simultaneous combining.

We have used the practical approach of purely resistive loads here, i.e., no attempt is made to tune out the mutual reactance, or to optimize for a performance criteria. (Different optimization criteria, such as limiting theoretical capacity, total received power, etc., result in different optimal load matrices.) Here we note that the slot element resistive loads play a positive role, in the sense that the loaded circuit voltage correlations are reduced compared with the open circuit voltage correlations. This result is not general, but the same observation is reported in other MEAs, e.g., [55]-[57][119].

As expected, the S-parameter-derived $\rho_{L,S}$ is equivalent to the mutual impedance-derived $\rho_{L,Z}$. The loaded embedded pattern-derived $|\rho_{L,H,ij}|^2$ at L/λ=0.7 shown in Fig. 7.10 is also the same. All these approximations to the loaded circuit voltage correlation are equivalent.

Fig. 7.11 gives the estimated correlation coefficient matrices of the partitioned cube given from the measured data. $|\rho_{O,Z,ij}|^2$ is greatly reduced, compared to Figs. 7.10, and similar to $|\rho_{L,Z,ij}|^2$ and $|\rho_{L,S,ij}|^2$ over the frequency range of interest. The simulation results are all well below 0.1 so they are not plotted.

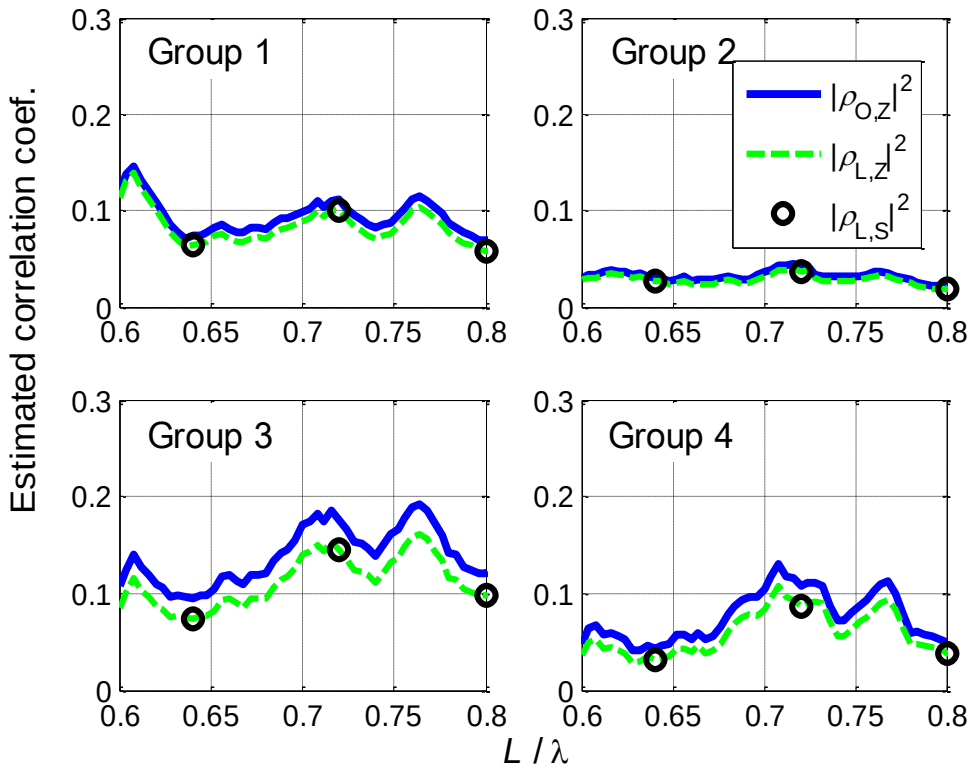

Figure 7.11 Estimated correlation coefficients of the partitioned cube from measurements

The partitioned slot cube has improved MEA correlation, however its impedance bandwidth is narrow and this is caused by the small cavity size of each partitioned cell. Matching circuits are required to match the slots to 50Ω coaxial cables. This partitioned model demonstrates a method to reduce the correlation of the slot cube MEA. However, the element bandwidth is much lower, with theoretical bandwidth in the order of only 8%, and the fabrication is complicated. In the next sections, only the hollow slot cube's diversity, capacity and compactness will be discussed.

7.5 Diversity performance

In Fig. 7.12, the singular values of the scaled correlation coefficient matrix of the hollow slot cube, found with Eqs. (3-14) and (3-15) from simulation data, are compared for non-simultaneous and simultaneous combining for the antenna with L/λ=0.7. The correlation matrices are $\rho_{o,z}$ and $\rho_{L,z}$ from Fig. 7.9. The MEA total efficiencies from both simulation and measurement are listed in Table 7.2. All cases are for the uniform propagation scenario.

The radiation efficiency of the hollow slot cube is almost unity, but the total efficiency is low when its elements are simultaneously terminated (e.q. MRC). This is caused by the power lost to the loads of the elements through mutual coupling. Although the slot cube has low mutual coupling and low correlation among the elements, the total power lost from one element to the loads of the other elements is significant since the number of elements (M=12) is large.

Table 7.2 Embedded MEA total efficiencies

η_{total}	Hollow cube open circuit	Hollow cube loaded circuit
simulated	0.94	0.32
measured	0.97	0.33

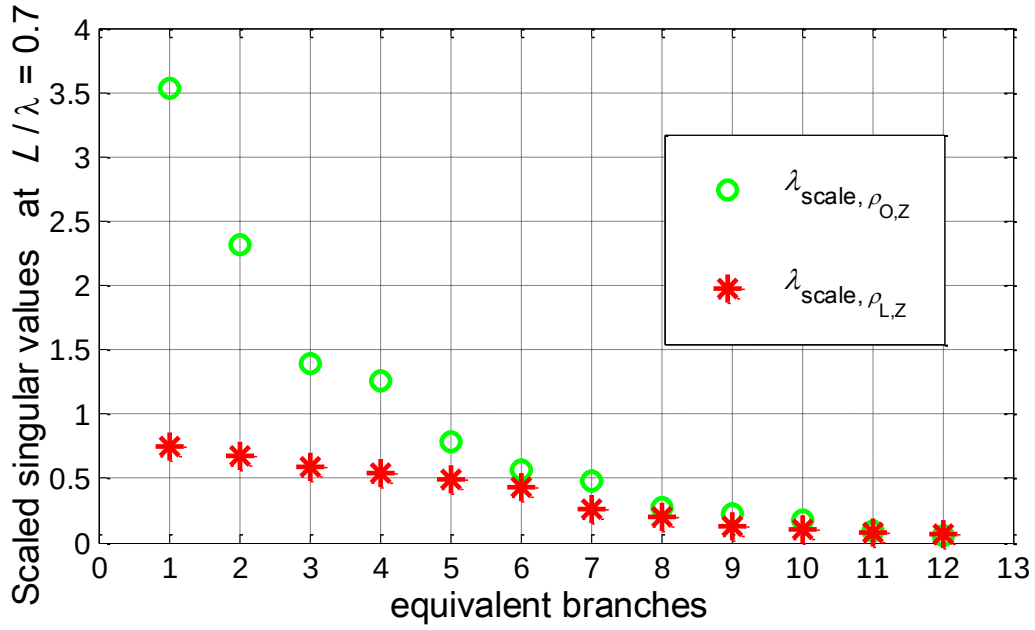

Figure 7.12 Scaled singular value for each equivalent branch of the hollow cube

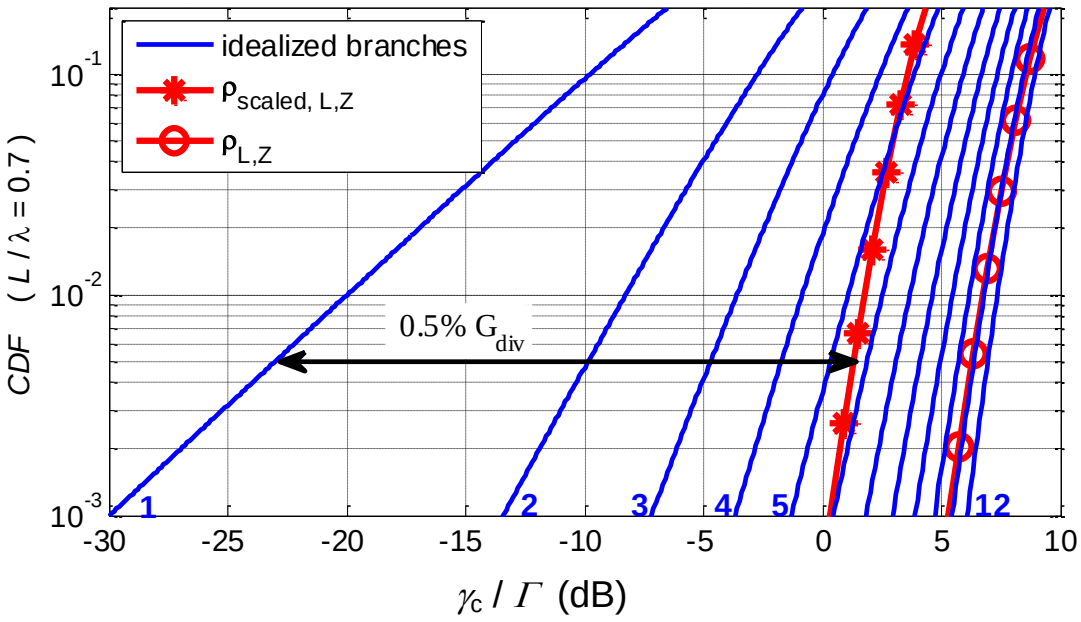

Figure 7.13 MRC *CDF* for diversity gain of the hollow slot cube

In Fig. 7.13, the solid curves are the MRC *CDF*s of idealized MEAs (uncorrelated and lossless) having 1 to 12 antenna branches from left to right. The circle-marked curve is for the hollow slot cube at L/λ=0.7 with MRC, including only the impact of correlation but without including the impact of the MEA total efficiency. It overlaps with the curve for the 11-branch idealized MEA, so the diversity order of this slot cube is slightly reduced (by about one ideal branch), owing to the finite correlation among the slot elements. Taking the leftmost curve (single branch) as the reference antenna, and a probability of 0.5%, the diversity gain is G_{div}=29dB, which is 1dB less than the idealized case.

The star-marked curve is for when the impact of both the correlation and the total efficiency are included. It is parallel to the circle-marked curve, and is near the curve for the 6-branch idealized MEA. Now the diversity gain of the MEA is G_{div}=25dB at the probability of 0.5%. Comparing the star-marked and circle-marked curves, the correlation reduces the MEA diversity order by one ideal branch (G_{div} is reduced by 1dB), and then the MEA total efficiency reduces the diversity order by five more idealized branches (G_{div} is further reduced by 4dB). Now this 12-element MEA with MRC has a diversity order of only M_e=6, but its transmission reliability at 0.5% probability is still improved by a diversity gain of 25dB over a single element antenna, as given in the following table

Table 7.3 MRC diversity performance of the hollow slot cube MEA

	MRC diversity order branches (M_e)	G_{div} (0.5%)
Hollow slot cube MEA	6	25 (dB)

7.6 MIMO capacity

Fig. 7.14 gives the averaged capacity: of idealized MEAs at both ends of the link; with the hollow slot cube used at the receive end, and at both ends of the link.

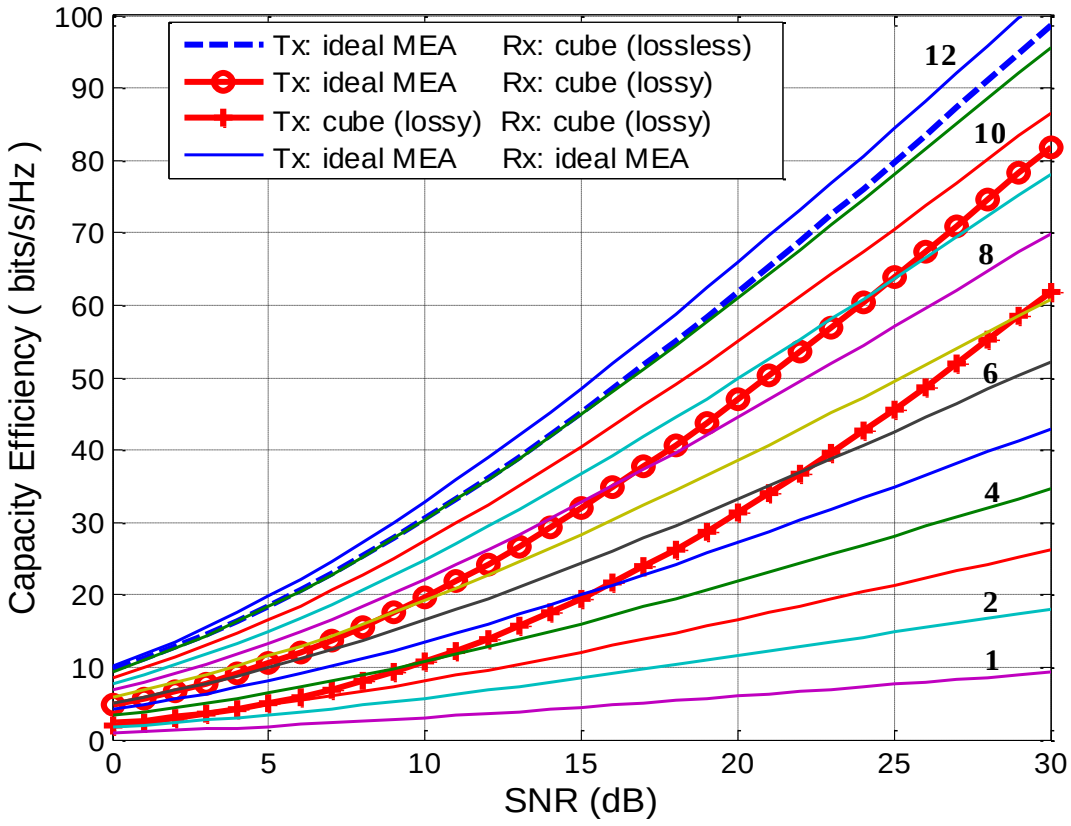

Figure 7.14 MIMO capacities of idealized and hollow slot cube MEAs

The solid curves are the averaged capacities for idealized MEAs with the order of 1 to 12 in Rayleigh channels.

The dashed curve is for the case when an idealized 12-element transmit antenna is used, and the slot MEA with unity efficiency is receiving. This curve is between the MIMO capacity order of 11 and 12. In other words, the correlations between the slot cube elements decreases its MIMO capacity only slightly. This lossless form of the slot cube MEA is equivalent to an idealized MIMO antenna with 11.2 branches for *SNR*=20dB.

The circle-marked curve includes the effect of MEA total efficiency for using the slot cube at the receiver and an idealized 12-element MEA at the transmitter. The curve has a capacity order of about 9 when *SNR* is higher than 15dB, and a capacity order between 7 and 8 for lower *SNR*. The significant drop in MIMO capacity is caused by the MEA total efficiency. For an *SNR* of 20dB, this MEA is equivalent to an 8.5-branch idealized MEA in terms of it capacity.

The cross-marked curve is when the slot cube MEA is used at both the transmitter and receiver, i.e. it includes the total efficiencies for each MEA. This capacity is obviously further decreased. The pair of slot cube MEAs is equivalent to a pair of 6-branch idealized MEAs when *SNR*=20dB.

7.7 Compactness and space efficiency

Fig. 7.15 gives the radiation quality factor of the hollow slot cube near the resonance. It is obtained from the simulated loaded-circuit embedded-element input impedance. At the resonance, the radiation quality factor Q_{rad}; the derived fractional impedance bandwidth from Q; and the 50Ω impedance bandwidth from input reflection coefficients; etc., are listed in Table 7.4.

Table 7.4 Quality factors and bandwidths of hollow slot cube at L/λ=0.7

	Q_{rad}	η_{rad}	Q	-10dB BW from Q	-10dB 50Ω BW
Hollow slot cube	2.5	~1	2.5	27%	30%

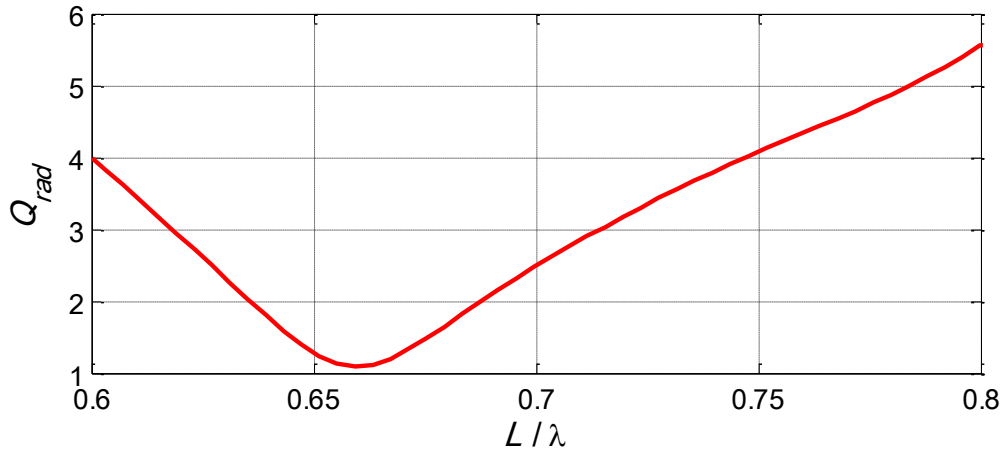

Figure 7.15 Q_{rad} derived from simulated element input impedance

The diversity order of the hollow slot cube for *SNR*=20dB at L/λ=0.7 is M_e=6 from Table 7.3, and it results in the effective element electrical radius of

$$ka_e = \frac{2\pi}{\lambda}\frac{a}{\sqrt[3]{M_e}} = 2.3, \qquad \text{where, } M_e = 6,\ a = \frac{\sqrt{3}}{2}d,\ d = 0.76\lambda \tag{7-1}$$

The compactness evaluation of the MEA is as listed in Table 7.5.

Table 7.5 Compactness evaluation of the hollow slot cube at L/λ=0.7

	M_e	Q_{rad}	ka_{Chu}	ka_e	η_{space}
Hollow slot cube	6	2.5	0.75	2.3	0.33

Fig. 7.16 gives the space efficiency of the hollow slot cube against its equivalent number of idealized elements, and compared with all the MEAs discussed above. The hollow slot cube has a space efficiency which is nearly 7% lower than the reference idealized circular 6-element dipole array. This demonstrates how the space efficiency can be used to evaluate compactness over different types of MEAs.

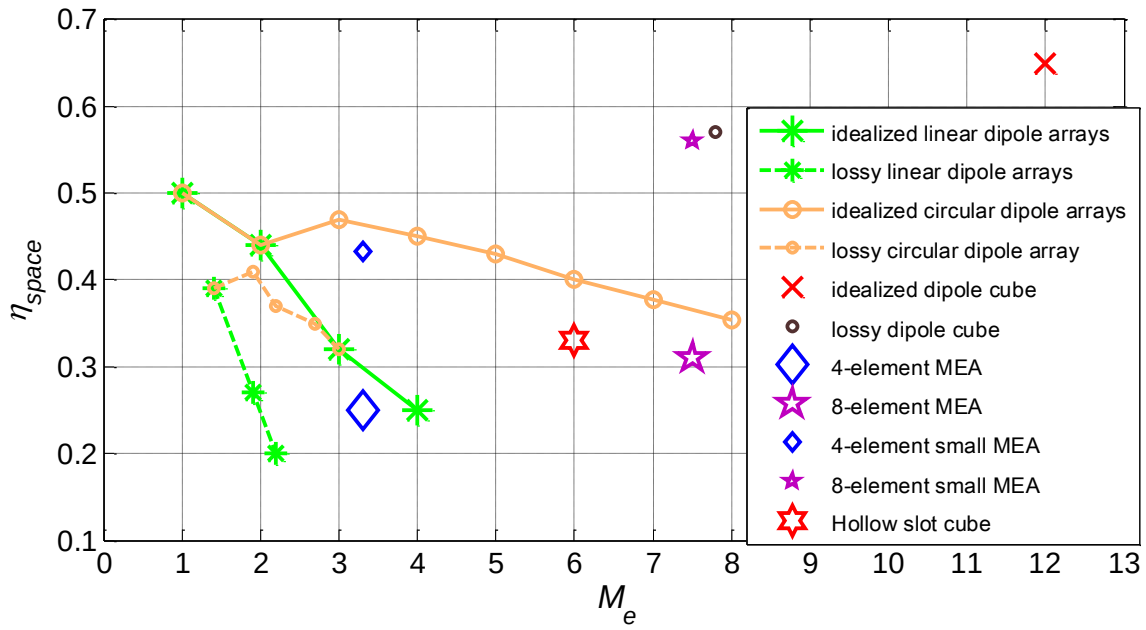

Figure 7.16 η_{space} of dipole arrays and slot-wedge MEAs against M_e

The hollow slot cube's total efficiency is the main cause of the reduced (relative to the idealized case) diversity performance, and the ensuing space efficiency. The mutual coupling between each two slot elements is small.

However this MEA has a large number of elements (M=12), so the total power lost to the loads of the MEA elements through mutual coupling is significant.

7.8 Conclusion

A new design of MEAs with a large numbers of elements can be realized by placing slots on the edges of polyhedron surfaces. A 12-port hollow slot-cube example is presented. At the second resonance (L/λ=0.7) the -10dB 50Ω impedance relative bandwidth for each element is 30%. The mutual coupling is low but finite. To investigate the main cause of the coupling, the cube is partitioned into 12 identical cells, each comprising a slot element and a cavity with 1/12 of the cube volume. Although this makes a complicated structure whose bandwidth is limited by the cell cavity electrical volume, the partitioning reduces the mutual coupling to very low levels.

The correlation coefficients of the two MEAs are compared, showing that the partitioned slot cube has reduced correlation but also has a much narrower bandwidth. Also, matching circuits are needed for feeding the slots with 50Ω coaxial cables.

The MEA performances of the hollow slot cube are discussed, including total efficiency, diversity, capacity and compactness. Although the mutual coupling among the slot elements is low, the number of slot elements is large, so the total power lost from one element to the loads of the elements through mutual coupling is considerable, and the MEA has a total efficiency of only 32%. The low MEA total efficiency greatly impacts the MEA's diversity gain, capacity

performance, and its space efficiency. This 12-element slot cube is equivalent to a 6-element idealized MEA in terms of its diversity gain and capacity, while its space efficiency is about 7% lower than an idealized (no element losses, zero correlation, and no mutual coupling losses) 6-element circular first resonance dipole array.

One important conclusion from the hollow slot cube performance analysis is that, in order to use an MEA with a large number of elements to achieve high data throughput, the elements need to have very low mutual coupling. Even with low mutual coupling or low correlation, the MEA total efficiency can still be poor, and the MIMO performance of the MEA is greatly reduced. The larger the number of antennas, the more sensitive the MEA performance to mutual coupling.

CHAPTER 8: CONCLUSIONS

MIMO is a powerful solution for significantly increasing data throughput and reliability without additional transmit power and bandwidth. Multiple element antennas (MEAs) are used at both the transmitting and receiving ends of MIMO systems to exploit spatial channels. However, the complexity of compact MEA design and the associated signal processing are the challenges in MIMO implementation.

This dissertation contributes MEA design and analysis techniques, and explores new types of elements and MEAs. New figures of merit are proposed to evaluate antennas for MIMO, including MEA efficiencies and compactness. The evaluation processes are demonstrated with both idealized dipoles and realistic slot MEA examples. These slot MEAs are designed based on the sophisticated slot element analysis, including the impact of the rectangular slot shape, the groundplane effect, and the correlation between elements.

Each part of the dissertation is summarized as follows.

Chapter 2 addresses MIMO antenna design and evaluation techniques currently available in the literature.

In Chapter 3, formulations for the efficiencies of an MEA with diversity combining are developed in the context of MIMO communications performance.

The MEA *embedded element efficiency* is derived for both the transmitting and the receiving cases, so that the principle of reciprocity can be simply interpreted for MEAs. The *total efficiency of the embedded element* is also presented. The *MEA total efficiency* is expressed as a diagonal matrix of the total efficiencies of the embedded elements. This matrix form is then used to calculate the impact of the MEA total efficiency on the communications performance in terms of the diversity gain and capacity. When the MEA has an element-symmetric structure (all elements see the same antenna structure) then all the embedded element efficiencies are the same, and the formulations simplify and align with a known result. The reductions in the diversity gain and capacity, resulting from finite correlation coefficient and the total loss (ohmic, and through mutual coupling) are separated in order to analyze the different performance degradations. The diversity order and MIMO capacity order of an MEA are expressed as an equivalent number of idealized branches – i.e., lossless, equal gain, uncorrelated and uncoupled. This metric allows a performance comparison of different MEA designs.

In Chapter 4, the evaluation of MEA compactness is discussed with respect to the antenna bandwidth and MIMO communications performance, *viz*, diversity order, or capacity efficiency. An equivalent number of idealized elements of an MEA is defined from the antenna diversity gain performance. This equivalent number can also be defined from other communications performance measures such as the capacity of the antenna. The space efficiency is used as a metric for evaluating the spherical compactness of an MEA. Some element-

symmetric dipole MEAs are used as examples to demonstrate the process to evaluate different types of MEAs with the proposed metric.

Chapter 5 focuses on a slot antenna at its second resonance in a finite groundplane as a simple wideband antenna. Low correlation between closely spaced orthogonal elements is demonstrated. Besides wide bandwidth, this slot element has medium gain, extremely simple fabrication and associated low cost, and simple connection directly to 50Ω impedance, including to coax cable, without the need for a matching circuit or balun. The groundplane can also be bent along the slot axis without reducing the bandwidth, to give some control over the gain. In this way, it can have a higher directivity of 10dBi in the direction of the acute angle of the bent plate, for the considered antenna dimension.

Chapter 6 and Chapter 7 present the examples of combining multiple slot elements in different geometries yielding new MEAs for MIMO communication. Their MIMO performances are evaluated with the proposed methods. Slot polyhedron MEAs are proposed as a new type of antenna with a large number of elements. Variations of the slot polyhedron MEAs are suggested.

APPENDIX A: MEAS VS. ARRAYS

There is an IEEE definition for an antenna with identical and regularly arranged elements as a conventional array in [1]. But there is not a standard definition describing a multiport antenna that does not have the regularity of an array. “MEA” is a term for such antennas.

An MEA is a more general multiport antenna than an array, and it includes arrays as a special case. It can comprise irregularly spaced elements (*cf*., sparse arrays and random arrays), differently oriented elements (*cf*., rotated elements for certain (usually circular) polarized patterns), and, in particular, it can comprise different elements which are irregularly spaced and oriented. In this dissertation, to follow the IEEE convention, *arrays* refer to the antennas with regular, identical elements, and *MEAs* specifically refer to the multiport antennas for MIMO/diversity applications.

From a design point of view, the differences between an MEA and an array can be viewed as the following. Firstly, array elements are normally identical and arranged regularly to be able to achieve a desired pattern. Array synthesis is to obtain array patterns with specific properties. An MEA may have different types of elements, typically arranged to minimize mutual coupling for maximizing diversity performance, while also seeking a minimal size. In most cases, the MEA elements need to be arranged to suit the shape and volume

requirements of the platform. Secondly, in terms of antenna patterns, arrays often strive for narrow beams and high spatial resolution, and are therefore expansive (large aperture), while MEAs normally strive for wide angular coverage for multipath propagation. Moreover, array antennas are classically configured to send/receive one signal at a time, shared by all the elements, whereas MEAs sometimes function by using different elements for transmitting different signals (*viz*., for some MIMO communications schemes). Adaptive MIMO technology defines the MEA termination architecture and signal combining algorithms, both of which in turn play central roles in the MIMO performance. Since we are interested in the potential communications performance of the antenna, we consider MEAs to include the signal combination. The feed structures of MEAs can be very different to that of a classical array. For a fully digital beamformer, each element is individually amplified and digitized, and then the feed structure difference between the array and MEA is within the digital processor.

Applications also tend to distinguish an array from an MEA. Arrays are classically considered for use in line-of-sight type of scenarios, where, in the receive case, for example, a wanted signal and any interfering signals have well-defined directions of arrival. Arrays tend to be for improving the signal reception/transmission by addressing far field pattern maxima, and/or minima to suppress interference. Examples include radar arrays, and interference cancelation systems that use pattern beamforming. On the other hand, MEAs tend to be compact and to improve signal reception reliability and data throughput in multipath environment, where diversity and MIMO techniques are

deployed. The term beamforming is still used for MEAs, but in reference to the signal processing operation. The patterns cannot be readily interpreted in multipath scenarios especially those with wide angular spreads.

In terms of evaluation, classical array antennas have different evaluation criteria from MEAs. A few of the differences are as follows:

1) A large number of elements in a radar antenna are used to achieve high gain, often with beam steering, and perhaps interference (jammer and clutter) suppression. Pattern parameters, such as gain, beam width, polarization axial ratio, etc., are the evaluation criteria for the antenna.

2) MEAs are used in multipath environment, where high directive gain is not of primary interest. MEAs are used to achieve antenna diversity and MIMO communications. Therefore diversity and communications performances are the primary interest, and there is seldom a focus on the usual pattern parameters. Instead, the particularly useful parameters include distributed directivity, MEG, and pattern correlation.

3) Normally, array elements are spaced by more than a half wavelength. The spacing is related to reducing the mutual coupling [125] while also avoiding directional aliasing, i.e., grating lobes. Close spacing is addressed in [126], but this is a special case. For MEAs, the element spacing is minimized as well, but the arrangement is not necessarily regular. The mutual coupling for MEAs is of even more interest than for arrays because it relates to the correlation in certain conditions (propagation scenario which is: the same for each embedded element; angularly uncorrelated; uncorrelated between polarizations, and uniformly

spanning the field of view of the embedded element patterns; and the elements should have minimum scattering properties) [11][12]. In addition, with different diversity schemes (e.g., maximum ratio combining (MRC), equal gain combining (EGC), switch combining (SwC), etc., *cf*. [12]), different MEA elements may have different terminations (open or short circuited, reactively terminated, or loaded with an impedance match). These result different impacts from the mutual coupling. The impact is more difficult to analyze in MEAs [130] than in classical arrays.

4) The proposed space efficiency is a figure of merit for an MEA. It can be used to compare the compactness of different MEAs with respect to the overall MIMO/diversity communication performances in different scenarios. This is different to existing array evaluation. The MEA space efficiency can still be applied to arrays, but then in such a configuration (i.e., with diversity combining) we prefer to call the array an MEA.

An MEA is typically more compact than a classical array for a given number of elements. This is because the required far field patterns are normally less directive than that of an array, and is often realized by using closely spaced elements with different patterns. The MEA tends to have a wider field of view (FOV is a term often used with arrays) than a classical array, and can be the whole sphere. Moreover, the array is often for a specific polarization, whereas the MEA seldom seeks a predetermined polarization purity. As noted above, the low directivity and associated wide FOV are for operating in multipath.

APPENDIX B: FUTURE DIRECTIONS FOR SLOT MEA DESIGNS AND APPLICATIONS

Possible new designs with slot elements include the following:

1) Linear array of slot-wedge antennas: the use of several slot elements in the same conducting plate can make an MEA. The simplest example would be multiple slots at multiple folds of bends in a plate.

2) Cylindrical and spherical MEAs: multiple slots mounted on a conducting cylinder, a sphere or double curved surfaces.

3) Mechanically reconfigurable slot-wedge antennas for reconfigurable arrays with reconfigurable patterns. If the slot-wedge element is realized to support an adjustable (reconfigurable) bending angle, i.e., conductive plates are hinged, the changing bending angle provides a variable antenna pattern and variable gain. This has the advantage of being able to vary the pattern by simple mechanical variation of a simple structure. Furthermore, the impedance remains essentially constant as the bending angle changes. We have demonstrated a large range of bending angles, 30^{o} to 330^{o}. This constant impedance behavior cannot be attained by using a classical corner reflector which needs to be fed by a dipole element mounted within the wedge for example. In the corner reflector antenna case, as the corner (or bending) angle changes, the position of the dipole feed must change to maintain an impedance match. Multiple wedge

antenna elements in the form of an array can provide a larger gain, in the usual way used with arrays. Multiple slot-wedge elements that are reconfigurable can be formed in a linear array using a concertina shape. As the concertina forms and compresses (the wedge angles move away from 180^o representing the planar structure), the elements become closer together. The advantage of this sort of array antenna is the reconfigurable pattern and gain, which can now be large, because there is an array of elements. For example a two element array comprising two 10 dBi gain slot wedge elements would have a 13 dBi gain. In a larger array, there is the possibility of optimizing the wedge conductor size and the bending angle, in order to tailor the pattern to a specific coverage requirement. The design is complicated to optimize, because the performance is enhanced by the diffraction contributions from the wedge edges.

These slot elements and MEAs have applications in:

1) Simple, inexpensive, stand-alone element that connects directly to 50Ω coax cable. Useful in laboratory set-ups, and also useful for access points, base stations, wireless routers, wireless cards, etc.

2) Mobile terminals: Mobile phone antennas require a low profile antenna and edge-mounted slots elements are candidates for MIMO antennas which are flush mounted onto the surface of the mobile phones, laptops, etc.

3) Base Station: The bent slot provides a medium gain element and it can be used for a variety of applications from basic indoor testing antennas to professionally deployed outdoor antennas. In an array, they can be deployed for diversity and MIMO base systems.

4) Wi-Fi Repeater: The slot-wedge MEAs provide 2D coverage and polyhedron MEAs provides 3D coverage for multipath scenario, and they are candidates for indoor and outdoor repeaters.

5) Wireless industry: The slot element could also be used in many small terminals such as USB keys, RF tags, etc.

APPENDIX C: LIST OF PUBLICATIONS ASSOCIATED WITH THE DISSERTATION

Journal Papers:

1) J. X. Yun and R. G. Vaughan, “Open Slot Antenna in a Small Groundplane,” *IET Microwaves, Antennas & Propagation,* vol. 5, iss. 2, pp. 200-213, 2011
2) J. X. Yun and R. G. Vaughan, “MEA Efficiency and Impact on Diversity and Capacity,” *IEEE Transactions on Antennas and Propagation*, Special Issue on MIMO Technology (joint with MTT), accepted
3) J. X. Yun and R. G. Vaughan, “Space Efficiency of Multiple Element Antennas,” *IEEE Transactions on Antennas and Propagation*, under review
4) K. Daheshpour, S. J. Mazlouman, A. Mahanfar, J. X. Yun, X. Han, C. Menon, F. Carpi and R. G. Vaughan, “Pattern reconfigurable antenna based on moving V-shaped parasitic elements actuated by dielectric elastomer,” *IEEE Electronics Letters*, vol. 46 , pp. 886- 888, 2010
5) Chi-Yuk Chiu; Jie-Bang Yan; R. D. Murch; J. X. Yun and R. G. Vaughan, “Design and Implementation of a Compact 6-Port Antenna,” *IEEE Antennas and Wireless Propagation Letters*, vol. 8, pp. 767-770, 2009

Conference papers:

1) J. X. Yun, and R. G. Vaughan, “A View of the Input Reflection Coefficient of the N-Port Network Model for MIMO Antennas,” *IEEE International Symposium on Antennas and Propagation*, Spokane, WA, USA, 2011
2) J. X. Yun, and R. G. Vaughan, “Open Slot Antenna in a Small Groundplane at the Second Resonance,” *IEEE Antennas and Propagation Society International Symposium*, Toronto, Canada, 2010
3) J. X. Yun, and R. G. Vaughan, “Slot-wedge Antenna,” *IEEE Antennas and Propagation Society International Symposium*, Toronto, Canada, 2010
4) J. X. Yun, and R. G. Vaughan, “Slot MIMO Cube,” *IEEE Antennas and Propagation Society International Symposium*, Toronto, Canada, 2010
5) J. X. Yun, and R. G. Vaughan, “Slot-Wedge Multiple-Element Antennas,” *IEEE Antennas and Propagation Society International Symposium*, Toronto, Canada, 2010

6) M. Dehghani Estarki, J. X. Yun, X. Han and R. G. Vaughan, “The Effect of Gap Size on Dipole Impedance Using the Induced EMF”, *EMTS 2010, International Symposium in Electromagnetic Theory*, Berlin, Germany, August 16-19, 2010
7) J. X. Yun, and R. G. Vaughan, “Impedance of Closely Spaced Orthogonal Slot Antennas,” *Canadian Conference on Electrical and Computer Engineering*, 2007.
8) J. X. Yun, and R. G. Vaughan, “Multiport Impedance Testing of Antennas for MIMO Systems,” *IEEE Antennas and Propagation Society International Symposium*, Honolulu, Hawaii, USA, 2007
9) J. X. Yun, and R. G. Vaughan, “Impedance of Slot Antennas on Finite Ground Plane,” *IEEE International Symposium on Electromagnetic Theory*, Ottawa, Ont. Canada, 2007.

BIBLIOGRAPHY

[1] IEEE, “IEEE *Standard Definitions of Terms for Antennas*,” IEEE Standard 145, 1993

[2] H. Bach, J.E. Hansen, “Uniformly spaced arrays”, Chapter 5, in *Antenna Theory, Part I*, Collin and Zucker, McGraw-Hill, 1969

[3] A. C. C. Schell, A. Ishimaru, “Array pattern Synthesis”, Chapter 7, in *Antenna Theory, Part I*, Collin and Zucker, McGraw–Hill, 1969

[4] R. S. Elliott, *Antenna Theory & Design*, revised ed., John Wiley & Sons, 2003

[5] C.B. Dietrich Jr., K. Dietze, J. R. Nealy, and W. L. Stutzman, “Spatial, polarization, and pattern diversity for wireless handheld terminals*”, IEEE Transactions on Antennas and Propagation*, vol. 49, pp. 1271–1281, 2001

[6] T. M. Cover and J. A. Thomas, *Elements of Information Theory*, John Wiley & Sons, 1991

[7] J. H. Winters, “On the capacity of radio communications systems with diversity in a Rayleigh fading environment,” *IEEE Journal of Selected Areas on Communications*, June 1987, SAC-5(5), pp. 871-878

[8] G. J. Foschini and M. J. Gans, "On limits of wireless communications in a fading environment when using multiple antennas," *Wireless Personal Communications*, vol. 6, pp. 311-335, 1998

[9] M. Schwartz, W. R. Bennett, and S. Stein, *Communication Systems and Techniques*. New York: McGraw-Hill, 1966

[10] W. C. Jakes, *Microwave Mobile Communications*, New York, Wiley, 1974

[11] R. G. Vaughan and J. B. Andersen, “Antenna diversity in mobile communications,” *IEEE Transaction on Vehicle Technologies*, vol. 36, pp. 147–172, Nov. 1987

[12] R. G. Vaughan and J. B. Andersen, *Channels, Propagation and Antennas for Mobile Communications*, IEE Electromagnetics Waves, Series, 50, London, UK, 2003

[13] M. Gustafsson, and S. Nordebo, “Characterization of MIMO Antennas Using Spherical Vector Waves,” *IEEE Transactions on Antennas Propagation*, vol. 54, pp:2679-2682, Sept. 2006

[14] L. J. Chu, “Physical limitations of omni-directional antenna,” J. Appl. Phys., vol. 19, pp. 1163-1175, 1948

[15] M. A. Jensen, *Comments on Thesis*, Private Communication with R.Vaughan and J.Yun, June 2011

[16] M. A. Jensen and J. W. Wallace, “Capacity of the continuous-space electromagnetic channel,” *IEEE Trans. Antennas Propag*., vol. 56, pp. 524-531, Feb. 2008

[17] www.3gpp.org, accessed Aug. 2010

[18] E. Seidel, “Progress on “LTE Advanced” - the new 4G standard”, www.nomor.de, July 2008

[19] A. Goldsmith, *Wireless Communications*, Cambridge University Press, 2005

[20] S. A. Banani, and R. G. Vaughan, “ICA with Particle filtering for blind channel estimation in high data-rate MIMO systems”, *IEEE Wireless Communications and Networking Conference (WCNC)*, Sydney, Australia, Apr. 2010

[21] Q. Sun, D. C. Cox, H. C. Huang, and A. Lozano, ‘‘Estimation of continuous flat fading MIMO channels,’’ *IEEE Transaction on Wireless Communications*, vol. 1, pp. 549--553, Oct. 2002

[22] X. Ma, G. B. Giannakis, and S. Ohno, ‘‘Optimal training for block transmission over doubly selective wireless fading channels,’’ *IEEE Transaction on Signal Processing*, vol. 51, pp. 1351--1366, May 2003

[23] M. Biguesh, and A. B. Gershman, ‘‘Training-based MIMO channel estimation: A study of estimator tradeoffs and optimal training signals,’’ *IEEE Transaction on Signal Processing*, vol. 54, pp. 884-893, Mar. 2006

[24] B. Hassibi and B. M. Hochwald, ‘‘How much training is needed in multiple-antenna wireless links?’’ *IEEE Transaction on Information Theory*, vol. 49, pp. 2515-2528, Apr. 2003

[25] C.-Y. Chi and C.-H. Chen, “Cumulant based inverse filter criteria for MIMO blind deconvolution: Properties, algorithms, and application to DS/CDMA systems in multipath,” IEEE Transaction on Signal Processing, vol. 49, pp. 1282-1299, Jul. 2001

[26] L. Tong and S. Perreau, ‘‘Multichannel blind identification: From subspace to maximum likelihood methods,’’ *IEEE Proceeding*, vol. 86, pp. 1951--1968, Oct. 1998

[27] IEEE, "*IEEE Standard Test Procedures for Antennas*," IEEE Standard 149, 1979

[28] K-S. Min, D-J Kim and M-S Kim,"Multi-channel MIMO Antenna Design for WiBro/PCS band", *IEEE International Symposiums on Antennas and Propagation*, pp.1225–1228, June 2007

[29] M. Manteghi and Y. Rahmat-Samii, "Novel Compact Tri-Band Two-Element and Four-Element MIMO Antenna Designs", *IEEE International Symposiums on Antennas and Propagation*, pp.4443–4446, July 2006

[30] M-T Lin and S-J Chung, "A Compact MIMO antenna System with Three Closely Spaced Multi-band Antennas for WLAN Application", *Asia-Pacific Microwave Conference*, pp. 1-4, Dec. 2007

[31] C. Tounou, C. Decroze, D. Carsenat, T. Monediere, and B. Jecko, "Diversity antennas efficiencies enhancement", *IEEE International Symposiums on Antennas and Propagation,* pp.1064–1067, June 2007

[32] J. Guterman, A. A. Moreira, and C. Peixeiro, "Microstrip fractal antennas for multistandard terminals", *IEEE Antennas and Wireless Propagation Letters*, vol. 3, pp.351–354, 2004

[33] S. B. Yeap, X. Chen, J. A. Dupuy, C. C. Chiau, and C. G. Parini, "Low profile diversity antenna for MIMO applications", *Electronics Letters*, vol. 42, pp.69-71, 2006

[34] R. G. Vaughan, "Two-port higher mode circular microstrip antennas," *IEEE Transactions on Antennas and Propagation*, vol. 36, pp. 3, 1988

[35] D. Piazza, P. Mookiah, and K.R. Dandekar, "Computational electromagnetic analysis of a reconfigurable multiport circular patch antenna for MIMO communications", *International URSI Commission B - Electromagnetic Theory Symposium*, 2007

[36] Y. Karasawa and M. Shinozawa, "A compact tri-polarization antenna for MIMO communication systems", *International URSI Commission B - Electromagnetic Theory Symposium*, 2007

[37] Guterman, Jerzy Moreira, Antonio A. Peixeiro, Custodio, "Multi-element omnidirectional wrapped microstrip antenna for MIMO laptop integrated wireless interface," *The First European Conference on Antennas and Propagation*, pp. 1-5, Nov. 2006

[38] S-W Su and J-H Chou, "Internal wideband monopole antenna for MIMO access-point applications," *IEEE International Symposiums on Antennas and Propagation*, pp. 1-4, July 2008

[39] J. Villanen, P. Suvikunnas, C. Lcheln, J. Ollikainen, and P. Vainikainen, “Performance Analysis and Design Aspects of Mobile-Terminal Multiantenna Configurations,” *IEEE Transactions on Vehicular Technology*, vol. 57, pp.1664-1674, 2008

[40] T. W. C. Brown, and S. R. Saunders, “The Intelligent Quadrifilar Helix: A Compact MIMO Antenna for IEEE 802.11n”, *The Second European Conference on Antennas and Propagation*, pp.1–4, 2007

[41] M. Cabedo, M. Gallo, E. Antonino, M. Ferrando, and M.Bozzetti, “Modal analysis of a MIMO antenna for sensor networks”, *IEEE International Symposium Antennas and Propagation*, pp. 1–4, 2008

[42] H. Sato, T. Hayashi, Y. Koyanagi, and H. Morishita, “Small array antenna for 2x2 MIMO terminal using folded loop antenna”, *The First European Conference on Antennas and Propagation,* pp. 1–5, 2006

[43] A. Nemeth, L. Sziics, and L. Nagy, “MIMO Cube Formed of Slot Dipoles”, *Mobile and Wireless Communications Summit*, pp.1–5, 2007

[44] C-Y. Chiu, J-B. Yan and R. D. Murch, “24-Port and 36-Port Antenna Cubes Suitable for MIMO Wireless Communications”, *IEEE Transactions on Antennas and Propagation*, vol. 56, pp. 1170–1176, 2008

[45] J. Sarrazin, Y. Mahe, S. Avrillon, and S. Toutain, “Investigation on Cavity/Slot Antennas for Diversity and MIMO Systems: The Example of a Three-Port Antenna”, *IEEE Antennas and Wireless Propagation Letters*, vol. 7pp. 414–417, 2008

[46] N. Behdad, M. Schamberger, and N. E. Buris, “Slot Antenna Design for Wireless Communications Systems”, The Second European Conference on Antennas and Propagation, pp.1-9, 2007

[47] R. G. Vaughan and J. B. Andersen, “A multiport patch antenna for mobile communications,” *14th European microwave conference*, pp. 607-612, 1984

[48] G. Wen, Q. Rao, D. Wang, S. Ali and M. Pecen, “Compact multi-feed mufti-band antenna designs for wireless mobile devices,” *IEEE International Symposium on Antennas and Propagation*, pp.1036–1039, 2007

[49] B.N. Getu, and J. B. Andersen, “The MIMO cube - a compact MIMO antenna”, *IEEE Transactions on Wireless Communications*, vol. 4, pp. 1136–1141, 2005

[50] P. Loskot and N. C. Beaulieu, “Decorrelation and Orthogonalization of Correlated Diversity Branches for HS/MRC Diversity”, *IEEE Vehicular Technology Conference,* pp. 335–339, May 2008

[51] C. A. Balanis, Antenna *Theory, Analysis and Design*, New York: Harper & Row, 1982

[52] J. D. Kraus, and R. J. Marhefka, *Antennas for All Applications*, 3rd ed., McGraw_Hill Higher Education, 2002

[53] J. L. Allen and B. L. Diamond, “Mutual Coupling in Array Antennas,” *Lincoln Laboratory, M.I.T., Technical Report*, 1966.

[54] P. N. Fletcher, M. Dean, and A. R. Nix, “ Mutual coupling in multi-element array antennas and its influence on MIMO channel capacity,” Electronics Letters, vol. 39, pp. 342-344, 2003

[55] R. G. Vaughan and N. L. Scott, “Closely spaced monopoles for mobile communications”, *Radio Science*, pp.1259–1266, 1993

[56] A. A. Abouda and S. G. Haggman, “Effect of mutual coupling on capacity of MIMO wireless channels in high SNR scenario”, *Progress In Electromagnetics Research,* pp. 27-40, 2006

[57] T. Svantesson and A. Ranheim, “Mutual coupling effects on the capacity of multielement antenna systems,” in *Proc. IEEE Int. Conf., Acoustics, Speech, and Signal Processing*, pp. 2485–2488, 2001

[58] D. M. Pozar, *Microwave engineering*, John Wiley & Sons, Inc, New York, 2nd ed.

[59] R. E. Collin and F. Zucker, *Antenna Theory*, Part 1. New York, McGraw-Hill, 1969

[60] J. B. Andersen and F. Hansen, “Antennas for VHF/UHF personal radio: A theoretical and experimental study of characteristics and performance,” *IEEE transaction on Vehicular Technology*, vol. 26, pp. 349-357, 1977

[61] A. L. Davidson and W. J. Turney, “Mobile antenna gain in multipath environment at 900 MHz,” *IEEE transaction on Vehicular Technology*, vol. 26, pp. 345-348, 1977

[62] T. Taga, “Analysis for mean effective gain of mobile antennas in land mobile radio environments,” *IEEE transaction on Vehicular Technology*, vol. 39, pp. 117-131,1990

[63] A. A. Glazunov, “Mean effective gain of user equipment antennas in double directional channels,” *15th IEEE International Symposium on Personal, Indoor and Mobile Radio Communications*, vol. 1, pp. 432-436, 2004

[64] J. R. Pierce and S. Stein, “Multiple diversity with nonindependent fading,” *IRE Proceddings*, vol. 48, pp. 89-104, 1960

[65] M. Jensen and Y. Rahmat-Semii, “*Performance analysis of antennas for hand-held transceivers using FDTD*,” IEEE Transactions on Antennas and Propagation, vol. 42, pp. 1106-1113, 1994

[66] A. Diallo, C. Luxey, P. Le Thuc, R. Staraj, and G. Kossiavas. “Diversity performance of multiantenna systems for UMTS cellular phones in different propagation environments,” International journal of antennas and propagation, 2008

[67] K. Rosengren and K. Kildal, “Correlation and capacity of MIMO systems and mutual coupling, radiation efficiency, and diversity gain of their antennas: simulations and measurements in a reverberation chamber”, IEEE Communications Magazine, vol. 42, pp. 104–112, 2004

[68] Y. Gao, *Characterisation of Multiple Antennas and Channel for Small Mobile Terminals*, PhD dissertation, University of London, 2007

[69] S.C.K. Ko and R.D. Murch, “Compact integrated diversity antenna for wireless communications,” IEEE Transactions on Antennas and Propagation, vol. 49, pp. 954–960, 2001

[70] M. B. Knudsen and G. F. Pedersen, “Spherical outdoor to indoor power spectrum model at the mobile terminal,” IEEE Journal on Selected Areas in Communications, vol. 20, no. 6, pp. 1156–1169, 2002

[71] Z. Ying, V. Plicanic, T. Bolin, G. Kristensson, and A. Derneryd, “ Characterization of multi-channel antenna performance for mobile terminal by using near field and far field parameters,” *COST* 273, G¨oteborg, Sweden, June 2004

[72] J. Fuhl, A. F. Molisch, and E. Bonek, “Unified channel model for mobile radio systems with smart antennas,” *IEE Proceedings, -Radar, Sonar Navig*., Vol. 145, No. 1, February 1998

[73] C. Montg*omer*y, R. Dicke, and E. Purcell, *Principles of Microwave Circuits*, 1948. McGraw-Hill, New York, 1948.

[74] S. Stein, “On cross coupling in multiple-beam antennas”, *IRE Transactions on antennas and propagation*, pp. 548-557, 1962

[75] I. Salonen and P. Vainikainen, “Estimation of signal correlation in antenna arrays”, *International Symposium on Antennas*, vol. 2, pp. 383-386, 2002

[76] S. Blanch, J. Romeu and I. Corbella, “Exact representation of antenna system diversity performance from input parameter description”, *Electronics Letters*, vol. 39, pp. 705-707, 2003

[77] B. K. Lau, B. J. Andersen, G. Kristensson and A. F. Molisch, “Impact of Matching Network on Bandwidth of Compact Antenna Arrays,” *IEEE Transactions on Antennas and Propagation*, vol. 54, pp. 3225-3238, 2006

[78] D. R. Rhodes, “Observable stored energies of electromagnetic systems,” *J. The Franklin Institute*, vol. 302, pp. 225-237, Sept. 1976

[79] A. Yaghjian and S. Best, “Impedance, bandwidth, and Q of antennas,” *IEEE Transactions on Antennas and Propagation*, vol. 53, pp.1298–1324, 2005.

[80] A. Yaghjian and H. R. Stuart, “Lower Bounds on Q for dipole antennas in an arbitrary volume,” *IEEE International Symposium on Antennas and Propagation*, July, 2010

[81] J. McLean, “A reexamination of the fundamental limits on the radiation Q of electrically small antennas,” *IEEE Transactions on Antennas and Propagation*, vol. 44 pp. 672-676, 1996

[82] V. Plicanic, B. K. Lau, A. Derneryd, Z. Ying, “Actual diversity performance of a multiband diversity antenna with hand and head effects”, *IEEE Transactions on Antennas and Propagation,* vol. 57, pp. 1547-1556, 2009

[83] M. Pelosi, O. Franek, M. B. Knudsen, M. Christensen, G. F. Pedersen, “A grip study for talk and data modes in mobile phones ,” *IEEE Transactions on Antennas and Propagations*, vol. 57, pp. 856-865, 2009

[84] P. S. Kildal, K. Rosengren, J. Byun, and J. Lee, “Definition of effective diversity gain and how to measure it in a reverberation chamber,” *Microwave and Optical Technology Letters*, vol. 34, pp. 56–59, 2002

[85] R. G. Vaughan, “Antenna evaluation for communications with diversity/MIMO”. *Chapter 15 in Printed Antennas for Wireless Systems*, pp. 407-445, Wiley, 2007

[86] J. P. Kermoal, L. Schumacher, K. I. Pedersen, P. E. Mogensen and F. Frederiksen, “A stochastic MIMO radio channel model with experimental validation,” *IEEE Journal on Selected Areas Communication*, vol. 20, pp. 1211–1226, 2002

[87] M. A. Jensen and J. W. Wallace, “A review of antennas and propagation for MIMO wireless communications”, *IEEE Transactions on Antennas and Propagation*, vol.52, pp. 2810-2824, 2004

[88] J. B. Andersen, “Array gain and capacity for known random channels with multiple element arrays at both ends,” *IEEE Journal on Selected Areas Communication*, vol. 18, pp. 2172–2178, Nov. 2000

[89] P. Almers, E. Bonek, A. Burr, N. Czink, M. Debbah, V. Degli-Esposti, H. Hofstetter, P. Kyosti, D. Laurenson, G. Matz, A. F. Molisch, C. Oestges, and H. Ozcelik, “Survey of Channel and Radio Propagation Models for Wireless MIMO Systems,” *EURASIP Journal on Wireless Communications and Networking*, Vol. 2007, Article ID 19070, 2007

[90] 3GPP - 3GPP2 Spatial Channel Model Ad-hoc Group3GPP TR 25.996, “Spatial Channel Model for Multiple Input Multiple Output (MIMO) Simulations,” v6.1.0 (2003-09)

[91] C-Y Chiu; C-H Cheng; Y-S Wan; C. R. Rowell and R. D. Murch, “Design of a Flat Fading 4 x 4 MIMO Testbed for Antenna Characterization using a Modular Approach”, *IEEE Wireless Communications and Networking Conference*, pp.2913–2918, 2007

[92] C. C. Martin, J. H. Winters, N. R. Sollenberger, “MIMO radio channel measurements: performance comparison of antenna configurations”, *IEEE 54th Vehicle Technology Conference*, vol. 2, pp. 1225–1229, 2011

[93] K. Sulonen, P. Suvikunnas, L. Vuokko, J. Kivinen and P. Vainikainen, “Comparison of MIMO Antenna Configurations in Picocell and Microcell Environments”, *IEEE Journal on Selected Areas in Communication*, vol. 21, pp. 703-712, 2003

[94] C. C. Martin, J. H. Winters and N. R. Sollenberger, “Multiple-Input-Multiple-Output (MIMO) radio channel measurements,” *IEEE Vehicular Technology Conference*, pp. 774–779, 2000

[95] J.W. Wallace and M.A. Jensen. “Measured Characteristics of the MIMO Wireless Channel”. *IEEE Vehicular Technology Conference,* pp. 2038–2042 2001

[96] T Svantesson, J Wallace, “On Signal Strength and Multipath Richness in Multi-Input Multi-Output Systems*”, IEEE International Conference on Communications,* vol. 4, pp. 2683-2687, 2003

[97] R. E. Jaramillo, O. Fernandez, R. P. Torres, “Empirical Analysis of 2x2 MIMO Channel in Outdoor-Indoor Scenarios for BFWA Applications”, *IEEE Antennas and Propagation Magazine*, vol. 48, pp. 57-69, 2006

[98] C.-N. Chuah, J. M. Kahn, and D. Tse, “Capacity of multiantenna array systems in indoor wireless environment,” *IEEE Global Telecommunications Conference*, vol. 4, pp. 1894–1899, 1998.

[99] D. Chizhik, F. Rashid-Farrokhi, J. Ling and A.Lozano, “Effect of antenna separation on the capacity of BLAST in correlated channels,” *IEEE Communications Letters*, vol. 4, pp.337-339, 2000

[100] D.-S. Shiu, G. J. Foschini, M. J. Gans, and J. M. Kahn, “Fading correlation and its effect on the capacity of multielement antenna systems,” IEEE Transactions on Communications, vol. 48, no. 3, pp. 502–513, 2000.

[101] K. Yu, M. Bengtsson, B. Ottersten, D. McNamara, P. Karlsson, and M. Beach, “A wideband statistical model for NLOS indoor MIMO channels,” *IEEE 55th Vehicle Technology Conference*, vol. 1, pp. 370–374, 2002

[102] H. Özcelik, M. Herdin, W. Weichselberger, J. Wallace, and E. Bonek, “Deficiencies of the kronecker MIMO radio channel model,” *Electronics Letters*, vol. 39, pp. 1209–1210, Aug. 2003

[103] J.P. Kermoal, L. Schumacher, F. Frederiksen, and P.E. Mogensen, "Polarization Diversity in MIMO Radio Channels: Experimental Validation of a Stochastic Model and Performance Assessment," *Proc. 54th IEEE VTS Fall VTC 2001*, vol. 1, pp. 22–26, 2001

[104] J. F. Valenzuela-Valdés, M. A. García-Fernández, A. M. Martínez-González, and D. A. Sánchez-Hernández, "The influence of efficiency on receive diversity and MIMO capacity for Rayleigh-fading channels", *IEEE Transactions on Antennas and Propagation*, vol. 56, pp. 1444-1450, 2008

[105] H. G. Booker, "Slot aerials and their relation to complementary wire aerials." *IEE Journal*, 93, pt. IIIA, NO. 4 , pp. 620-626,1946

[106] S. A. Long, "Experimental study of the impedance of cavity-backed slot antennas," IEEE Transactions on Antennas and Propagation, vol. 23, pp. 1-7, Jan. 1975

[107] A. F. Stevenson, "Theory of slots in rectangular waveguides," *Journal of Applied Physics,* vol.19, pp.24-38, Jan. 1948

[108] R. S. Elliott, "Longitudinal shunt slots in rectangular waveguide: Part I, theory," *Rantec Report*, No. 72022-TN-1, Rantec, Calabasas, CA

[109] R. S. Elliott and L. A. Kurtz, "The design of small slot arrays," *IEEE Transactions on Antennas Propagation*, vol. AP-26, pp.214-219, 1978

[110] B. N. Das and K. K. Joshi, "Impedance of a radiating slot in the groundplane of a microstripline," *Transactions on Antennas Propagation*, vol. 30, pp. 922-926, 1982.

[111] Y. Yoshimura, "A microstripline slot antenna," *IEEE Transactions on Microwave Theory Techonology*, vol. MTT-20, pp. 760-762, 1972.

[112] D. M. Pozar, "A reciprocity method of analysis for printed slot and slot-coupled microstrip antennas," *Transactions on Antennas Propagation*, vol.34, pp. 1439-1446, 1986.

[113] Sharma, S.K.; Shafai, L.; Jacob, N.; "Investigation of wide-band microstrip slot antenna", *IEEE Transactions on Antennas and Propagation*, vol. 52, pp:865 – 872, March 2004

[114] Qinjiang Rao, Tayeb A. Denidni and Ronald H. Johnston, "A New Aperture Coupled Microstrip Slot Antenna", *IEEE Transactions on Antennas and Propagation*, vol. 53, pp, 2818-1826, Sep. 2005

[115] Hirokawa, J.; Arai, H.; Goto, N.; "Cavity-backed wide slot antenna," IEE Proceedings Microwaves, Antennas and Propagation, vol 136, Issue 1, pp:29-33, Feb 1989

[116] Azarbar, A.; Hassani, H.R.; Jahanbakht, M.; “Fractaly terminated line-fed Microstrip slot antenna”, *International Conference on Microwave and Millimeter Wave Technology*, vol. 4, pp:1641–1643, 2008

[117] H. Zhang and Q. Zhu, “A novel slot antenna on edge of V-curved plates”, *International Conference on Microwave and Millimeter Wave Technology*, pp.373-376, 2002

[118] K. Karlsson, J. Carlsson, I. Belov, G. Nilsson, P.-S. Kildal, "Optimization of Antenna Diversity Gain by Combining Full-Wave and Circuit Simulations," *EuCAP 2007*, Nov. 11-16, 2007

[119] J. W. Wallace and M. A. Jensen, ”Mutual coupling in MIMO wireless system: a rigorous network theory analysis”, *IEEE Transactions on Antennas and Propagation*, vol. 3, pp. 1317-1325, July, 2004

[120] J. X. Yun, and R. G. Vaughan, “A View of the Input Reflection Coefficient of the N-Port Network Model for MIMO Antennas,” *IEEE International Symposium on Antennas and Propagation*, Spokane, WA, USA, 2011

[121] J. B. Andersen and A Frandsen, “Absorption efficiency of receiving antennas,” *IEEE Transactions on Antennas Propagation*, vol. 53, pp. 2843-2849, 2005

[122] J. B. Andersen and R. G. Vaughan, “Transmitting, receiving and scattering properties of antennas,” *IEEE Antennas Propagation Magazine*, vol. 45, pp. 93-98, Aug. 2003

[123] I. Cho, I. Seo, H. Ahn, J. Oh, H. Lee, and Y. Lim, “A Design of the Triple-Band built-in Chip Antenna for Mobile Handset,” *Asia Pacific Microwave Conference*, pp. 2675 – 2678, 2009

[124] C. Mak, and C. R. Rowell, “Miniaturized orthogonal antenna system,” *United States Patent* 7812783, Oct. 12, 2010

[125] J. L. Allen and B.L. Diamond, Mutual coupling in array antennas, MIT Lincoln Lab, 1966

[126] H. Steyskal and J. S. Herd, “Mutual coupling compensation in small array antennas,” IEEE Trans. Antennas Propagat., Vol. 38, pp. 1971-1975, 1990

[127] Y. Kim, C. Song, I. Koo, H. Choi, and S. Lee, “Design of a double-looped monopole array antenna for a DSRC system roadside base station,” *Microw. Opt. Tech. Lett*., Vol. 37, Iss. 1, pp.74–77, April 2003

[128] J. X. Yun, and R. G. Vaughan, “Slot MIMO cube,” *IEEE International Symposium on Antennas and Propagation*, Toronto, Canada, 2010

[129] R. G. Vaughan and D. Meyer, “Slot MIMO cube”, *Technical Report*, IRL, Nov. 2002

[130] J. X. Yun, and R. G. Vaughan, “MEA efficiency and impact on diversity and capacity,” *IEEE Transactions on Antennas and Propagation*, under review

[131] V. Plicanic, B. K. Lau, A. Derneryd, Z. Ying, “Actual diversity performance of a multiband diversity antenna with hand and head effects”, *IEEE Transactions on Antennas Propagation*, vol. 57, pp. 1547-1556, 2009

[132] M. Pelosi, O. Franek, M. B. Knudsen, M. Christensen, G. F. Pedersen, “A grip study for talk and data modes in mobile phones,” *IEEE Transactions on Antennas Propagation*, vol. 57, pp. 856-865, 2009

[133] P. S. Kildal, K. Rosengren, J. Byun, and J. Lee, “Definition of effective diversity gain and how to measure it in a reverberation chamber,” *Microwave Optical Technology Letters*, vol. 34, no. 1, pp. 56–59, July 2002

[134] M. Schwartz, W. R. Bennett, and S. Stein, *Communication Systems and Techniques*, New York: McGraw-Hill, 1966

[135] R. E. Collin, *Foundations for Microwave Engineering*, International Student Ed. McGraw_Hill, Inc. 1966

[136] E. Nyfors and P. Vainikainen, *Industrial Microwave Sensors*, Artech House, 1989

[137] D. Kajfez, *Q factor*, Vector Fields Oxford, MS, 1994.

[138] R. E. Collin and S. Rothschild, “Evaluation of antenna Q,” *IEEE Transactions on Antennas and Propagation,* vol. 12, pp. 23-27, 1964

[139] R. L. Fante, “Quality factor of general ideal antennas,” *IEEE Transactions on Antennas and Propagation*, vol. 17, pp. 151-155 1969

[140] S. Best, “The Foster reactance theorem and quality factor for antennas,” *Antennas and Wireless Propagation Letters*, vol. 3, 2004.

[141] G. Wen, P Jarmuszewski, and Y. Qi, “The foster reactance theorem for antennas and radiation Q,” *IEEE Transactions on Antennas and Propagation*, vol. 48, pp. 401-408, 2000

[142] G. Wen, “A method for the evaluation of small antenna Q,” *IEEE Transactions on Antennas and Propagation*, vol. 51, pp. 2124-2129, 2003

[143] http://www.cst.com accessed Dec. 2009

[144] M. Dehghani Estarki, J. X. Yun, X. Han and R. G. Vaughan, “The Effect of Gap Size on Dipole Impedance Using the Induced EMF”, *EMTS 2010, International Symposium in Electromagnetic Theory*, August 16-19, 2010

[145] M. Gustafsson, C. Sohl, and G. Kristensson, “Illustrations of new physical bounds on linearly polarized antennas,” *IEEE Trans. Antennas Propagat*, Vol. 57, no. 5, pp. 1319–1327, 2009.

[146] M. M. Weiner, S. P. Cruze, C-C. Li, W. J. Wilson, *Monopole elements on circular ground planes*, Artech House, 1987

[147] M. M. Weiner, *Monopole Elements*, Marcel Dekker, Inc., New York, 2003

[148] W. L. Stutzman and G. A. Thiele, *Antenna theory and design*, John Wiley & Sons, Inc., New York, 2nd edn, 1998

[149] R. C. Johnson and H. Jasik, H, *Antenna engineering handbook*, McGraw-Hill, New York, 1961, 2nd edn.1984

[150] J. L. Volakis, *Antenna engineering handbook*, McGraw-Hill, New York, 4th edn. 2007

[151] T. Lertwiriyaprapa, C. Phongcharoenpanich, and M. Krairiksh, “Analysis of radiation characteristics of a probe fed rectangular cavity-backed slot antenna with finite-size ground plane”, *IEEE Antennas and Propagation Society International Symposium*, vol. 2, pp: 714-717, July 2000

[152] C. A. Balanis, and L. Peters, Jr., “Equatorial plane pattern of an axial-TEM slot on a finite sized ground plane”, *IEEE Transactions on Antennas and Propagation*, vol. 17, pp. 351-353, May 1969

[153] C. A. Balanis, “Pattern distortion due to edge diffractions”, *IEEE Transactions on Antennas and Propagation*, vol. 18, pp. 561-563, July 1970

[154] B. Zheng, and Z. Sheng, “Effect of a finite ground plane on microstrip-fed cavity-backed slot antennas,” *IEEE Transactions on Antennas and Propagation*, vol. 53. No. 2, pp. 862-865, Feb, 2005

[155] Y. Yoshimura, “A microstripline slot antenna”, *IEEE transactions on Microwave Theory and Techniques,* pp. 760-762, Nov. 1972

[156] R. Janaswamy, “Analysis of the tapered slot antenna”, *IEEE Transactions on Antennas and Propagation*, vol. Ap-35, pp. 1058-1064, Sep. 1987

[157] J. R. Kelly, and P. S. Hall, “Reconfigurable slot antenna for Cognitive Radio applications”, *IEEE International Symposium on Antennas and Propagation,*pp. 1-4, June 2009

[158] T. M. Weller, L. P. B. Katehi, and G. M. Rebeiz, “Single and double folded-slot antennas on semi-infinite substrates,” *IEEE Transactions on Antennas Propagation*, vol. 43, pp:1423–1428, Dec. 1995

[159] M. W. Nurnberger, J. L. Volakis, J. A. Mosko, and T. Ozdemir, “Analysis of the log-periodic folded slot array”, *IEEE International Symposium on Antennas and Propagation*, vol. 2, pp. 1282–1285, Seattle, USA, June 1994,

[160] D. E. Anagnostou, and A. A. Gheethan, “A coplanar reconfigurable folded slot antenna without bias network for WLAN applications”, *IEEE Antennas and Wireless Propagation Letters*, vol. 8, pp.1057–1060, 2009

[161] T. Moselhy, and H. Ghali, “Design of fractal slot antennas”, *34th European Microwave Conference, Amsterdam*, vol. 3, pp.1265–1268, Oct. 2004

[162] A. Azarbar, H. R. Hassani, and M. Jahanbakht, “Fractaly terminated line-fed microstrip slot antenna”, *International Conference on Microwave and Millimeter Wave Technology,* vol. 4, pp. 1641-1643, Nanjing, China, April 2008

[163] D. D. Krishna, M. Gopikrishna, C. K. Aanandan, P. Mohanan, and K. Vasudevan, “Compact wideband Koch fractal printed slot antenna”, *IET Microwaves, Antennas and Propagation*, vol. 3, pp.782–789, August 2009

[164] R. Azadeganand K. Sarabandi, “Design of miniaturized slot antennas,” *IEEE International Symposium on Antennas and Propagation*, vol. 4, pp. 565–568, July 2001

[165] N. Behdad, and K. Sarabandi, “Bandwidth enhancement and further size reduction of a class of miniaturized slot antennas,” *IEEE Transactions on Antennas and Propagation*, vol. 52, pp. 1928–1935, Aug. 2004

[166] S. I. Latif, L. Shafai, and S. K. Sharma, “Bandwidth enhancement and size reduction of microstrip slot antennas,” *IEEE Transactions on Antennas and Propagation*, vol. 53, pp. 994-1003, March 2005

[167] M. Kahrizi, T. Sarkar, and Z. Maricevic, “Analysis of a wide radiating slot in the ground plane of a microstrip line,” *IEEE transactions on Microwave Theory and Techniques*, vol. 41, pp. 29-37, Jan. 1993

[168] N. Behdad, and K. Sarabandi, “A wide-band slot antenna design employing a fictitious short circuit concept,” *IEEE Transactions on Antennas and Propagation*, vol. 53, pp. 475-482, Jan. 2005

[169] C. R. Cockrell, “The input admittance of the rectangular cavity-backed slot antenna,” *IEEE Transactions on Antennas and Propagation*, vol. 24, pp. 288-294, May, 1976

[170] B. N. Das, and K. K. Hoshi, “Impedance of a radiating slot in the ground plane of a microstripline”, *IEEE Transactions on Antennas and Propagation*, vol. 30, pp. 922-926, Sep. 1982

[171] D. M. Pozar, “A reciprocity method of analysis for printed slot and slot-coupled microstrip antennas,” *IEEE Transactions on Antennas and Propagation*, vol. 34, pp. 1439-1446, Dec, 1986

[172] H. G. Akhavan, and D. Mirshekar-Syahkal, “Approximate model for microstrip fed slot antennas,” *IET Electronics Letters*, vol. 30, pp. 1902-1903, Nov. 1994

[173] B. Stockbroechx, I. Huynen, and A. V. Vorst, “Effect of surface wave diffraction on radiation pattern of slot antenna etched in finite ground plane,” *IET Electronics letters*, vol. 36, pp. 1444-1446, Aug., 2000

[174] R. G. Kouyoumjian, and P. H. Pathak, “A uniform geometrical theory of diffraction for an edge in a perfectly conducting surface,” *IEEE Proceedings*, vol. 62, pp. 1448-1461, Nov. 1974

[175] M. A. Forman, and Z. B. Popovic, “A tunable second-resonance cross-slot antenna,” *IEEE International Symposium on Antennas and Propagation*, Montreal, Canada, vol. 1, pp. 18-21, July, 1997

[176] B. K. Kormanyos, W. Harokopus, L. P. B. Katehi, and G. M. Reheiz, “CPW-fed active slot antennas,” *IEEE transactions on Microwave Theory and Techniques*, vol. 42, pp. 541-545, Apr. 1994

[177] http:www.agilent.com accessed Dec. 2009

[178] http://satimo.com accessed Dec. 2009

[179] J. X. Yun, and R. G. Vaughan, “Slot-wedge Multiple-Element Antennas,” *IEEE International Symposium on Antennas and Propagation*, Toronto, Canada, 2010

[180] J. X. Yun, and R. G. Vaughan, “Slot-wedge Antenna,” *IEEE International Symposium on Antennas and Propagation*, Toronto, Canada, 2010

[181] J. X. Yun, and R. G. Vaughan, “Open slot antenna in a small groundplane at the second resonance,” *IEEE International Symposium on Antennas and Propagation*, Toronto, Canada, 2010

[182] J. X. Yun, and R. G. Vaughan, “Impedance of Closely Spaced Orthogonal Slot Antennas,” *Canadian Conference on Electrical and Computer Engineering*, pp.1054-1057, 2007

[183] J. X. Yun, and R. G. Vaughan, “Multiport impedance testing of antennas for MIMO systems,” *IEEE International Symposium on Antennas and Propagation*, pp. 2965–2968, 2007

[184] J. X. Yun, and R. G. Vaughan, “Space efficiency of multiple element antennas,” *IEEE Transactions on Antennas and Propagation*, under review

[185] http://en.wikipedia.org/wiki/Polyhedron, accessed August, 2010

[186] http://en.wikipedia.org/wiki/Archimedean_solid, accessed August 2010